

THE MEASUREMENT OF FORCES IN CHIP REFINERS

By

SEYED MOHAMMAD ALI SIADAT

B.Eng. (Mechanical Engineering), McMaster University, 1997

A THESIS SUBMITTED IN PARTIAL FULFILLMENT OF THE
REQUIREMENTS FOR THE DEGREE OF
MASTER OF APPLIED SCIENCE

In

THE FACULTY OF GRADUATE STUDIES

Department of Mechanical Engineering

We accept this thesis as conforming to the required standard

THE UNIVERSITY OF BRITISH COLUMBIA

March 2001

© S. M. Ali Siadat, 2001

In presenting this thesis in partial fulfilment of the requirements for an advanced degree at the University of British Columbia, I agree that the Library shall make it freely available for reference and study. I further agree that permission for extensive copying of this thesis for scholarly purposes may be granted by the head of my department or by his or her representatives. It is understood that copying or publication of this thesis for financial gain shall not be allowed without my written permission.

Department of Mechanical Engineering
The University of British Columbia
Vancouver, Canada

Date 17th APRIL, 2001

ABSTRACT

The purpose of the chip refining process in the pulp and paper industry is to produce wood pulps and to enhance certain desirable properties of the fibres in the pulp suspension, by subjecting the wood material to cycles of shear and compressive stress. This process has commonly been quantified in terms of energy-based parameters such as specific energy and refining intensity, but such methods, although useful for establishing energy-pulp quality relationships, do not describe the underlying fundamental mechanisms of the process. It has been suggested that a knowledge of the stress-strain history of individual fibres can yield a deeper understanding of the process [Page, Fundamental Research Symposium (1989)].

With the long-term goal of such an understanding, the forces experienced by pulp in the refining zone are measured in a laboratory refiner operating at 700 rpm with softwood TMP at 16% consistency. This is done using a two-axis force sensor, originally designed by A. Bankes, P. Wild and D. Ouellet. The design, in its original form, did not perform well enough to provide a reliable force measurement under the high excitation frequency of passing refiner bars, as the sensor's resonant frequency was too low. A modified design with a much higher natural frequency is presented here, along with force measurements in the refining zone for various plate clearances, and varying dilution flow rate.

From these measurements, we see that both the normal and shear forces contain a component due to the ploughing action of the corner of the bar through the floc (termed

the corner force), a phenomenon previously only seen in the shear force [Batchelor et al. J. Pulp Pap. Sci. 23(1) (1997), Senger et al., Proceedings of the International Mechanical Pulping Conference, (2001)].

The peak normal force increased with decreasing plate clearance, while the peak shear force measured by the sensor did not exceed 11 N, corresponding to a maximum shear force per unit bar length of 2.2 kN/m. The equivalent tangential coefficient of friction decreased with decreasing plate clearance, and also decreased upon the addition of dilution water. The sensor design needs further refinement for testing at higher refiner rotational speeds, as signals acquired at high speeds are distorted by the sensor's resonant vibrations.

CONTENTS

ABSTRACT	ii
LIST OF TABLES	vii
LIST OF FIGURES	viii
ACKNOWLEDGEMENT	x
1. INTRODUCTION	1
2. REFINING THEORY	6
2.1 Energy-Based Refining Theories	6
2.1.1 Introduction To Energy-Based Refining Theories.....	6
2.1.2 Low Consistency Refining Theory	8
2.1.3 High Consistency Refining Theory	9
2.2 Force-Based Refining Theories	11
2.2.1 Forces In Low Consistency Refining.....	12
2.2.2 Forces In High Consistency Refining.....	15
2.3 Research Objectives	17
3. ORIGINAL SENSOR DESIGN	19
3.1 Design Details	19
3.2 Impact Tests & Calibration	22
3.3 Refiner Tests Using Original Sensor Design	28
3.4 Discussion Of Preliminary Test Results	33
3.4.1 Calibration.....	33
3.4.2 Dynamic Behaviour	34
3.4.3 Sensor Fabrication	35

4. MODIFIED SENSOR DESIGN.....	37
4.1 Design Modifications	37
4.1.1 Machining Of Housing Parts	37
4.1.2 Piezo Ceramic Elements	38
4.1.3 Insulating Material	38
4.1.4 Housing Support	39
4.1.5 Damping Mechanisms	41
4.1.6 Further Stiffening Of Sensor.....	41
4.2 Impact Tests & Calibration.....	43
4.2.1 Sensor Response To Combined Normal And Shear Loads	43
4.2.2 Effect Of Impact Position	48
5. REFINING TRIALS.....	50
5.1 Experimental Setup.....	50
5.2 Refining Force Profiles	51
5.2.1 Bar Passing Events.....	51
5.3 Data Rejection Criteria.....	55
5.3.1 Sensor Vibrations.....	56
5.3.2 Cyclic Fluctuations In Normal Force With Each Rotation.....	59
5.4 Analysis & Discussion	62
5.4.1 Impact Statistics.....	62
5.4.2 Variation Of Shear Force With Plate Clearance	63
5.4.3 Effect Of Injecting Dilution Water	65
5.4.4 Variation of $\mu_{t,eq}$ With Plate Clearance & Consistency	65

5.4.5 Ranges Of Measured $\mu_{t,eq}$ & Average Pressure	67
6. CONCLUSIONS	71
BIBLIOGRAPHY	73
NOMENCLATURE	76
APPENDIX A: Specifications Of D2B502 Refiner Plates	79
APPENDIX B: Properties Of Piezo Ceramic Elements	80
APPENDIX C: Calibration Procedure	81
APPENDIX D: Matlab Programs	96
APPENDIX E: Estimated Length Of Bars Crossing at Any Given Time100

LIST OF TABLES

1.1 Differences between chip refiners and pulp refiners	4
4.1 K-Values determined by impacting the sensor at different angles	45
4.2 Variation of sensitivity (K-values) of piezo elements 2 and 3 with varying impact position on the top face of the probe. All K-values are in V/N, and σ is the standard deviation.....	49
5.1 Summary of impact statistics for refining runs at 700 rpm (σ is the standard deviation)	63
5.2 Values of constants from different sources for use in Equation 2.8 (S1 and S2 refer to primary and secondary stage processes, respectively).....	68

LIST OF FIGURES

1.1 Schematic diagram of a chip refiner	2
3.1 Components of the preliminary sensor design.....	20
3.2 Sensor installed in refiner plate for measuring forces during refiner operation	21
3.3 Impact testing of sensor (mounted in jig) using force hammer. Impacts in the x-direction correspond to the direction of bar impacts at the leading edge during refiner operation	23
3.4 Force hammer impact in time and frequency domain	23
3.5 Response of sensor (from piezo elements 1 & 3) to a normal impact at the probe tip ...	24
3.6 Variation of peak signal voltage from piezos 1, 2 and 3 with impact force for normal impacts	25
3.7 Average transfer functions for piezo elements 1 and 3 in response to 20 vertical impacts	27
3.8 Signals from piezo elements during refiner operation. Bar passing events cannot be distinguished as vibrations dominate the signal.....	30
3.9 Refining forces derived from the above signals. The fine line corresponds to the forces calculated from piezo elements 1 and 3, while the bold line uses the combination of piezo elements 2 and 3.....	30
3.10 The variation of the refining forces over a period of 1 second, as derived from different piezo combinations. The periodic behaviour corresponds to the rotor plate rotation	32
3.11 Comparison of measured with calculated values of the normal force for impacts applied to the sensor when mounted in the plated	33
3.12 Exaggerated diagram showing how the piezo elements deform as the probe is displaced	35
4.1 Sensor housing design changes.....	38
4.2 Average transfer functions for piezo elements 1 and 3, with the new housing modifications and the 2 mm-wide piezo elements.....	40
4.3 Sensor used in conjunction with shims in order to inhibit deformation of housing	40

4.4 Effect of using latex pads in conjunction with layers of mica in the shims. The time domain signal of piezo element 3 is shown in response to an impact from the force hammer	42
4.5 Transfer functions for piezo elements 1 and 3, for revised sensor design with all new modifications.....	42
4.6 Impacts administered at different angles by using aluminum wedges	44
4.7 A comparison of the true normal component with values calculated from Equations 4.4a and 4.5a	47
4.8 A comparison of the true normal and shear components with those calculated from Equations 4.4b and 4.5b.....	47
4.9 The moving load during a bar passing event. As the rotor bar moves across the top of the probe, so does the centre of pressure	48
5.1 Refining normal force (bold line) and shear force (fine line) at 700 rpm as calculated using piezo combinations 2-3 and 2-4	52
5.2 One of the three segments of the D2B502 rotor plate (the stator plate segments are identical)	53
5.3 The normal (bold line) and shear forces (fine line) due to a typical bar impact.....	54
5.4 An illustration of problematic 30 kHz resonant vibrations of the sensor	56
5.5 Typical force profiles of bar impacts at 2560 rpm.....	57
5.6(a) Sensor vibrations at approximately 2 kHz	58
5.6(b) 2 kHz vibrations grow in amplitude for five successive bar impacts, until a sixth impact from a wider bar reduces their amplitude. This record shows several successive occurrences of this phenomenon.....	58
5.7 Cyclic fluctuations in normal force with each rotation at 2560 rpm	60
5.8 Variation of plate clearance and mean normal force through one full rotation of the rotor plate	61
5.9 Equivalent tangential coefficient of friction versus plate clearance	66
5.10 Plot of the equivalent tangential coefficient of friction against average mechanical pressure for different refiners.....	68

ACKNOWLEDGEMENT

The author wishes to thank the many people whose help eased the task of preparing this thesis. To Dr. D. Ouellet for the priceless guidance provided throughout my experience as a Masters' student. To J. Senger for the many helpful discussions and valuable feedback, and for generally being a pleasure to work with. To R. Nagy for the technical support to combat the seemingly endless computer problems. To Dr. P. Wild, A. Bankes, M. Olmstead and B. Shiari for much helpful input regarding the force sensor. To P. Taylor for the meticulous fabrication of sensor parts. To T. Paterson, K. Wong, L. Brandly, B. Dutka, J. Marsden, B. McMillan, R. Penko, J. Mackenzie, G. White, Dr. R. Thiruvengadaswamy, and Dr. G. Stewart for providing help in many areas during my time at the Pulp & Paper Centre. To the NCE Mechanical Wood Pulps Network for funding my project. And most of all, to my parents for ceaseless love and support throughout my time as a student (and as a human being, for that matter).

1. INTRODUCTION

Refiners are used in the pulp and paper industry to mechanically separate fibres from the wood matrix and to enhance certain pulp properties. The former of the two actions, commonly termed mechanical pulping, is carried out in chip refiners at high consistency. Here, wood chips are fed into the refiner and fibres are peeled away from the wood structure by repeated cycles of shear and compressive stresses. This mechanism affects the physical properties of the individual fibres, and of the paper ultimately made from these fibres.

The most common type of refiner is the disc refiner, illustrated schematically in Figure 1.1. Pulp is fed through the inlet, and moves between the two refiner plates, one stationary and the other rotating at high speed (commonly 1800 rpm in North America, and 1500 rpm in Europe). Both plates have a bar and groove pattern, and are separated by a small gap through which the pulp flows. As the rotor bars pass over the stator bars, agglomerates of pulp fibres are trapped repeatedly between the passing bars, and in this way receive the cyclic loading that constitutes the mechanical action of refining.

These loading events are the topic of study in this work, for they are the basic cause of the changes to the fibre structure. The nature of the changes in the refined pulp is strongly dependent on the absolute and relative magnitudes of these loads and the number of loading cycles received by each fibre. These factors are influenced by the plate

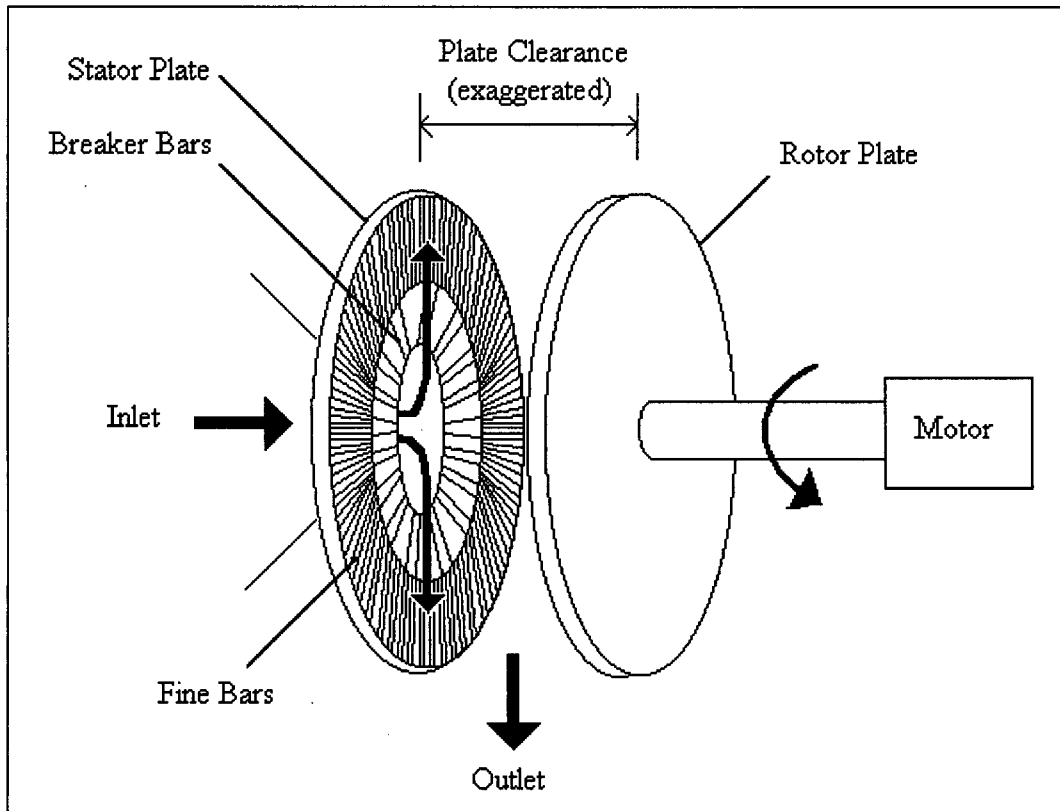


Figure 1.1 Schematic diagram of a chip refiner.

pattern, the refiner rotational speed, the pulp consistency, the plate clearance and the residence time of pulp in the refining zone. All these variables come under consideration depending on the desired result.

At this point, we must make a distinction between chip refining and pulp refining. Chip refining is the production of pulp from wood chips by refining at high consistency, whereas low consistency pulp refining is carried out to develop the properties of fibres that have already been separated by chemically dissolving the wood substances that bind them together.

In chip refiners, it is desired first to break down the wood chips and free the individual fibres, and then to enhance their flexibility. The chips are first impacted at the beginning of the refining zone with a coarse bar pattern that becomes progressively finer as we move radially outwards through the refining zone. The breaker bar section is tapered slightly to allow for a larger plate gap in this region, which narrows to a smaller gap at the intermediate bar section, and often continues to narrow all the way to the outer radius of the refining zone. Due to the high energy mechanical action in chip refiners, large amounts of steam are produced between the refiner plates, causing high temperatures and pressures that are not encountered in the lower consistency pulp refining process.

The purpose of pulp refining is to alter the properties of the fibres, which have already been separated from the wood matrix, to a state that best serves the final product. Therefore, the breaker bar section is not required in this application, and usually there is only one type of bar that spans the refining zone. As a result of the lower consistency, pulp refining is carried out at a much lower plate clearance than chip refining.

The key differences between pulp and chip refiners are summarized in Table 1.1. Due to these differences (most notably in the flow of pulp), the refining action in the two processes is characterized differently. On a very basic level, however, the action of the two types of refiners is similar, as in both cases the wood material is repeatedly beaten by passing refiner bars. Therefore, there are some similarities in the characterization of the different types of refiners.

	Chip Refiners	Pulp Refiners
Consistency	High (20-60%)	Low (3-5%)
Plate diameter	36 to 68 inches (0.91 to 1.73 m)	32 to 48 inches (0.81 to 1.22 m)
Speed	1500 rpm in Europe 1200 or 1800 rpm in North America (although some 1st stage refiners run at up to 2300 rpm)	600 to 900 rpm
Plate Clearance	0.5 to 3 mm	0.06 to 0.2 mm
Specific Energy	1.5 to 3.5 MWh/t	80 to 250 kWh/t
Pulp Flow	Pulp is propelled by forces inside refiner	Pulp suspension is pumped through refiner

Table 1.1 Differences between chip refiners and pulp refiners.

In order to predict the extent of the refining treatment received by the fibres, a number of theories have been put forward. For the most part, these have been based on the net mechanical energy transferred to a unit mass of pulp, and the “intensity” at which this energy is applied. This approach has proven useful in developing relationships between key operating variables and the quality of the resulting pulp suspensions, and the simplicity of some of these energy methods has facilitated their widespread use. However, when it comes to understanding the fundamental mechanisms of refining, such energy-based theories offer limited insight, because they make no attempt to describe the mechanisms by which the energy was transferred to the fibres.

Refined fibres undergo a variety of structural changes due to the different modes of loading they experience. Passing bars cut and bend fibres, and subject them to cyclically varying normal and shear stresses. Furthermore, the effects also depend on the combinations of the modes of loading and the relative magnitudes of these loads.

A general objective of the work presented here is to develop a better understanding of high consistency refining based on the forces encountered in the process. This work will

focus on measuring the forces that are experienced between refiner bars and examining how they are affected by operating conditions. The basis of our approach was to develop a two-axis force sensor capable of withstanding the harsh conditions present inside an operating refiner, and to use this sensor to measure forces at various plate clearances, consistencies and rotational speeds.

The refiner used in this study is a 12-inch Sprout Waldron laboratory refiner. The force sensor used was originally designed by Alan Bankes [1], and was modified in order to improve its behaviour. The modified design is useful for tests on the laboratory refiner, operating at speeds up to 700 rpm, above which meaningful force measurements are not possible as sensor vibrations dominate the signal.

This thesis begins with a review of refining theories and previous investigations regarding the refining forces. The focus then shifts to the development, testing and use of the refiner force sensor. This is followed by an analysis of force measurements made during refiner operation.

2. REFINING THEORY

Characterization of the action of refining has evolved over the years to enable producers of pulp to predict the effects of different operating conditions. This chapter will review the key theories put forward to characterize the action of both high consistency and low consistency refining. The review will focus first on energy-based theories for the two types of processes, and then on research into forces experienced by pulp flocs in refiners. This will set the stage for a summary of the objectives of the work presented in this thesis.

2.1 ENERGY-BASED REFINING THEORIES

2.1.1 INTRODUCTION TO ENERGY-BASED REFINING THEORIES

The most widely used parameter for characterization of the degree of refining at both high and low consistency is the specific energy, which is defined as the energy transferred per unit mass of pulp. It is calculated from:

$$E = \frac{P}{\dot{m}_f} \quad (2.1)$$

where P is the net power transferred to the pulp and \dot{m}_f is the oven-dry fibre mass flow rate through the refiner.

On its own, the specific energy is not enough to fully characterize the refining action, because of differences in types and sizes of refiner, plate designs and operating conditions. Therefore, two trials with pulp refined to the same specific energy can

exhibit very different results, as the different effects of refining on the fibres (internal and external fibrillation, fibre cutting, etc.) can occur to different extents. This is true for both high consistency [2] and low consistency processes [3].

It was therefore necessary to develop a second parameter which, when used in conjunction with the specific energy, would allow us to predict the effects of refining by accounting for other important refining conditions. This additional parameter generally attempts to quantify the severity or intensity of the refining treatment by estimating the amount of energy transferred to pulp with every refiner bar impact.

The number of impacts received by each fibre is directly dependent on the time it spends in the refining zone (the residence time). In low consistency refiners, pulp is pumped through by an external pumping system, and the liquid nature of the suspension allows a simple calculation of the residence time based on geometric considerations and the flow rate of the pulp suspension. In high consistency chip refiners, the pulp suspension behaves more like a wet solid than a liquid, and no pump is used. Therefore, the velocity of the pulp through the refiner is determined by considering the forces acting on it, such as the centrifugal force, contact forces with the refiner plates, and drag forces from the large amounts of steam produced during the process.

Because of these key differences in the way pulp flows through low and high consistency refiners, the measures of refining intensity differ in these two cases. They will therefore be reviewed separately in the next two sections.

2.1.2 LOW CONSISTENCY REFINING THEORY

There have been many suggestions for the form of the refining intensity parameter at low consistency. As the name suggests, this parameter, in all its forms, describes the severity with which the energy treatment is imparted to the pulp.

The definitions of the measures of intensity discussed here are all in the form:

$$I = \frac{P}{\text{constant}} \quad (2.2)$$

where I is the intensity and P is the net power. The form of the constant in the denominator distinguishes the different ways of measuring the intensity.

In low consistency processes, the most commonly used intensity measure is the specific edge load (SEL), defined as [4]:

$$SEL = \frac{P}{CEL} = \frac{P}{\sum_i n_{ri} n_{si} L_i \omega} \quad (2.3)$$

The denominator here is known as the cutting edge length (CEL). It is the total length of bar crossings per second in the refining zone. The values n_{ri} and n_{si} are the number of bars on the rotor and stator, respectively, in a radial increment i , L_i is the length of the refiner bar within the radial increment, and ω is the rotational speed of the refiner (revolutions per second). The SEL is therefore a measure of the energy transferred per unit length of bar, measured in J/m.

This intensity measure is based on the design of the plates in use, but neglects many parameters that are known to have an effect on the mechanical treatment. A major criticism of the *SEL* theory is that it ignores parameters such as groove depth, bar and groove widths, and bar angle, although it has been suggested that some of these parameters are indirectly accounted for [5]. In response to these criticisms, extensions to the *SEL* theory were devised that included some of these other plate parameters. Among these were the Modified Edge Load (*MEL*) [6] and Specific Surface Load (*SSL*) [7] theories.

Other theories were not limited to plate design parameters, as factors such as pulp consistency, unrefined fibre properties and plate clearance had yet to be addressed. Possibly the most comprehensive of all intensity measures to date, in terms of accounting for all the relevant factors in the refining process, comes from Kerekes' C-factor theory [3]. This theory accounts for plate parameters, pulp properties and operating variables, and also allows for an estimation of the number of impacts received by each fibre, as well as the average energy associated with each impact. However, due to its more complex nature than the *SEL*-type theories, the C-factor theory is not as widely used in industry.

2.1.3 HIGH CONSISTENCY REFINING THEORY

One of the greatest influences in the understanding of high consistency refining came when Miles and May published their highly successful model of the flow of pulp in chip refiners [8] in 1990. They followed it up a year later with extensions on the theory and experimental results to support the work [9]. Their approach consists of considering the

forces acting on an element of pulp in the refining zone to predict its radial velocity, which is then used to estimate the residence time.

The model predicts that this element of pulp is acted on by centrifugal and frictional forces, along with the drag forces exerted by the copious amounts of steam generated in the refiner. The equation derived for the radial velocity of the pulp, v , as it relates to the radial position in the refining zone, r , is:

$$\frac{dv}{dr} = \frac{r\omega^2}{v} - a \frac{\mu_r}{\mu_t} \frac{Ec(r)}{\omega(r_2^2 - r_1^2)} + S \quad (2.4)$$

where ω is the refiner's rotational speed, c is the pulp consistency (fraction), μ_r and μ_t are the coefficients of friction in the radial and tangential directions respectively, r_1 and r_2 are the inner and outer radii of the refining zone, a is a constant that equals 4 for a single-disc refiner and 2 for a double-disc refiner, and S is a term related to the steam flow. The steam flows backward (i.e. counter to the flow of pulp) near the inlet of the refining zone, and forward near the outlet, exerting no force on the pulp at the stagnation point in between. Therefore, by assuming that the effects of the backward and forward flowing steam cancel each other out, the equation is simplified by removing the steam flow term [10]. A further simplification can be made by assuming that the pulp velocity gradient is small relative to other terms in Equation 2.4, and the differential equation is then reduced to a simple algebraic equation.

The residence time, τ , can then be determined using:

$$\tau = \int_{r_1}^{r_2} \frac{dr}{v} \quad (2.5)$$

and the number of impacts experienced by each unit of pulp, n_{imp} , is:

$$n_{imp} = \frac{2N_{av}\omega(r_1 + r_2)\tau}{a} \quad (2.6)$$

where N_{av} is the average number of bars per unit length of arc. Using this, Miles and May then coined an intensity measure for the chip refining process. This is the specific energy per impact, e :

$$e = \frac{E}{N_{av}} \quad (2.7)$$

Thus, as Miles, May and associates have shown [8-11], a two-parameter energy-based characterization can be used to predict certain pulp property changes associated with changes in refining conditions.

2.2 FORCE-BASED REFINING THEORIES

To their credit, researchers have come a long way in predicting the response of pulp to refining by quantifying the process in terms of energy-based parameters. However, all of these characterizations possess the common shortcoming that none can describe the exact mechanisms of the energy transfer. A variety of structural changes are experienced by the fibres in the process, among which internal fibrillation, external fibrillation, fibre shortening and the creation of fines are the main ones. The type of loading seen by the fibres is the direct influence for these changes, but none of the energy based characterizations yield an understanding of these effects. The following sections are dedicated to the research that has focused on the refining forces in order to gain a

complete, detailed picture of the mechanical phenomena occurring inside a refiner. The cases of high and low consistency are again taken up separately.

2.2.1 FORCES IN LOW CONSISTENCY REFINING

In 1989, Page described his vision of the forces acting on an agglomerate of pulp fibres (a floc) as it is trapped between passing bars in the refining zone [12]. He envisioned three main forces in refining: a normal component (perpendicular to the faces of the bars) due to the compression of the floc, a shearing component (in the direction tangential to the relative motion of the bars) due to friction between the pulp and the bars, and a “ploughing” force (also known as the ‘corner force’) required for the bar corners to plough through the floc. Page himself did no work to measure these forces.

One of the first attempts to quantify the refining forces was described by Khlebnikov et al. at the Leningrad Institute for the Pulp and Paper Industry. They used sensors to determine the forces in a conical refiner operating at 2-3 % consistency [13]. They measured forces in two perpendicular directions on the face of a refiner bar, those directions being normal to the face of the bar (the normal force) and tangential to the motion of the bar (the tangential force, or shear force). They plotted the shear force profile that they measured due to individual bar passing events where flocs were trapped between opposing refiner bars. The shear force was seen to rise sharply at the start of the event, then fall sharply to a much lower level where it remained essentially constant until the trailing edges of the bars in question parted ways.

The sensor designs they used were based on strain gauges, and these designs were revised the following year [14] before being used by Goncharov, who then implemented their use in a disc refiner [15]. He reported similar force profiles to those of Khlebnikov et al.

In retrospect, it seems likely that the initial peak in the shear force was due to the corner force described by Page twenty years later, and the lower, constant force regime that followed it was the friction force between the pulp and the metal faces of the refiner bars.

The initial high force regime was seen to act for a greater portion of the bar passing event when the plate clearance was decreased. The overall magnitudes of the forces measured were seen to rise with increasing consistency, increasing operating speed, and decreasing plate gap. Khlebnikov et al. defined the ratio of the tangential force to the normal force as the coefficient of refining, and saw that it increased for decreasing plate clearance and for increasing speed. Goncharov reported a coefficient of refining of approximately 0.11 for unbleached sulphite pulp at 2.5-3 % consistency refined at 720 rpm. He also quoted peak pressures at the bar surface of around 3.4 MPa for the initial high force regime.

In 1981, Nordman et al. measured pressures in grooves and on bar surfaces in a disc refiner at low consistency, running at 1200 rpm [16]. They registered pressure peaks on the bar surfaces that corresponded to bar passing events, although these were somewhat more erratic in nature than those depicted by Khlebnikov et al. Nordman et al. reported peak to peak pressures of 0.08-0.12 MPa due to bar passing events – more than 20 times lower than those reported by Goncharov.

In 1997, Martinez, Batchelor, Kerekes and Ouellet published work done to characterize and model the forces on pulp flocs when trapped between opposing refiner bars at low speed (corresponding to approximately 1 rpm) [17,18]. Their tests were performed on a specially designed machine, called the single-bar refiner. This could compress and shear one floc of pulp at a time in the same way as would occur between opposing refiner bars, while measuring forces in the normal and tangential directions. In this way, they could examine the effect of single bar passing events on individual flocs.

They used spherical nylon flocs at a consistency of 9.5% and assumed linear elastic behaviour to develop and test a force model. These tests showed evidence of a corner force component in the shear force. After this initial peak, the shear force dropped to a lower constant value. The normal force profile rose to a peak at the beginning of the bar passing event, and remained essentially constant until the trailing edges of the passing bars parted ways.

The model was later modified by Batchelor and Ouellet to consider previously dried kraft pulp fibres with collapsed lumens. It was also extended to predict the tensile forces experienced by individual fibres. According to the model, the tensile force to which a fibre is subjected depends on the location and orientation of the fibre within the floc, as well as the size of the trapped portion of the floc [19].

2.2.2 FORCES IN HIGH CONSISTENCY REFINING

In 1975, Atack et al. measured the temperature and pressure at different locations in the refining zone in a single-disc, open-discharge refiner operating at 1800 rpm and discharge consistencies of 20-50% [20]. Although they could not see the details of bar passing events, they did see pressure “spikes” at the frequency at which bars passed over the pressure sensor. These spikes were seen to be as high as 620 kPa at times. Atack later suggested that the magnitude of these spikes would be influenced by the size of flocs [21].

In their pressure measurements, Atack et al. also observed cyclic pressure fluctuations (approximately 28 kPa in magnitude) with each rotation of the rotor plate, upon which the spikes were superimposed. Having correlated this cyclic variation with variations in the plate separation due to run-out in the rotor plate, they concluded that this periodic fluctuation was due to the saturated steam pressure in the refining zone. In later work, Atack et al. used high-speed photography to show that periodic variations in the amount of pulp present at any given area of the refining zone occur due to that same rotor run-out phenomenon [22].

In 1982, Franzen and Sweitzer studied the variation of the total axial thrust with varying motor load, specific energy and consistency [23]. They quantified the refining forces in terms of the total axial thrust and a tangential friction force (which draws the torque from the motor) between the plates. The latter was defined as proportional to the axial thrust,

the constant of proportionality being a coefficient of friction. They proceeded to claim (referring to extensive unpublished work by Fisher) that this coefficient of friction increased with increasing consistency. The resultant tangential friction force was envisioned to act at a certain radial distance from the centre of the plates, and this distance was shown to vary depending on the operating conditions.

Miles and May derived the following simple equation for this coefficient of friction for a non-pressurized refiner [8]:

$$\mu_t = \frac{2P}{h\omega F_m(r_1 + r_2)} \quad (2.8)$$

where μ_t is the tangential coefficient of friction, P is the motor load, F_m is the total axial thrust, r_1 and r_2 are the inner and outer radii of the refining zone, respectively, ω is the rotational speed of the refiner (rad/s) and h is the number of rotating discs (1 or 2).

Using data from a Bauer 914 mm atmospheric double-disc refiner operating at 1200 rpm, they plotted the motor load against the axial thrust for different pulp consistencies (15, 20 and 30%) and found all points to fall on the same straight line, indicating that the coefficient of friction was independent of consistency. From the slope of the line, they calculated a value of 0.75 for μ_t . Furthermore, they suggested that μ_t was independent of the radial position in the refining zone. As the tangential speed of a refiner bar is proportional to the radial position at which the speed is measured, this implies that μ_t would also be independent of refiner speed.

Most recently, Senger and Ouellet used the single bar refiner apparatus of the work of Martinez et al. and Batchelor et al. to examine the forces on TMP flocs at high consistency and low speed [24]. They showed nonlinear elastic behaviour at high consistency, and presented clear evidence of the corner force component in the shear force. As the corner force was seen to represent a large part of the shear force, the ratio of the shear to the normal force could no longer be considered a true coefficient of friction, and they coined a new variable, the equivalent tangential coefficient of friction $\mu_{t,eq}$, as this ratio. $\mu_{t,eq}$ was shown to increase with increasing consistency and with increasing floc grammage, and it was seen to decrease with an increasing extent of bar wear.

2.3 RESEARCH OBJECTIVES

The fact that energy-based characterizations do not refer directly to the mechanisms by which refining causes structural changes in the fibres leaves us in search of a force-based theory by which we can completely quantify and predict the effects of refining. Such a theory has yet to be developed, and before this can happen much work needs to be done in understanding the refining forces themselves.

This is not the only reason to study the refining forces. Given that the refining process is energy intensive, it becomes even more desirable to understand its underlying mechanisms, as it could help to reduce energy costs in the long run.

The objectives of the work presented here can be summarized as follows:

- To design and implement the use of a two-axis force sensor for a refiner operating at high consistency
- To measure the normal and shear forces experienced by pulp flocs during bar passing events
- To investigate how these forces are influenced by operating conditions.

Work was begun on the first of these three objectives by A. Bankes, P. Wild, and D. Ouellet prior to the start of the work presented as part of this Master's thesis. The original design and preliminary testing of the force sensor comprised the work done as part of the Master's degree of A. Bankes. This work is described in detail in his Master's thesis [1], and summarized in the next chapter.

3. ORIGINAL SENSOR DESIGN

The work of Bankes included the original design of the sensor, the building and testing of a large-scale prototype, and the construction and testing of a preliminary version of the force sensor for use inside the laboratory refiner at the UBC Pulp and Paper Centre. The reader is referred to Bankes' Master's thesis for details on the design concept and the large-scale prototype [1]. The testing of the original design was performed at UBC, and marked the beginning of the work done as part of this thesis.

The objectives for the tests described in this chapter were:

- to develop and implement a calibration procedure,
- to examine the sensor's dynamic behaviour,
- to examine force traces from the refiner and identify bar passing events,
- to bring to light any other issues involved in the design, fabrication, assembly and use of the sensor.

3.1 DESIGN DETAILS

The original design of the sensor is depicted schematically in Figure 3.1 in terms of its separate components, and the assembled item is shown in Figure 3.2. This design was devised by A. Bankes in collaboration with P. Wild and D. Ouellet [1].

The workings of the force sensor can be summarized as follows: The sensor's T-shaped probe is held inside the housing, completely supported by the four piezo ceramic

elements under preload, such that any displacement of the probe relative to the sensor housing will deform the piezo elements.

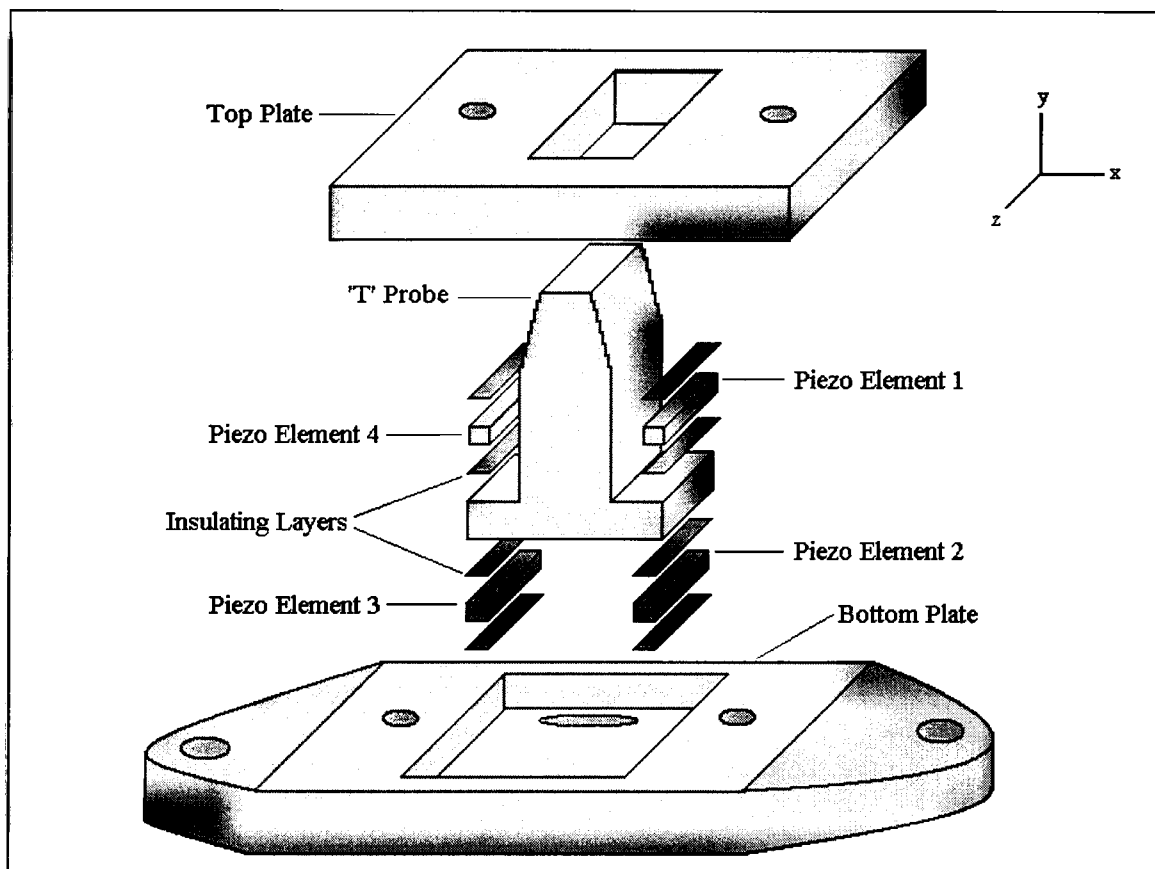


Figure 3.1 Components of the preliminary sensor design.

According to [1], signals from two piezo elements from opposite sides of the sensor probe tip (one from the left and one from the right, as pictured in Figure 3.1) can be used to uniquely determine the magnitude and direction of the force acting on the probe tip. The calculation of these forces is described in Section 3.2.

The sensor probe tip has the same shape as a refiner bar, and was designed as such to replace a 5 mm-long section of a bar. A hole was machined in the back of a D2B502 refiner plate (see Appendix A for specifications) in which the sensor fits snugly, with the probe tip replacing the removed bar section.

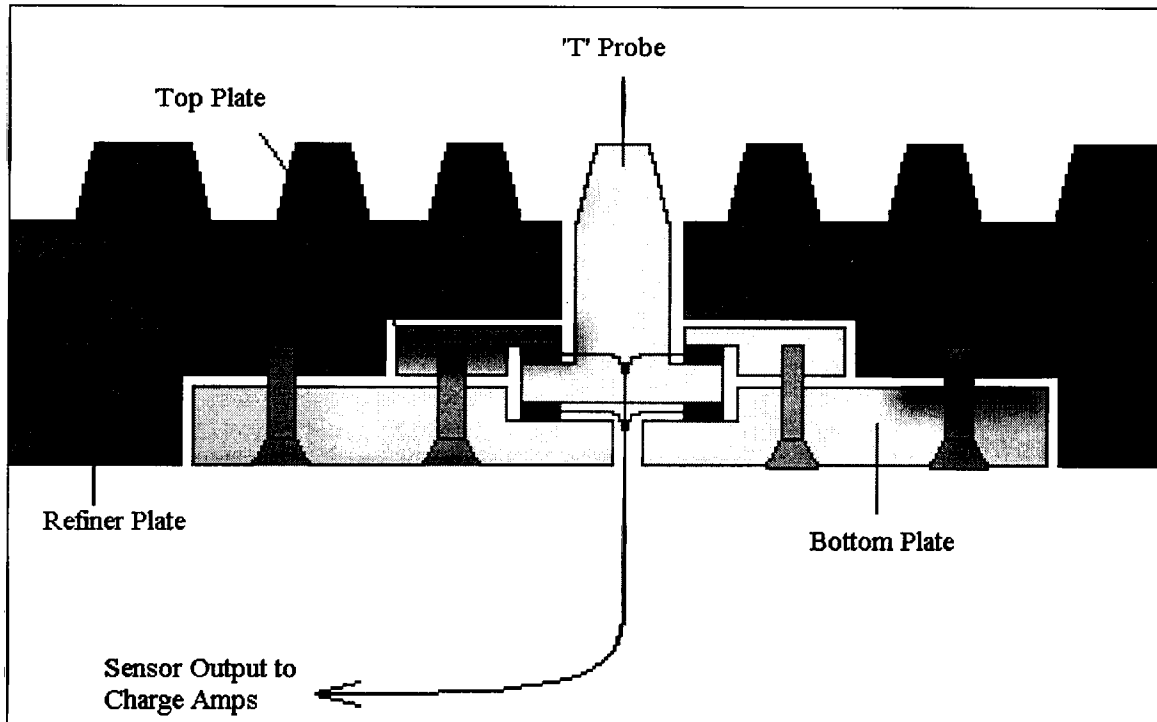


Figure 3.2 Sensor installed in refiner plate for measuring forces during refiner operation.

The piezo ceramic material used for the elements was lead zirconate titanate (PZT), whose ferro-electric behaviour is specified in Appendix B. The piezo elements in the original design were 1 mm x 1 mm x 7 mm in size, and were clamped under preload along the 5 mm length that was in contact with the probe. An insulating layer was required to prevent conduction between the electrodes of the piezo elements and the sensor's metal parts. In the preliminary design, small sheets of paper were glued to the appropriate locations on the sensor probe and housing for this purpose. The adhesive used was a Loctite™ cyano-acrylate product.

To prevent water from entering the sensor housing, it was sealed around the edges at the last step of the assembly using a silicone sealant.

3.2 IMPACT TESTS & CALIBRATION

The response of the refiner force sensor was characterized using a PCB 086D80 piezoelectric impact hammer. This device, used in conjunction with an appropriate signal conditioner, gives an output signal whose voltage is proportional to the magnitude of the force experienced at the tip of the hammer head. The impact testing setup is illustrated schematically in Figure 3.3.

The force hammer reliably measures forces up to 60 N, and the impacts provide excitation up to very high frequencies (see Figure 3.4). As a result, it is ideal for testing the sensor's response in both the time domain and the frequency domain.

The original calibration method consisted of impacting the sensor in two perpendicular directions, which corresponded to the directions of the normal (y-direction) and shear (x-direction) refining forces. However, this method cannot be used when the sensor is mounted in the refiner plate, because the neighbouring bars obstruct the hammer's path when trying to apply horizontal impacts. Therefore, the sensor was held in a vice for the calibration presented in [1], where it could easily be impacted in the two directions. It was later noted by the author of this work that the vice did not adequately replicate the sensor's mounting conditions in the refiner plate, and so a specially designed jig (depicted in Figure 3.3) was constructed to hold the sensor for the impact testing. The geometry of the jig's contacting surface with the sensor is identical to that of the refiner plate.

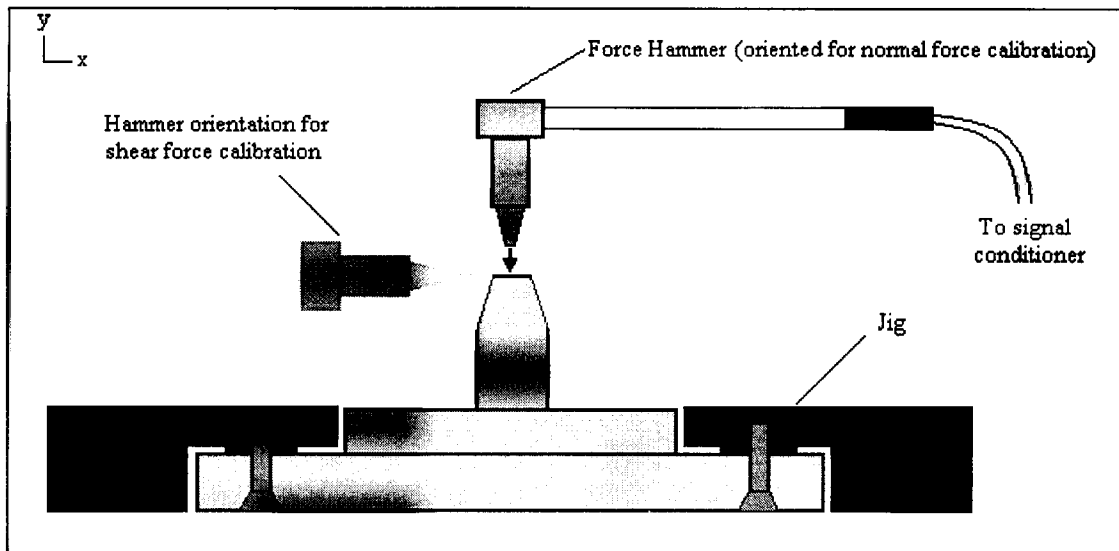


Figure 3.3 Impact testing of sensor (mounted in jig) using force hammer. Impacts in the x-direction correspond to the direction of bar impacts at the leading edge during refiner operation.

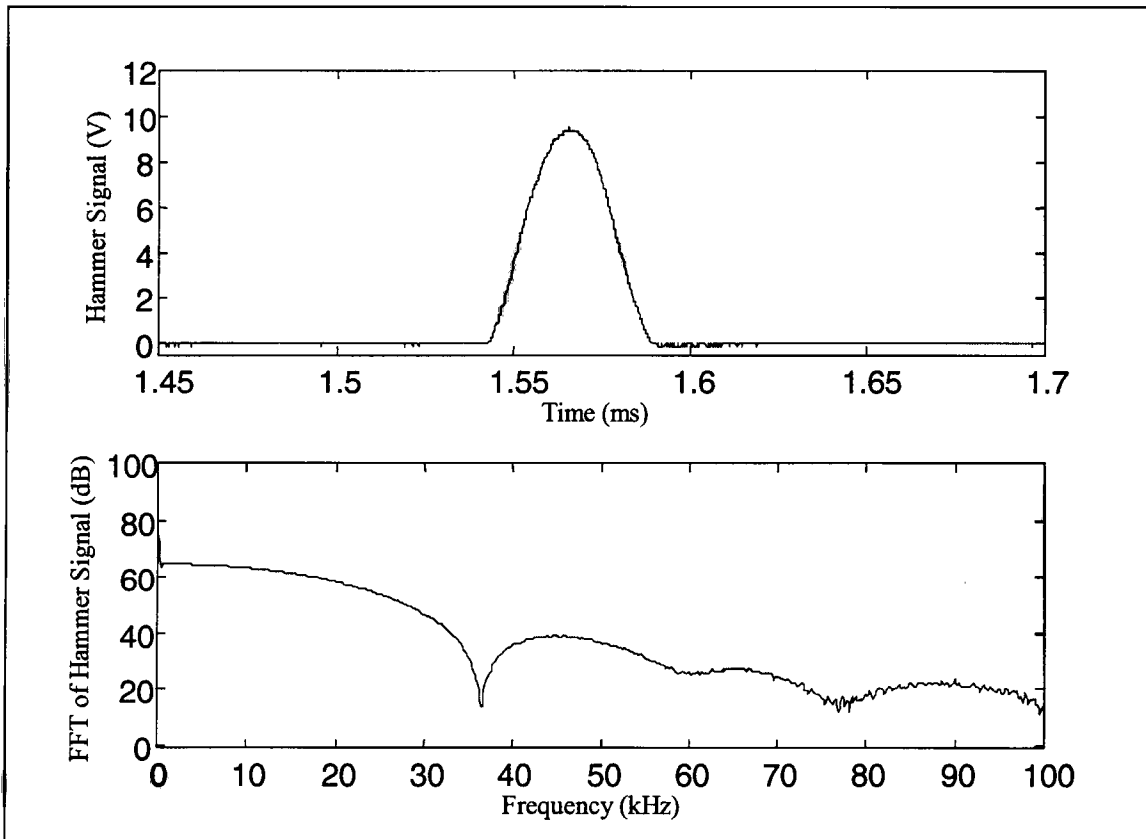


Figure 3.4 Force hammer impact in time and frequency domain.

The sensor was struck with the hammer and the resulting piezo signals were analysed. Piezo elements emit negative signals when compressed, and positive signals when extended¹. A sample impact with the corresponding sensor output signals is shown in Figure 3.5.

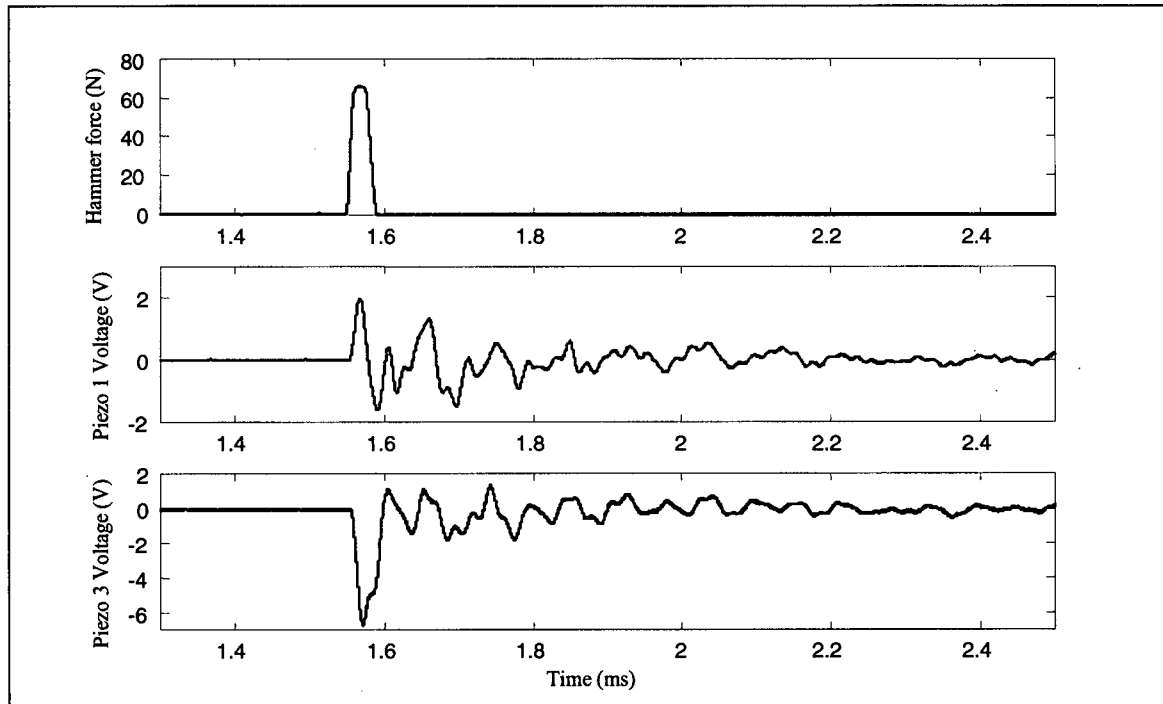


Figure 3.5 Response of sensor (from piezo elements 1 & 3) to a normal impact at the probe tip.

The magnitude of the first peak of each piezo element signal was seen to be directly proportional to the peak amplitude of the force hammer signal, for impacts in both the normal and shear directions. This is expressed mathematically as:

¹ The terms compression and extension, as used here, should be understood as being *relative to the preloaded state*. As the piezo elements are under preload, they are always under compressive stress. When the preload is applied, the piezo elements emit a signal for a brief period of time and then this signal fades to zero. Subsequently, the piezo elements emit no charge unless further relative deformation takes place. If the elements are then extended *relative to the preloaded state*, even though they are not experiencing a positive tensile stress, they will emit a positive signal.

$$V_i = K_{iN} F_N \quad (3.1a)$$

$$V_i = K_{iS} F_S \quad (3.1b)$$

where the subscript i denotes the piezo element number, V_i is the voltage from piezo element i , F_N and F_S are the normal and shear force magnitudes, respectively, and K_{iN} and K_{iS} are the normal and shear calibration coefficients (in V/N). The former relation, as an example is illustrated graphically in Figure 3.6.

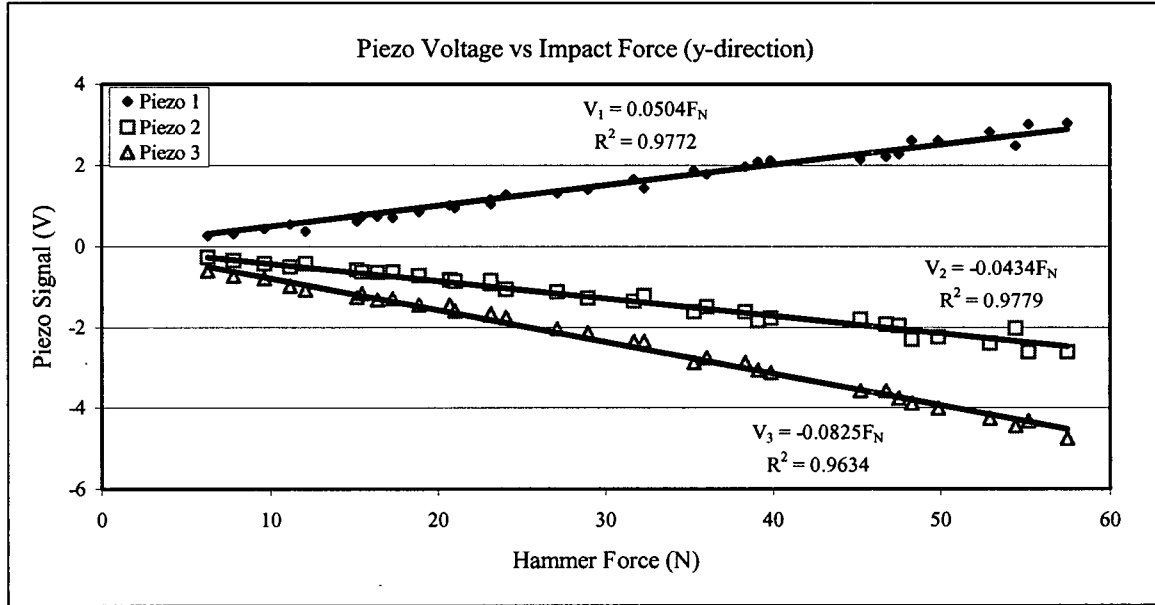


Figure 3.6 Variation of peak signal voltage from piezos 1, 2 and 3 with impact force for normal impacts.

At this point, it was assumed that the response from each piezo element to an impact at an arbitrary angle θ to the y-direction (a combined normal and shear load) was equal to the sum of the responses to the normal component $F \cos\theta$ and the shear component $F \sin\theta$. This assumption of the validity of linear superposition is tested in Section 4.2. For now, the following relations are assumed to hold:

$$F_N = F \cos\theta \quad (3.2a)$$

$$F_S = F \sin\theta \quad (3.2b)$$

$$V_i = K_{iN} F_N + K_{iS} F_S = F(K_{iN} \cos\theta + K_{iS} \sin\theta) \quad (3.3)$$

where F is the magnitude of the resultant force.

It should be noted here that these calibration coefficients K_{iS} and K_{iN} were determined by impacting the sensor in the aforementioned jig, after which the sensor was transferred to the refiner plate and again impacted in the normal direction to see how the response compared to that in the jig. Invariably, the values of K_{iN} determined from the plate and the jig differed, sometimes by up to 20%. Due to this discrepancy, the K-values subsequently used for force calculations were not those determined directly from the jig configuration. Instead, the value of K_{iN} from the plate was used, and K_{iS} was calculated using the following equation:

$$K_{iS} = \frac{K_{iN}(plate)}{K_{iN}(jig)} \cdot K_{iS}(jig) \quad (3.4)$$

This assumes that the normal and shear calibration coefficients change proportionately when the sensor's mounting conditions change. The validity of this assumption was difficult to verify in practice, and this represents a serious limitation of this calibration method. A more reliable method of determining the value of K_{iS} was therefore developed and will be presented in Section 4.2.

Using Equation 3.3, one can derive equations for the forces F_N and F_S given the voltage from any two piezo elements on opposite sides of the probe tip. These will be in the form:

$$F_N = C_i V_i + C_j V_j \quad (3.5a)$$

$$F_S = D_i V_i + D_j V_j \quad (3.5b)$$

where i and j are the numerical designations of the piezo elements on either side of the probe, and the values of C and D for these piezo elements can be determined using the K -values above. A detailed description of this calibration procedure, including the determination of all relevant constants, is given in Appendix C.

The average transfer functions of piezo elements 1 and 3 are depicted in Figure 3.7 for frequencies up to 15 kHz. Transfer functions were calculated for several impacts and averaged over the range of frequencies according to:

$$\overline{H}_i(f) = 20 \log \left(\frac{\sum_{j=1}^n (|V_i(f)/V_h(f)|_j)}{n} \right) \quad (3.6)$$

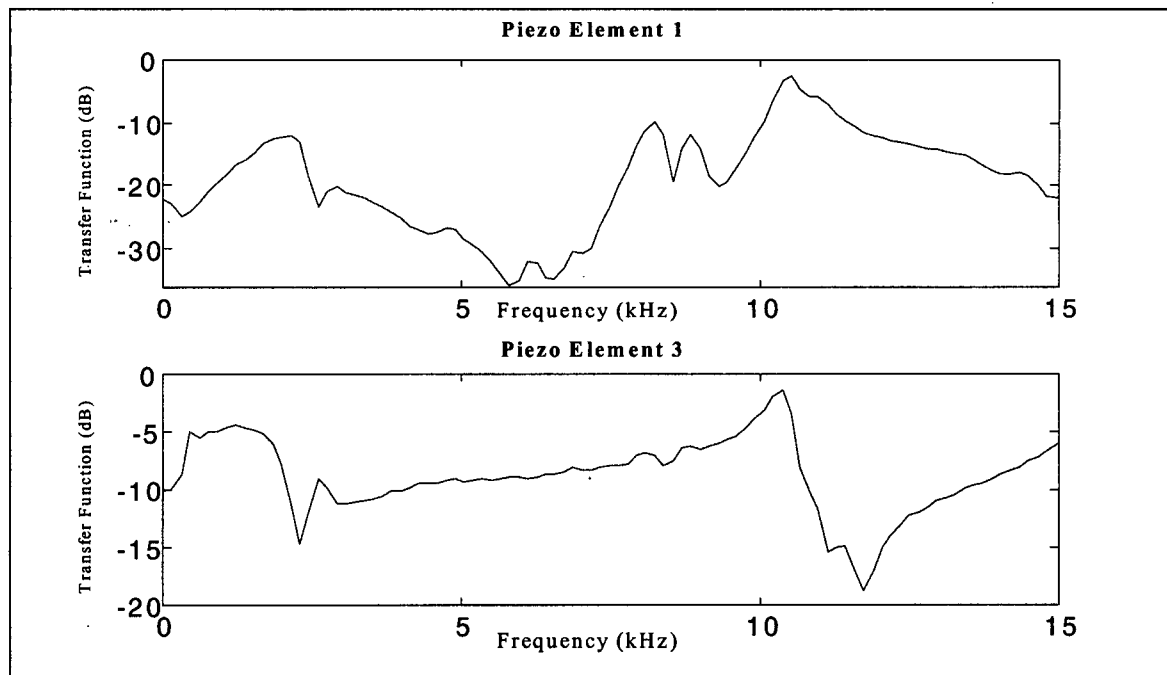


Figure 3.7 Average transfer functions for piezo elements 1 and 3 in response to 20 vertical impacts.

where $\overline{H}_i(f)$ is the magnitude (in dB) of the average transfer function at frequency f and $V_i(f)$ and $V_h(f)$ are the magnitudes of the signals from piezo i and the hammer, respectively, at said frequency.

We can see that the transfer function is markedly different between piezo elements 1 and 3. In both cases, the transfer function exhibits several peaks, first in the region between 1 and 3 kHz, and then above 8 kHz or so. This behaviour was unexpected, since a finite element analysis of the system, carried out by Bankes, indicated that the lowest natural frequency should be about 25 kHz. The cause of this discrepancy was not immediately apparent, but will be examined later in this chapter.

3.3 REFINER TESTS USING ORIGINAL SENSOR DESIGN

The force sensor was used to measure forces in the UBC Pulp and Paper Centre's Sprout-Waldron 12-inch laboratory refiner. This refiner is non-pressurized, and is run using a 50 horsepower (35 kW) motor. The motor load is controlled by manually varying the plate clearance.

The low natural frequency quoted above for the force sensor must be compared with the frequency at which bars on the refiner's rotor plate pass over the sensor probe during refiner operation, as this is the major frequency component of the excitation force. We calculate the bar passing frequency using the following equation:

$$f_{bp} = \frac{2\pi \cdot \Omega r_s}{60(B + G)} \quad (3.7)$$

where Ω is the refiner speed (rpm), r_s is the radial position (m) of the sensor on the refiner plate, and B and G are the bar and groove widths (m), respectively, on the rotor plate.

On the D2B502 plates used here, the sum $B + G$ is 5.4 mm, and the sensor was at a radial distance of 14.6 cm from the axis of rotation of the rotor plate. Thus, for a speed of 2560 rpm (full speed), f_{bp} is 7.2 kHz, and for 1260 rpm, f_{bp} is 3.6 kHz. Under normal circumstances, the refiner can be run at any desired speed up to 2560 rpm using a variable frequency drive. However, the drive emits large quantities of electrical noise which interfere with the data acquisition. This drive had to be bypassed as a result, and the refiner speed could only be varied by changing the configuration of the pulleys over which the drive belts ran. This allowed us to run the refiner at only two speeds: 1260 rpm and 2560 rpm.

Ideally the sensor should be an overdamped system with a natural frequency much higher than the frequency of excitation, so that the sensor's natural vibration does not affect its ability to measure the refining forces. However, from the data presented in Figures 3.5 and 3.7, we can see that this sensor has a low natural frequency and is underdamped. We could therefore expect that the sensor's vibration behaviour would dominate the signal, and prevent accurate force measurement. Indeed, this is exactly what was observed.

Figure 3.8 shows a 10 ms time trace of the individual piezo signals during refiner operation, and Figure 3.9 shows the force traces derived from those piezo signals. The signals are clearly dominated by the sensor's vibration, as can be seen in their sinusoidal

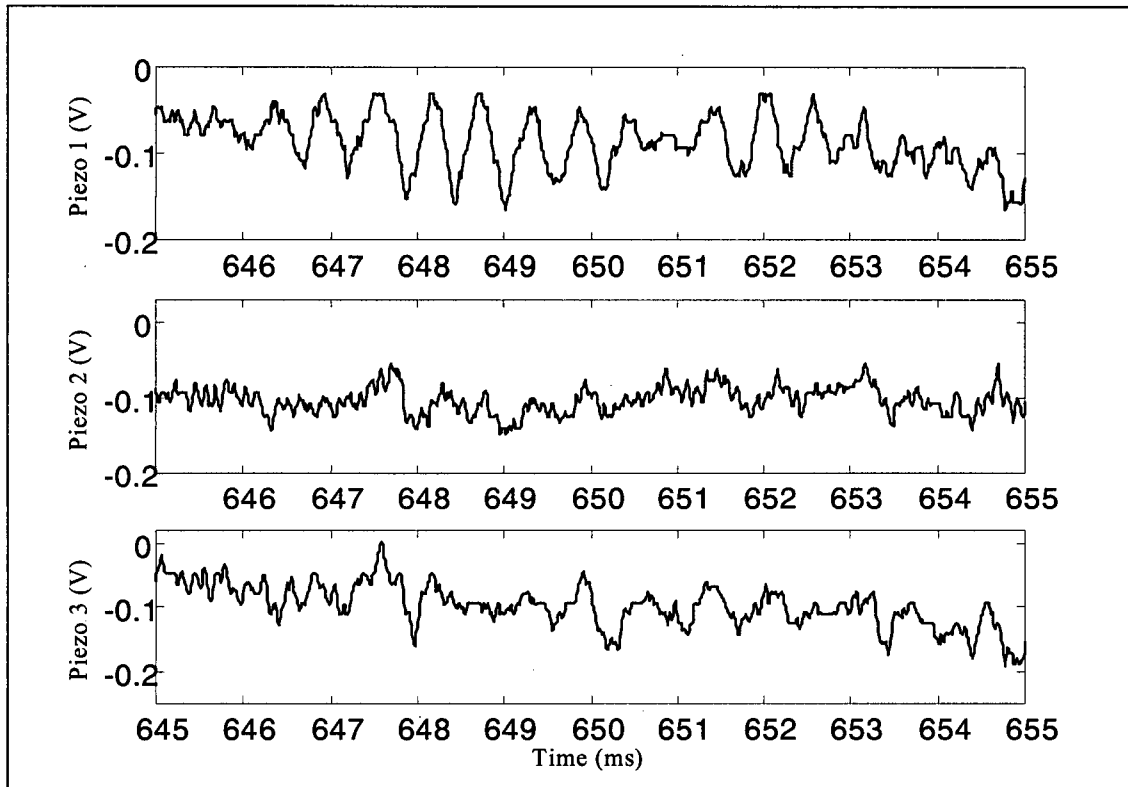


Figure 3.8 Signals from piezo elements during refiner operation. Bar passing events cannot be distinguished as vibrations dominate the signal.

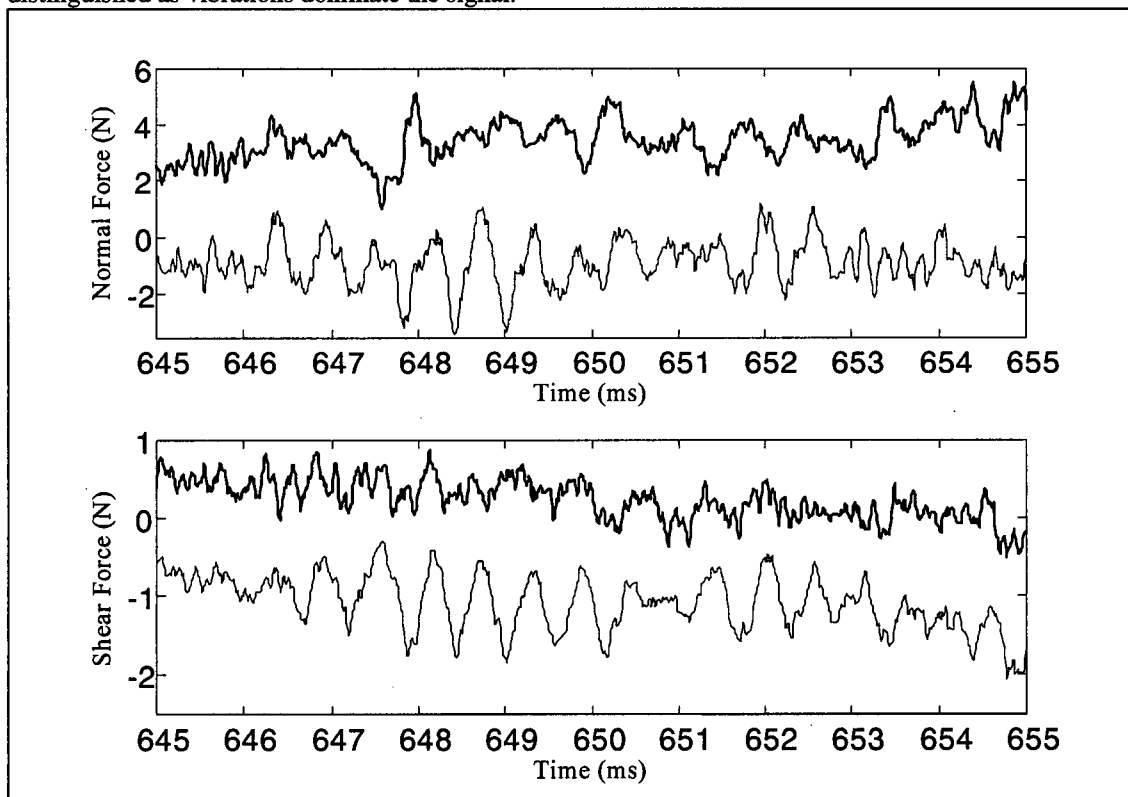


Figure 3.9 Refining forces derived from the above signals. The fine line corresponds to the forces calculated from piezo elements 1 and 3, while the bold line uses the combination of piezo elements 2 and 3.

nature. With the bar passing frequency at 3.6 kHz, the time between bar passing events is 0.28 ms, and no such events can be distinguished from the trace, neither in the piezo signals nor in the force trace.

An interesting feature can be seen in Figure 3.10, where the forces are plotted for 1 second of refiner operation. The periodic variation of the force trace corresponds exactly to the refiner's rotational speed. This is due to the run-out on the rotor plate, which effectively causes a cyclic variation in the plate clearance. The pulp between the plates thus sees a periodic, varying level of compressive strain, and this comes through in the force reading.

It should be noted that the forces calculated from the combination of piezo elements 1 and 3 differ from those calculated from combination 2 and 3, in both Figures 3.9 and 3.10. This aspect was not examined in [1] and is discussed in the following section.

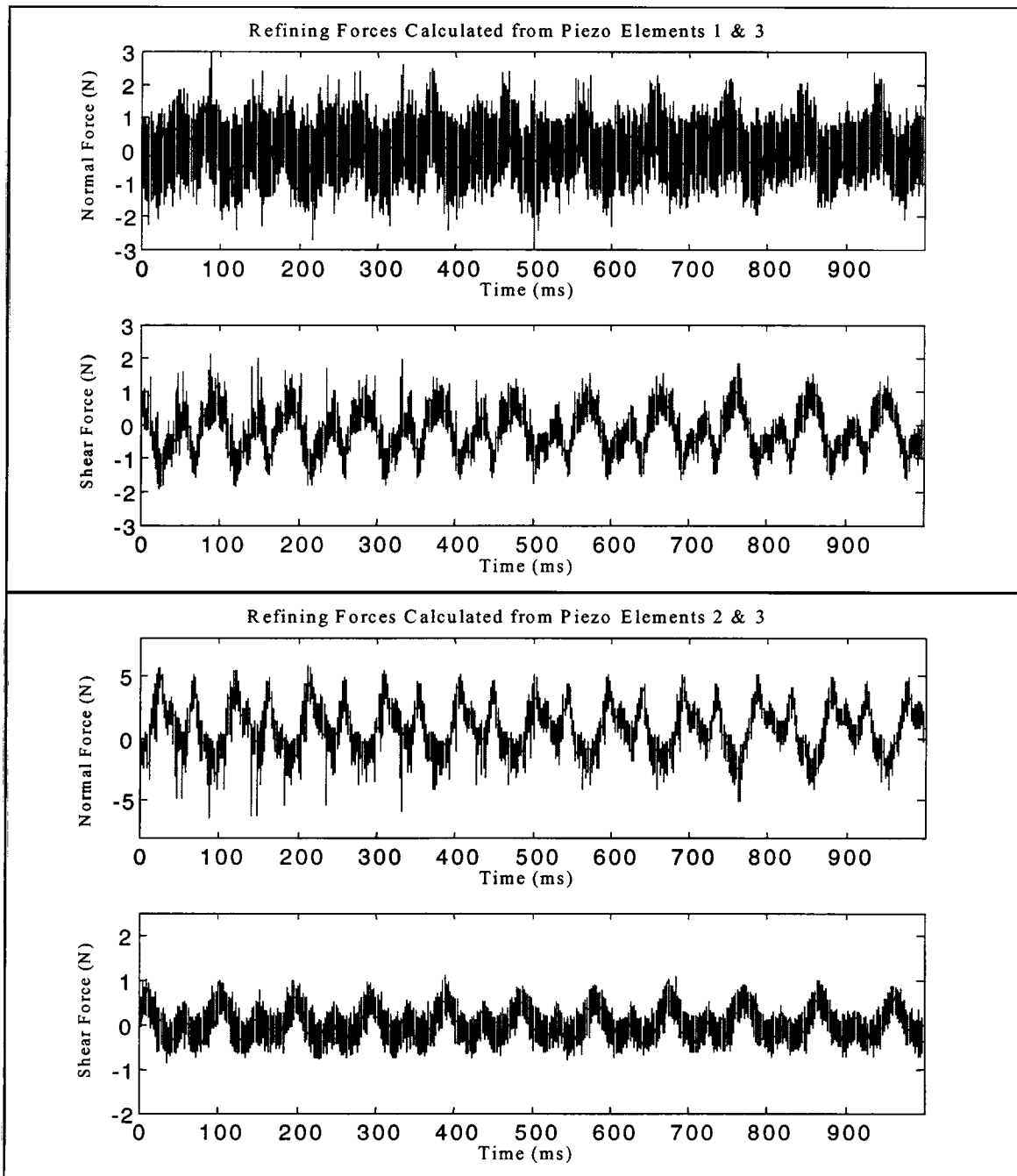


Figure 3.10 The variation of the refining forces over a period of 1 second, as derived from different piezo combinations. The periodic behaviour corresponds to the rotor plate rotation.

3.4 DISCUSSION OF PRELIMINARY TEST RESULTS

3.4.1 CALIBRATION

The equations reported earlier for force determination proved reliable, and the calibration of the sensor was successful (see Figure 3.11). However, some doubts remained with regard to interpreting the piezo element responses in terms of the linear superposition assumption of Equation 3.3. Impact testing using a large-scale model suggested that the assumption was not valid [1], and such a test had yet to be devised and carried out for the prototype. This test is described in Section 4.2.

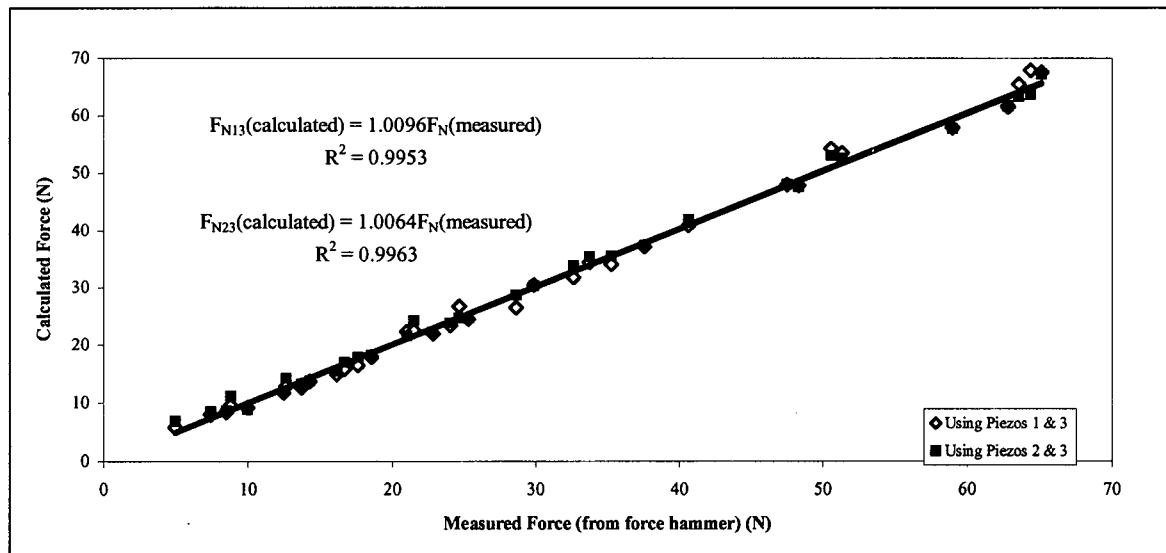


Figure 3.11 Comparison of measured with calculated values of the normal force for impacts applied to the sensor when mounted in the plated.

There was also the noted shortcoming of using the mounting jig to calibrate the sensor, when K-values differed significantly between cases where the sensor was mounted in the jig and those where it was mounted in the refiner plate. It thus became necessary either to verify Equation 3.4, or to devise a method by which the K-value for shear forces could be determined with the sensor mounted in the plate. The latter of the two options was selected, and this is also described in Section 4.2.

3.4.2 DYNAMIC BEHAVIOUR

Of all the aspects of sensor behaviour that were studied in these tests, its vibration characteristics emerged as the area most in need of improvement. The sensor's low natural frequency was the reason for the vibration problems, as explained earlier. Given that the bar passing frequency was 3.6 kHz, and higher frequency components were present in the excitation, a sensor capable of measuring forces in such an environment would need a significantly higher natural frequency than that of this design. Ideally, an overdamped system would also be desirable.

The forces experienced could not be determined with any certainty, neither qualitatively nor quantitatively, not only due to the vibrations, but also due to the fact that signals from piezo elements on vertically opposite sides of the sensor probe were not consistent with expectations. To clarify this point, consider the case shown in Figure 3.12. Assuming that the dominant factor controlling the piezo signal is the normal stress in the y-direction, as piezo element 1 is extended (relative to the preloaded state), its signal should be positive, while piezo element 2, being compressed, should give a negative signal. Therefore, we would expect piezo elements 1 and 2 to exhibit signals of opposite sign at all times (and the same would be expected of piezo elements 3 and 4). In reality, this was not the case (see, for example, Figure 3.8 in previous sections).

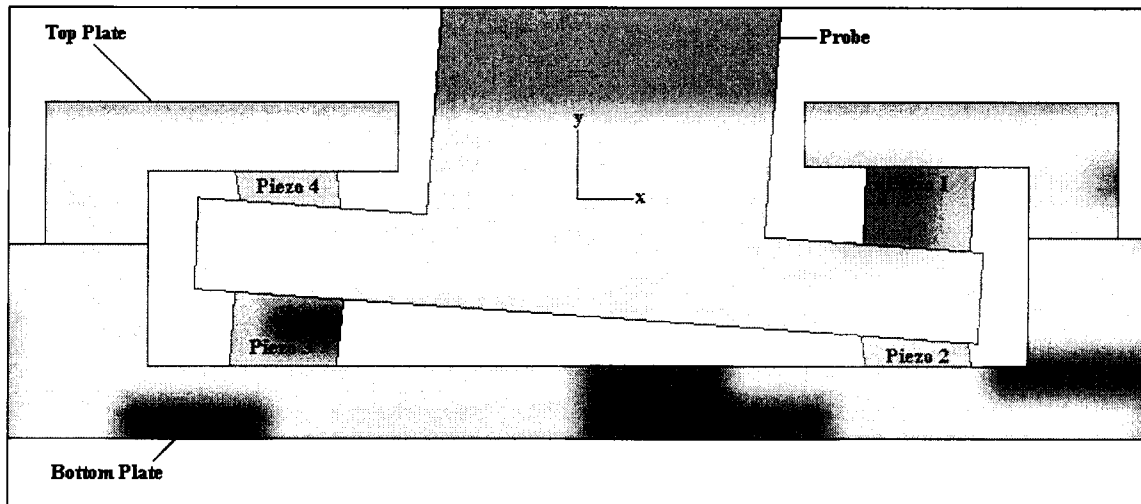


Figure 3.12 Exaggerated diagram showing how the piezo elements deform as the probe is displaced.

One possible explanation for this is that the piezo signals are not only dependent on the normal stress experienced by the elements, but also on shear stresses to a significant extent. Although such a ferro-electric material behaving ideally would not respond to shear stress, it was confirmed that the elements used here were not behaving ideally, as the polarization direction of some parts of the crystal structure were not perfectly aligned with the poling direction [1]. Another possible explanation for the discrepancy between piezo element pairs is that the sensor housing was not perfectly rigid, contrary to earlier assumptions. Relative deformation of the top and bottom plates of the housing would not only explain this, but would also account for the discrepancy between the natural frequency predicted by the finite element model and the value observed experimentally. Subsequent testing confirmed this suspicion, as will be explained in the following chapter.

3.4.3 SENSOR FABRICATION

Piezo ceramic elements would often crack during sensor assembly, and imperfections in the machined finish of the sensor housing were seen as the root of the problem. The

piezo elements would effectively rest on ridges left by the machining tools, and would thus bend and break when the preloading screws were tightened. The lack of good contact between the piezo surfaces and the top and bottom plates was also suspected to reduce the stiffness of the assembly.

To compound the problem, the piezo elements' dimensions (most importantly the thickness in the y-direction) varied significantly from one element to the next. This caused further difficulties in keeping the top and bottom plates parallel during assembly, and made it hard to ensure that all piezo elements saw the same preload.

All of the issues explained above led to the conclusion that significant modifications to the sensor were required before a reliable refiner force measurement would be possible. The following chapter is dedicated to the necessary modifications and their effects on the sensor's behaviour.

4. MODIFIED SENSOR DESIGN

In an effort to address the problems with sensor performance that were outlined in the previous section, several design modifications were examined. Considerable efforts were also devoted to finding the cause of the low natural frequency of the sensor. These steps led to an improved sensor design which is presented in this chapter. Improvements to the calibration procedure were also necessary, as was the testing of certain assumptions. The impact tests to this end and a new calibration method are also presented here.

4.1 DESIGN MODIFICATIONS

4.1.1 MACHINING OF HOUSING PARTS

In order to improve the surface finish of the sensor housing, a new housing design was proposed in which the square recesses in the top and bottom plates were replaced by circular recesses. This was done after noting that the surface finish defects were largely tool marks left by the passage of the small end mill used to machine the square recesses. This problem is avoided with the new design, as the circular recesses can be bored directly with one pass using a large end mill of the desired diameter. This change is illustrated in Figure 4.1. With this modification, it also became more practical to use four screws to hold the top and bottom plates together. This would also stiffen the housing and help ensure that the top and bottom plates were parallel during sensor assembly.

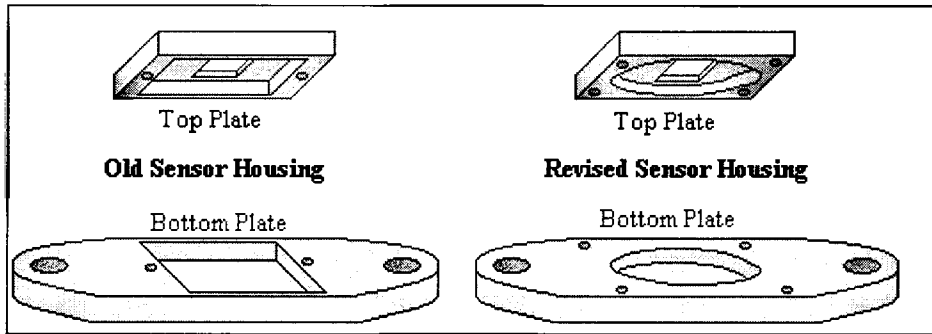


Figure 4.1 Sensor housing design changes.

4.1.2 PIEZO CERAMIC ELEMENTS

To increase the stiffness of the sensor system, and thus raise the sensor's natural frequency, it was decided to use wider piezo elements. The new piezo elements were 2 mm wide (twice the original width in the x-direction according to Figure 3.1), and identical to the original elements in other dimensions. For each sensor built, careful attention was given to the selection of the piezo elements prior to sensor assembly to ensure that each piezo element's thickness (dimension along the y-axis) was within ± 0.01 mm of the others.

4.1.3 INSULATING MATERIAL

Attention was also given to the selection of material used to insulate the piezo elements from the metal parts of the sensor. The different materials considered were scotch tape, mica and alumina coating. The first, a 3MTM-brand scotch tape, had the advantages of being a cheap, effective and quick solution. The tape layer provided ample insulation, but its stiffness was unknown and subject to some doubt.

Layers of mica were also considered for insulation, but were rejected, as their use required a greater amount of glue. The added thickness due to the extra glue and mica

layers was deemed too large, and was difficult to control precisely. This caused difficulties in ensuring that the top and bottom plates of the housing were parallel, and also lowered the stiffness of the system.

It was postulated that using a thinner, stiffer insulation layer could improve the vibration characteristics of the sensor. To this end, an alumina coating was applied to a set of sensor parts. This coating is expected to have a higher modulus of elasticity than the tape and was about half as thick, both contributing to higher support stiffness for the probe. However, using the tape instead of the coating did not appear to reduce the first natural frequency at all, and so it was concluded that the choice between these two was not a limiting factor in the design's lowest mode of vibration.

The changes described up to this point shifted the sensor's first natural frequency from 2.5 kHz to 8 kHz (see Figure 4.2).

4.1.4 HOUSING SUPPORT

As explained in section 3.4, the individual piezo element signals did not behave as expected, and we suspected that this might be due to deformation of the sensor housing. To determine whether such deformation was taking place, shims were used to obstruct any deflection of the top and bottom plates. These shims (made from mica) were used as shown in Figure 4.3, to sandwich the sensor. A side effect of this modification was to increase the preload on the piezo elements, which reduced the sensor's sensitivity, but not to a problematic extent. The addition of shims alone raised the natural frequency

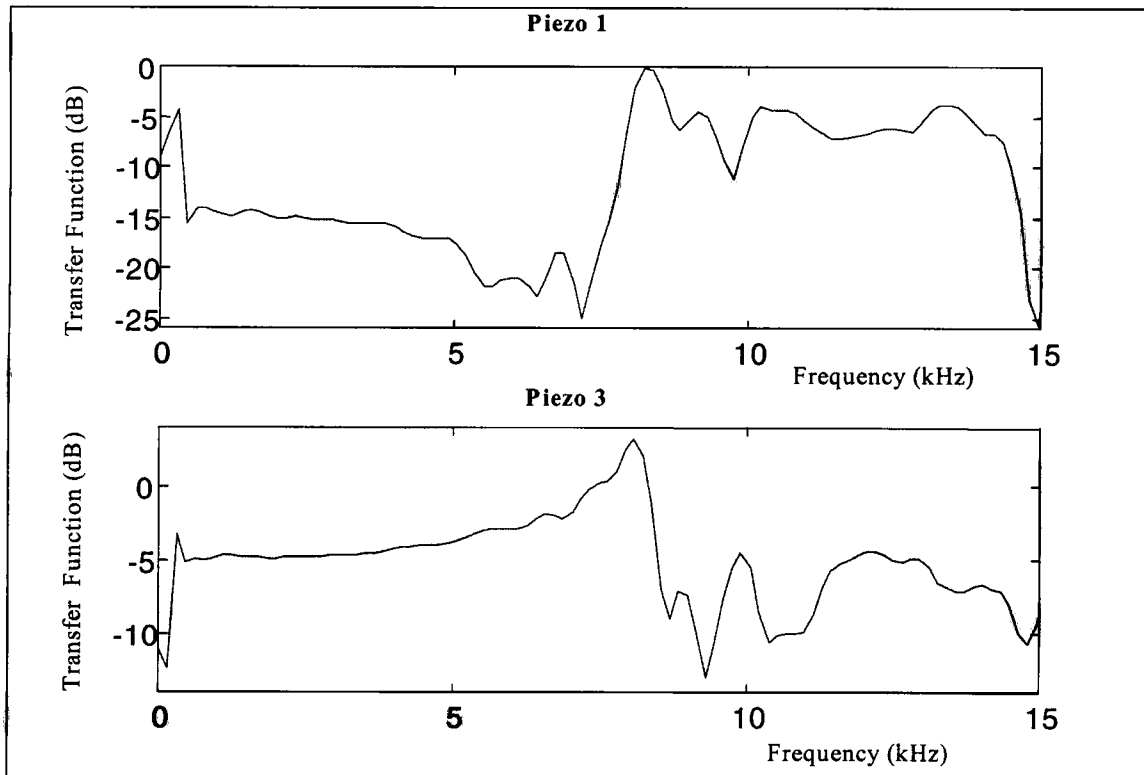


Figure 4.2 Average transfer functions for piezo elements 1 and 3, with the new housing modifications and the 2 mm-wide piezo elements.

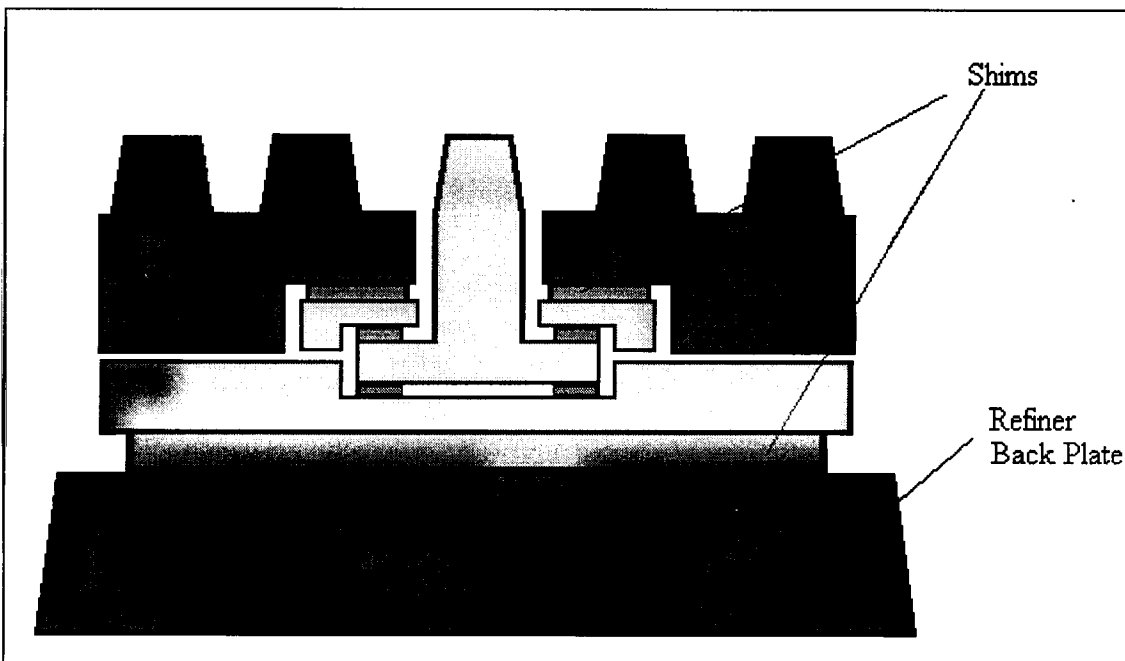


Figure 4.3 Sensor used in conjunction with shims in order to inhibit deformation of housing.

of test sensors to the 12-15 kHz range. The effect of placing shims against the top plate was greater than that achieved by placing shims against the bottom plate, implying that

the top plate deformed more readily than the bottom plate. This explains why transfer functions of piezo elements 2 and 3 (which are between the probe and the bottom plate) were generally better than those of 1 and 4 (which were against the top plate). Although transfer functions of piezo elements 1 and 4 were improved with the use of shims, they still did not behave as well in the frequency domain as piezo elements 2 and 3, which generally exhibited smoother transfer functions and higher natural frequencies. Therefore the piezo element combination 2-3 is preferred for force measurement.

4.1.5 DAMPING MECHANISMS

Attempts were made to add a damping mechanism to the system in different ways. The void regions of the sensor housing were filled with different combinations of latex and silicone, but none of these attempts at internally damping the system made much difference.

However, when external damping mechanisms were employed, a considerable effect was seen in the free vibration behaviour. Latex pads were added to the shims to dampen the vibrations due to the deformation of the housing, and the effects are shown in Figure 4.4. The damping factor increased from approximately 1% to 7% upon adding the latex pads.

4.1.6 FURTHER STIFFENING OF SENSOR

Finally, we tried filling the void regions in the sensor housing with epoxy, to stiffen the system even further. This last modification, in combination with all the others mentioned above, gave test sensors whose first natural frequencies were in the range 25-30 kHz (see Figure 4.5).

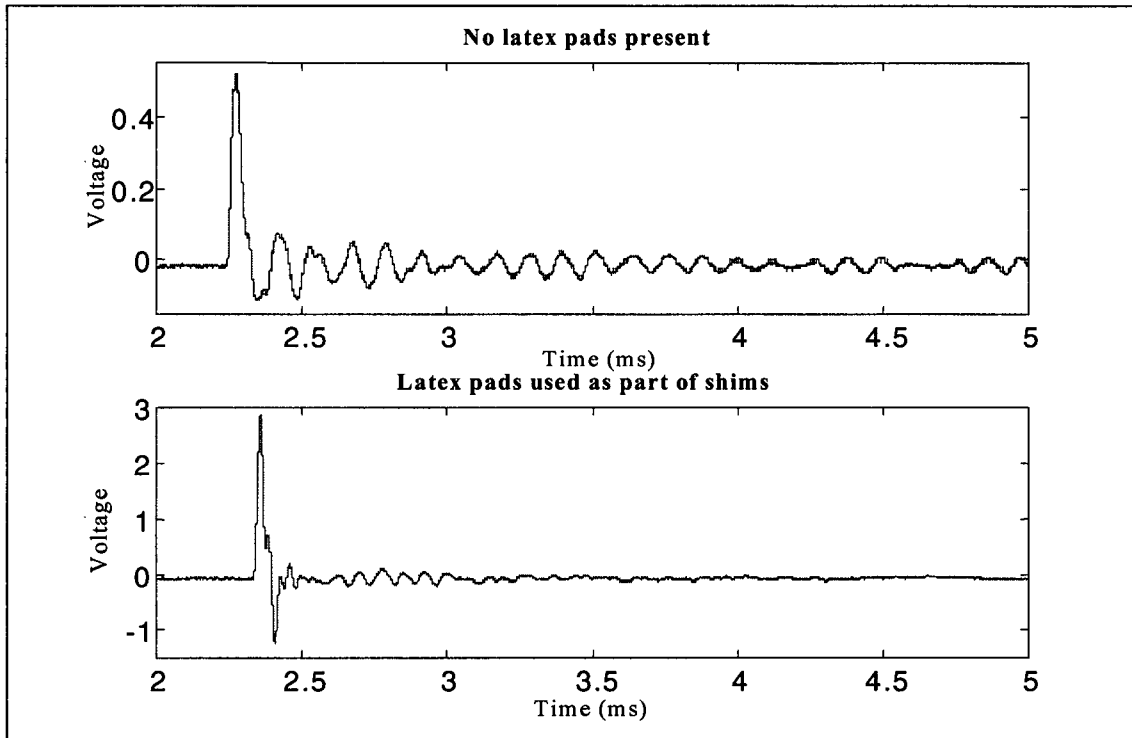


Figure 4.4 Effect of using latex pads in conjunction with layers of mica in the shims. The time domain signal of piezo element 3 is shown in response to an impact from the force hammer.

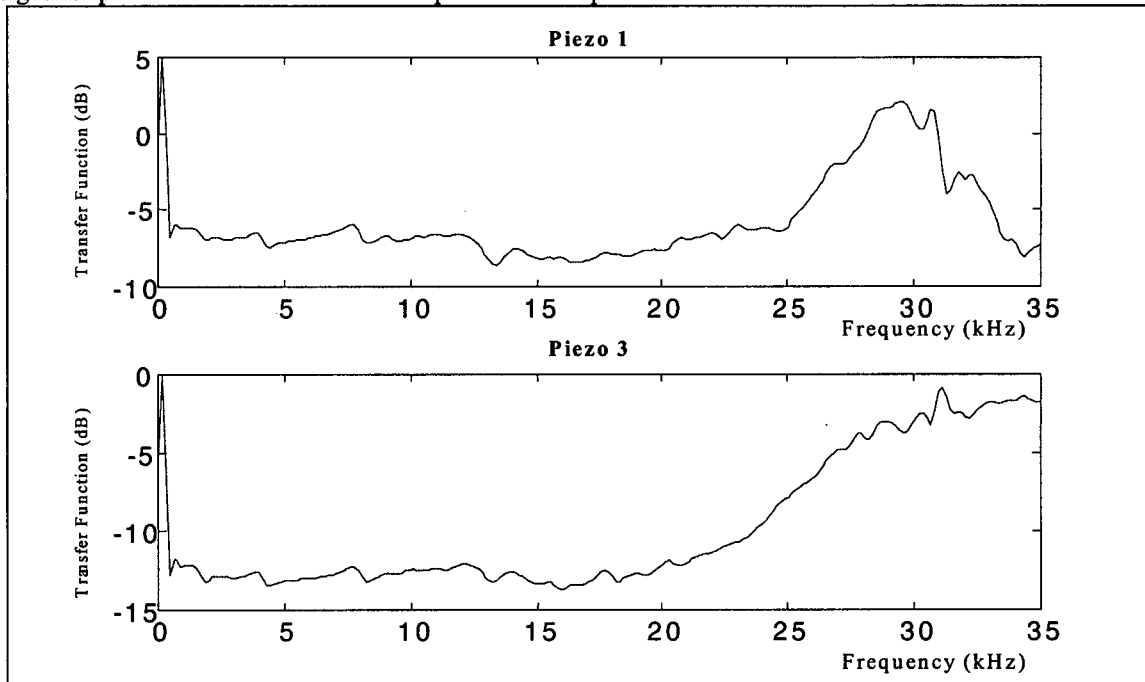


Figure 4.5 Transfer functions for piezo elements 1 and 3, for revised sensor design with all new modifications.

4.2 IMPACT TESTS AND CALIBRATION

Aside from the work summarized in the previous section, other aspects of the sensor's behaviour were examined. The objectives of the tests presented in this section were:

- To test the response of the sensor to combined normal and shear loads,
- To examine how the sensor's response changes when varying the position of impact on the probe,
- To develop a more reliable calibration procedure, in which all calibration coefficients are determined with the sensor mounted in the refiner plate.

4.2.1 SENSOR RESPONSE TO COMBINED NORMAL AND SHEAR LOADS

When pulp flocs are impacted by bars during refiner operation, the resultant force is a combination of a normal and a shear component. Thus far, it has been assumed that the sensor's response to such a force would be the sum of its response to the pure vertical component plus the response to the pure horizontal component of the force. This was mathematically stated as:

$$V_i = K_{iN} F_N + K_{iS} F_S = F(K_{iN} \cos\theta + K_{iS} \sin\theta) \quad (3.3)$$

where F is the magnitude of the resultant force and θ is the angle that its line of action makes with the perpendicular to the top face of the probe (i.e., the angle made with the y-direction, as defined in Figure 3.1). If the refining forces are to be calculated as such, then a confirmation of the above equation is required.

To this end, wedges of different geometries were constructed from aluminum and glued to the top face of the probe, so that repeatable impacts could be applied to the sensor at precise angles (see Figure 4.6). As the wedges were made from aluminum, their individual masses were very small (ranging from 0.02 to 0.05 g), generally below 3% of that of the sensor probe (weighing 2 g), and so any effects of having increased the probe mass were not significant.

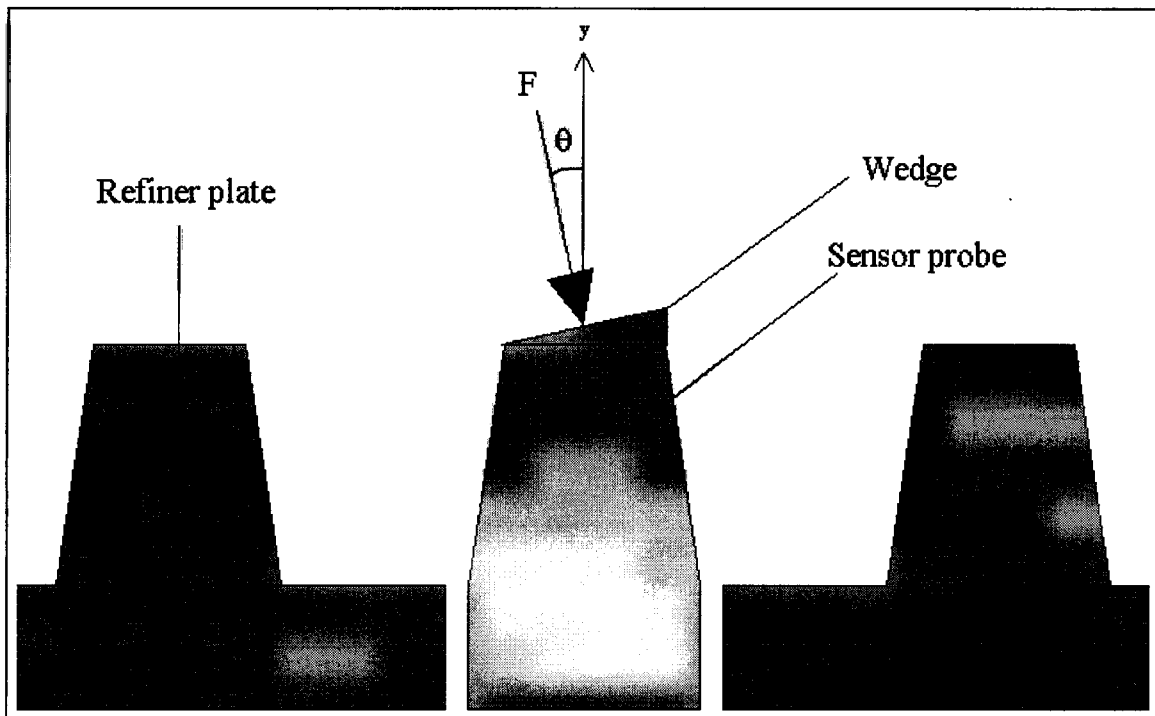


Figure 4.6 Impacts administered at different angles by using aluminum wedges.

For every angle θ at which the probe was impacted, the piezo elements responses were seen to be proportional to the magnitude of the impact force,

$$V_i = K_{i\theta} F \quad (4.1)$$

where $K_{i\theta}$ is the experimentally determined constant of proportionality.

K_{iN} was determined as before, by impacting the sensor vertically ($\theta = 0^\circ$), and if the assumption of linear superposition holds, then K_{iS} could be determined from:

$$K_{i\theta} = K_{iN} \cos\theta + K_{iS} \sin\theta \quad (4.2)$$

or, rearranging,

$$K_{iS} = \frac{K_{i\theta} - K_{iN} \cos\theta}{\sin\theta} \quad (4.3)$$

If the assumption of linear superposition is valid, the values of K_{iS} calculated from Equation 4.3 for different angles should all be the same. The results are summarized in Table 4.1. It should be noted that piezo element 2 cracked during the assembly of this sensor, and so no signals from this piezo element are included in this analysis. Aside from the values in the shaded regions of the table, the K_{iS} values calculated for different angles are close. The exception to this are those values in the shaded regions, which were inaccurate because at this particular angle, the sensor response was small ($K_{i\theta}$ changes sign in these regions) and the signal-to-noise ratio was low, hence the discrepancies in the K_{iS} values.

Angle (°)	Piezo 1		Piezo 3		Piezo 4	
	$K_{1\theta}$ (mV/N)	K_{1S} (mV/N)	$K_{3\theta}$ (mV/N)	K_{3S} (mV/N)	$K_{4\theta}$ (mV/N)	K_{4S} (mV/N)
0	43.3	-	-70.2	-	48.6	-
10	57.0	82.7	-42.1	155.7	28.3	-112.7
20	71.8	91.0	16.9	242.3	-9.4	-161.0
30	86.4	97.8	26.9	175.4	-18.9	-122.0
40	94.6	95.6	50.9	162.8	-31.3	-106.6
	Ave K_{1S} = 91.8 mV/N K_{1N} = 43.3 mV/N		Ave K_{3S} = 164.6 mV/N K_{3N} = -70.2 mV/N		Ave K_{4S} = -113.7 mV/N K_{4N} = 48.6 mV/N	

Table 4.1 K-Values determined by impacting the sensor at different angles

Using the method outlined in Appendix C, the average K-values can be used to derive equations to calculate the normal and shear forces from a combination of two piezo elements. For the piezo combinations 1-3 and 1-4, these are:

$$\begin{aligned} F_{N13} &= 12.12V_1 - 6.76V_3 \\ F_{S13} &= 5.17V_1 + 3.19V_3 \end{aligned} \quad (4.4a,b)$$

$$\begin{aligned} F_{N14} &= 12.12V_1 + 9.78V_4 \\ F_{S14} &= 5.18V_1 - 4.61V_4 \end{aligned} \quad (4.5a,b)$$

where V_1 , V_3 and V_4 are the magnitudes of the piezo element signals in volts.

The true normal and shear forces on the sensor probe, as measured by the hammer, are:

$$F_N = F \cos\theta \quad (3.2a)$$

$$F_S = F \sin\theta \quad (3.2b)$$

We can now compare these true forces with those calculated from the sensor signals using Equations 4.4 and 4.5. Figures 4.7 and 4.8 show the calculated forces plotted against the actual forces for 100 impacts at the different angles listed in the table above. A linear regression performed on the two sets of data gave slopes and correlation coefficients very close to 1 for both graphs, indicating that a measure of the forces with the assumption of linear superposition is reliable. Comparing the data to the equal-value lines in the figures, piezo combination 1-3 appears to slightly overestimate the normal force and underestimate the shear force. These deviations from the equal value lines on the graphs are explained by the fact that piezo elements 1 and 4 are in use here, and they are known to give less accurate results than piezo elements 2 and 3, as explained earlier. Another source of error was the difficulty in ensuring that the line of action of the impact forces passed through the centre of the probe tip. This caused more significant errors in the impacts at the larger angles, as is evident from the string of points that lie below the equal value line in Figure 4.7, which represent the data for $\theta = 40^\circ$.

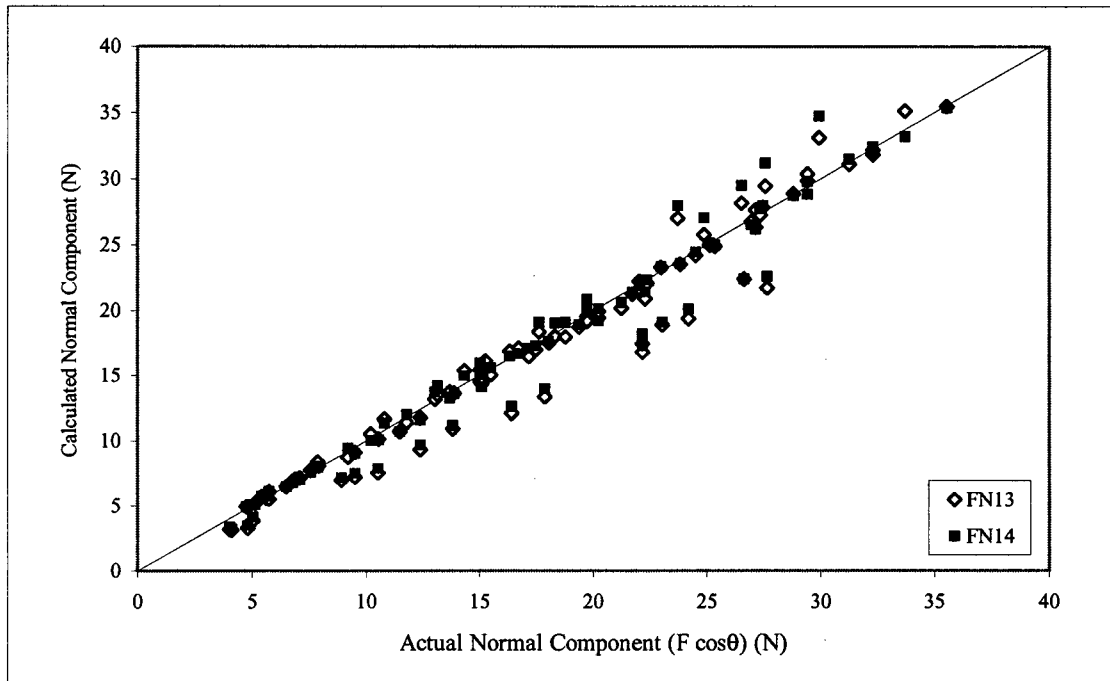


Figure 4.7 A comparison of the true normal component with values calculated from Equations 4.4a and 4.5a.

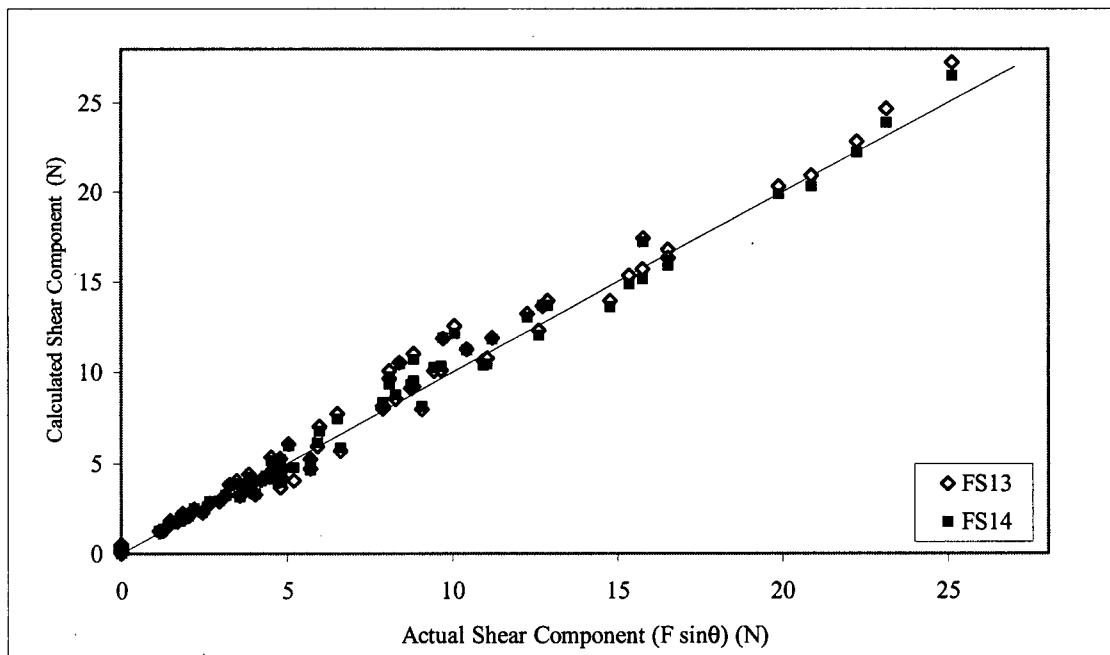


Figure 4.8 A comparison of the true normal and shear components with those calculated from Equations 4.4b and 4.5b.

The validity of the linear superposition assumption can now be used in order to calibrate the sensor in the plate, as both K_{iN} and K_{iS} can be determined with the sensor mounted in the refiner plate, thus solving the problem of having to use the mounting jig.

4.2.2 EFFECT OF IMPACT POSITION

One of the major objectives of this work is to examine the refining forces and their variation over the duration of a bar passing event when a floc is trapped between the sensor and a rotor bar. During such an event, a rotor bar passes over the sensor, trapping a floc at the leading edge of the probe where the forces begin to act. As the rotor bar moves over the probe, the centre of pressure moves away from the leading edge, right across the width of the probe's top face, to end up at the trailing edge of the probe tip. It is therefore important that the sensor response does not change significantly with the point of application of the loads, so that a meaningful force profile over the bar passing event can be acquired.

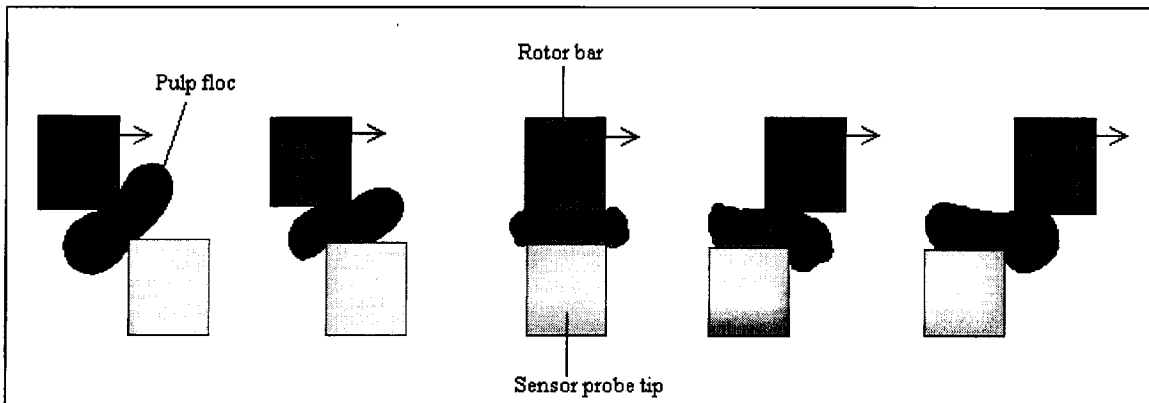


Figure 4.8 The moving load during a bar passing event. As the rotor bar moves across the top of the probe, so does the centre of pressure.

The experiment conducted to study this aspect of the sensor behaviour consisted of dividing the top face of the probe into a grid of 15 squares, each 1 mm x 1 mm in size,

and vertically impacting the centre of each square several times with the force hammer to determine a K-value for each piezo element in each location.

The results for piezo elements 2 and 3 are shown in Table 4.2. As one would expect, there is a small variation in the voltage of the signal per unit force of impact along the width of the probe (as the moment arm of the impact relative to each piezo element changes along the x-direction). There is little effect of moving the impact position along the length of the probe (z-direction), as shown by the low standard deviations reported in the table. Thus we can conclude that K_{iN} undergoes only small changes with varying impact position (mostly within 10% of the mean), and that the value measured in the centre of the probe is representative of the mean value.

Similar results were seen when K-values were measured for impacts applied at 30° at different positions on the grid. The sensitivity of the sensor did not vary greatly for the different impact positions, suggesting that K_{iS} is affected in the same way as K_{iN} , and that neither are significantly sensitive to the point of application of the forces in question.

Piezo 2 K-Values					
		x			$\sigma(x)$
		1	2	3	
z	1	0.139	0.145	0.152	0.007
	2	0.140	0.148	0.149	0.005
	3	0.142	0.151	0.152	0.005
	4	0.138	0.149	0.148	0.006
	5	0.143	0.152	0.153	0.006
$\sigma(z)$		0.002	0.003	0.002	
$K_{2N}(\text{mean}) = 0.147 \text{ V/N}$					

Piezo 3 K-Values					
		x			$\sigma(x)$
		1	2	3	
z	1	0.095	0.084	0.079	0.008
	2	0.092	0.086	0.078	0.007
	3	0.093	0.084	0.078	0.007
	4	0.095	0.088	0.077	0.009
	5	0.092	0.087	0.074	0.009
$\sigma(z)$		0.001	0.002	0.002	
$K_{3N}(\text{mean}) = 0.085 \text{ V/N}$					

Table 4.2 Variation of sensitivity (K-values) of piezo elements 2 and 3 with varying impact position on the top face of the probe. All K-values are in V/N, and σ is the standard deviation.

5. REFINING TRIALS

5.1 EXPERIMENTAL SETUP

Refining trials with the improved sensor were performed using the same Sprout Waldron 12-inch atmospheric discharge laboratory refiner that was used for the tests described in Chapter 3. New pulleys and drive belts were purchased to be able to run the refiner at different speeds. Trials were conducted with the refiner running at speeds of 700 rpm and 2560 rpm (full speed) using softwood TMP at an inlet consistency of 16%. For the high speed runs, the pulp was continuously fed into the refiner using a plunger-style feeder, thus maintaining a reasonably stable motor load. This method could not be used for the low speed runs, as the refiner's ability to propel pulp outwards through the refining zone is greatly reduced at lower speeds. Therefore, the pulp was fed in small quantities (about 0.3 kg at a time), and dilution water was injected intermittently via the eye of the refiner to ensure that pulp passed through and exited the refining zone.

The consistency was varied during the low speed tests by adding dilution water. Pulp samples taken from inside the refiner after adding dilution water had an average consistency of 13%. This value is, of course, only approximate, and the technique is useful only for distinguishing between a high consistency (16% without addition of dilution water), and a lower consistency (upon addition of dilution water).

In the high-speed tests, pulp was fed at two different inlet consistencies: 25% and 12%.

All trials were performed using D2B502 plates, which gave a bar passing frequency over the sensor probe of 2 kHz for the low speed runs, and 7.4 kHz at high speed. Data acquisition was carried out on a state-of-the-art 4-channel digital oscilloscope. We sampled 3 piezo signals (from piezo elements 2,3 and 4) and one signal from a tachometer measuring the refiner's rotational speed. The sampling rate was 250 kHz for the low speed tests and 1 MHz for the high-speed tests.

The objectives for these tests were:

- to isolate bar passing events and examine their force profiles
- to observe the variation of normal and shear forces and their relative magnitude upon changing the plate clearance, refiner speed, and consistency.

5.2 REFINING FORCE PROFILES

5.2.1 BAR PASSING EVENTS

Figure 5.1 shows a 5 ms force trace representing the normal and shear forces during refiner operation at 700 rpm. In all such diagrams in this chapter, the normal force is depicted by the bold line, and the shear force by the fine line. Several interesting features are present here. The sharp spikes, occurring at approximately 0.5 ms intervals, are the force profiles of bar passing events. The first and seventh spikes are impacts that last slightly longer than the others. This is a feature of the D2B502 plate pattern (see Figure 5.2), on which all bars have a width of 2.8 mm, except every sixth bar, which has a width of 5.5 mm over the location of the sensor probe. The radial position of the probe

corresponds to the streak visible on the left half of the segment near the outer radius. This is a scratch left by the sensor probe. The larger width of some of the bars at this radial position explains why some peaks are wider in the force profile.

In the case depicted in Figure 5.1, the peak magnitude of the forces varies when we look at successive impacts. This is typical of what was generally observed.

The peak levels were seen to vary quite erratically depending on how the pulp was feeding. This was to be expected, since the magnitude of the forces depends on factors

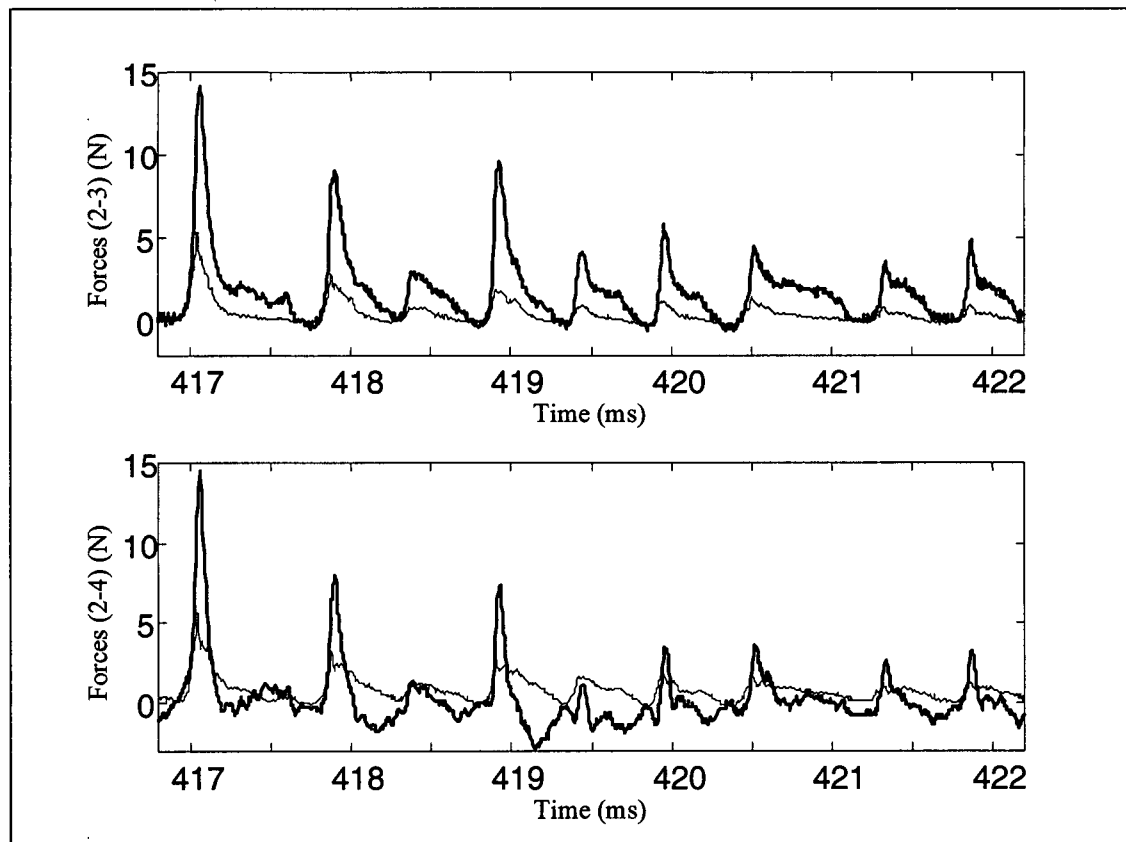


Figure 5.1 Refining normal force (bold line) and shear force (fine line) at 700 rpm as calculated using piezo combinations 2-3 and 2-4.

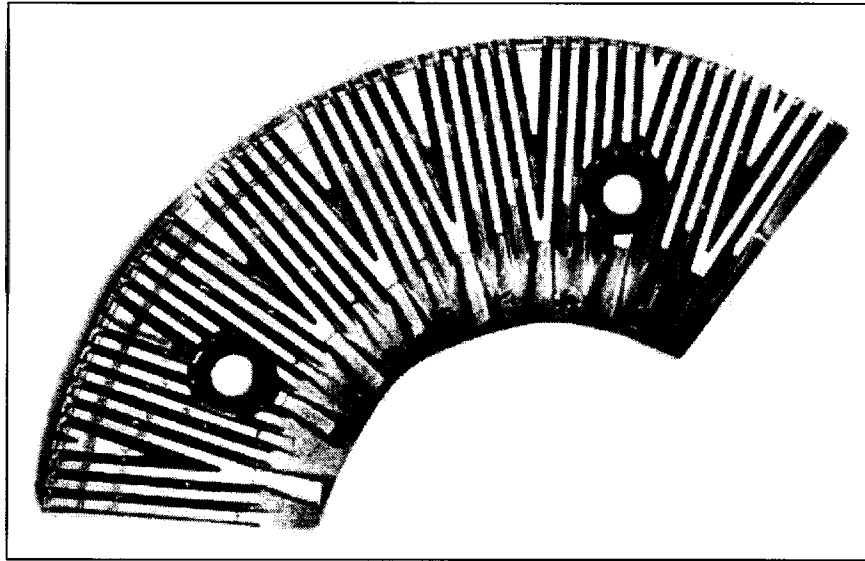


Figure 5.2 One of the three segments of the D2B502 rotor plate (the stator plate segments are identical).

such as the floc size, floc position relative to the bars and floc strength, all of which can vary greatly during normal refiner operation.

Forces calculated from the combination of signals from piezo elements 2 and 4 agree well with those from the combination of 2 and 3 in terms of the magnitudes of the forces. However, as we can see from Figure 5.1, the profiles from the 2-4 combination are somewhat more adversely affected by vibrations, and so the combination 2-3 was regarded as correct, and the 2-4 combination was not used for any force data.

Figure 5.3 shows a close-up of one bar impact.

In general, the force profiles of individual bar impacts were quite clearly defined and were all quite similar in shape. Both the normal and shear forces rise sharply to a

maximum early in the impact, and then fall to a lower level that gradually drops off to zero as the impact ends.

The shear force profiles measured here were similar to those shown by Senger et al. on their low-speed single bar refiner [24], but we saw important differences between the normal force profile measured in the two cases. In the work of Senger et al., the normal

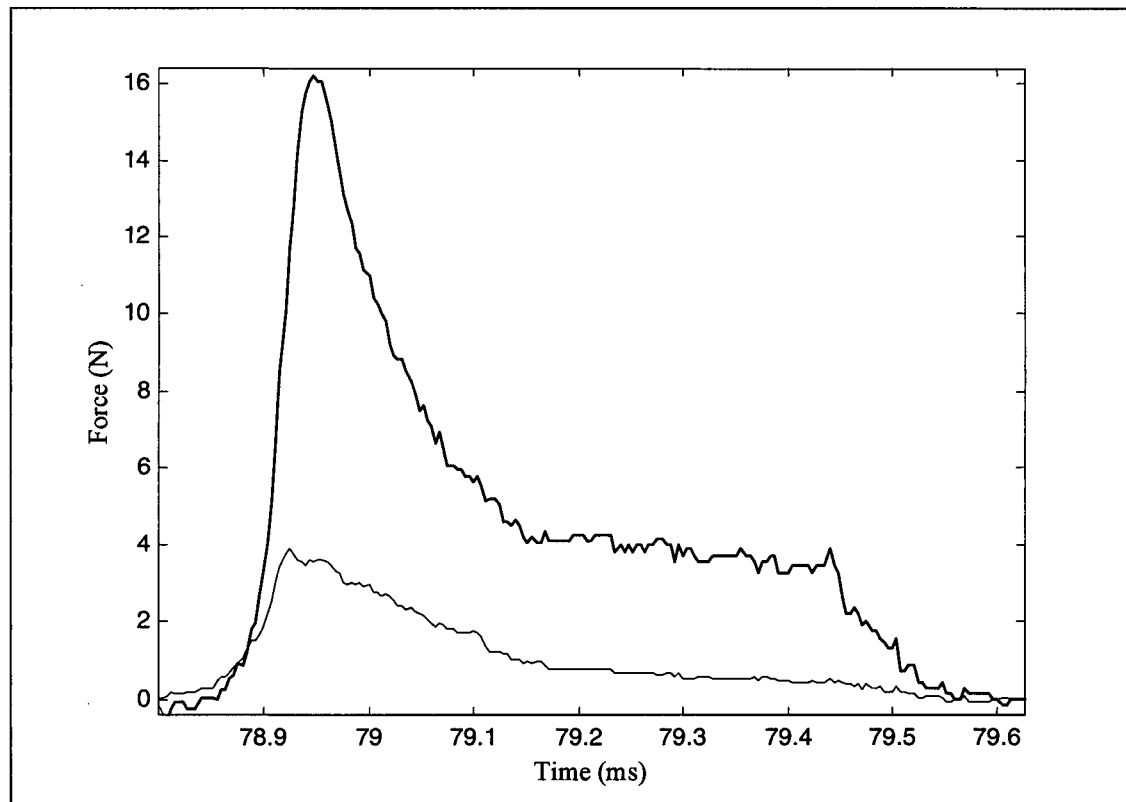


Figure 5.3 The normal (bold line) and shear forces (fine line) due to a typical bar impact.

force profile was essentially triangular and symmetric about the peak value, as the compressive force on the floc rose steadily to reach a maximum when the rotor and stator bars were centred over each other, then dropped steadily to zero as the bars departed each other [24]. In contrast, they also observed that the shear force profile was asymmetric, and attributed this to the action of the corner force. This force component, acting on the leading edge of the bar, rose sharply at the start of the impact, and dropped to zero

halfway through the impact, when the leading edge of the rotor bar reached the trailing edge of the stator bar. Senger et al. observed that the corner force acted almost entirely in the tangential direction. The overall shear force during a bar crossing was thus the sum of the corner force and the friction force (proportional to the normal force), which explained the asymmetry of the shear force profile.

The profiles shown here suggest that the corner force has a component in the normal as well as in the tangential direction. The fact that the corner force has a normal component in our results and did not display one in the measurements performed by Senger [24] at low speed may be an indication that the direction of action of the corner force is influenced by speed. Our results are not sufficient to reach a definite conclusion on this aspect, however, and a more detailed investigation of the effect of refiner speed will be required.

5.3 DATA REJECTION CRITERIA

To investigate how refiner operating conditions affected the forces between bars, we recorded signals representing thousands of bar impacts. Sensor vibrations and other phenomena detrimental to the force measurement were sometimes seen to affect the signals adversely. We therefore had to reject some signals when analyzing records of data, and the criteria used for rejecting such signals are described in this section.

5.3.1 SENSOR VIBRATIONS

The sensor's vibration problems encountered in these tests can be split into two categories:

- Vibrations at 30 kHz, corresponding to the peaks in the transfer functions in Figure 4.5 (resonant vibration).
- Vibrations at 2 kHz, set up by bar passing events at this frequency,

Although some low-magnitude 30 kHz vibrations were present in most signals, these were not often a cause of a loss of accuracy. In some cases, however, the shear force profile was significantly affected by these vibrations. Signals where the amplitude of these vibrations exceeded 10% of the peak magnitude of the shear force were rejected.

An example of such a signal is shown in Figure 5.4.

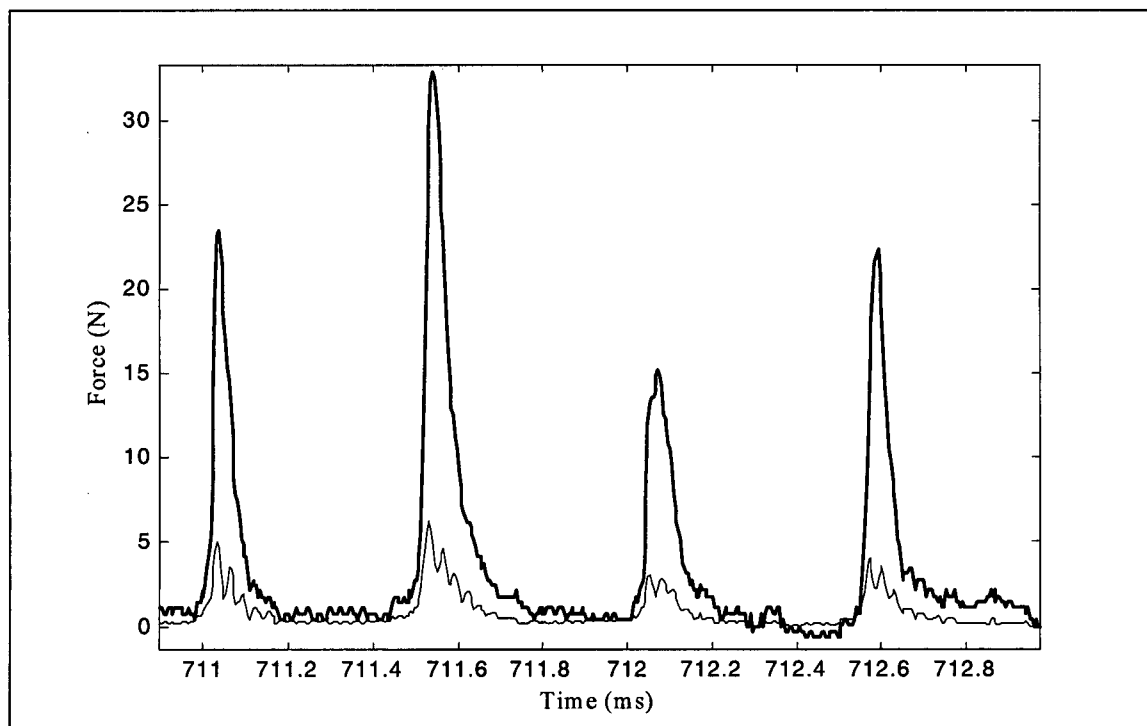


Figure 5.4 An illustration of problematic 30 kHz resonant vibrations of the sensor.

Figure 5.5 shows typical bar passing events at an operating speed of 2560 rpm. Although bar impacts are clearly distinguishable, the true peak magnitude of the forces is subject to some doubts, as the resonant response of the sensor affects the measurement to a significant degree. This is particularly true for the shear force because of its lower peak magnitude. As a result of this problem, none of the signals we collected at high refiner rotational speed could be used for quantitative analysis. This is clearly a shortcoming of the force sensor that needs to be addressed in subsequent design refinements.

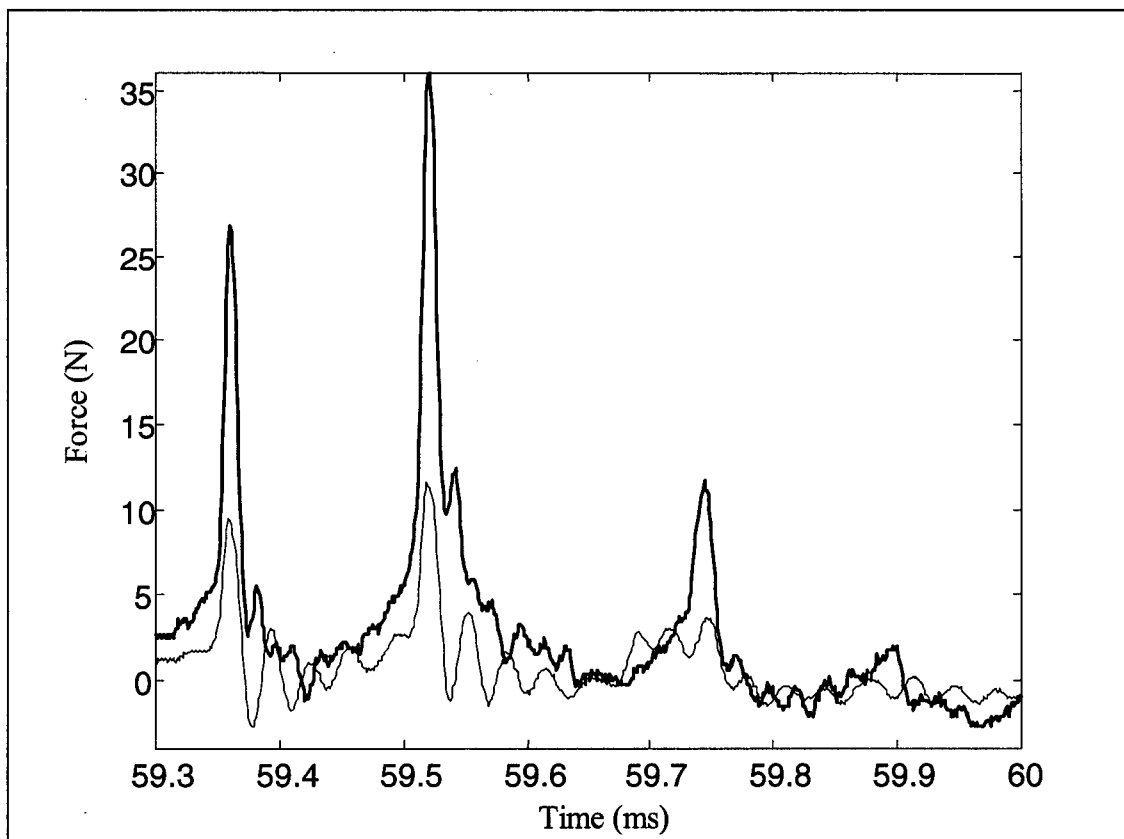


Figure 5.5 Typical force profiles of bar impacts at 2560 rpm.

In some cases during the tests at 700 rpm, the sensor was seen to vibrate at a frequency close to that of the bar passing events. This is shown in Figures 5.6 (a) and (b), where the five consecutive 2.8 mm bars begin to excite the sensor into vibration at approximately 2

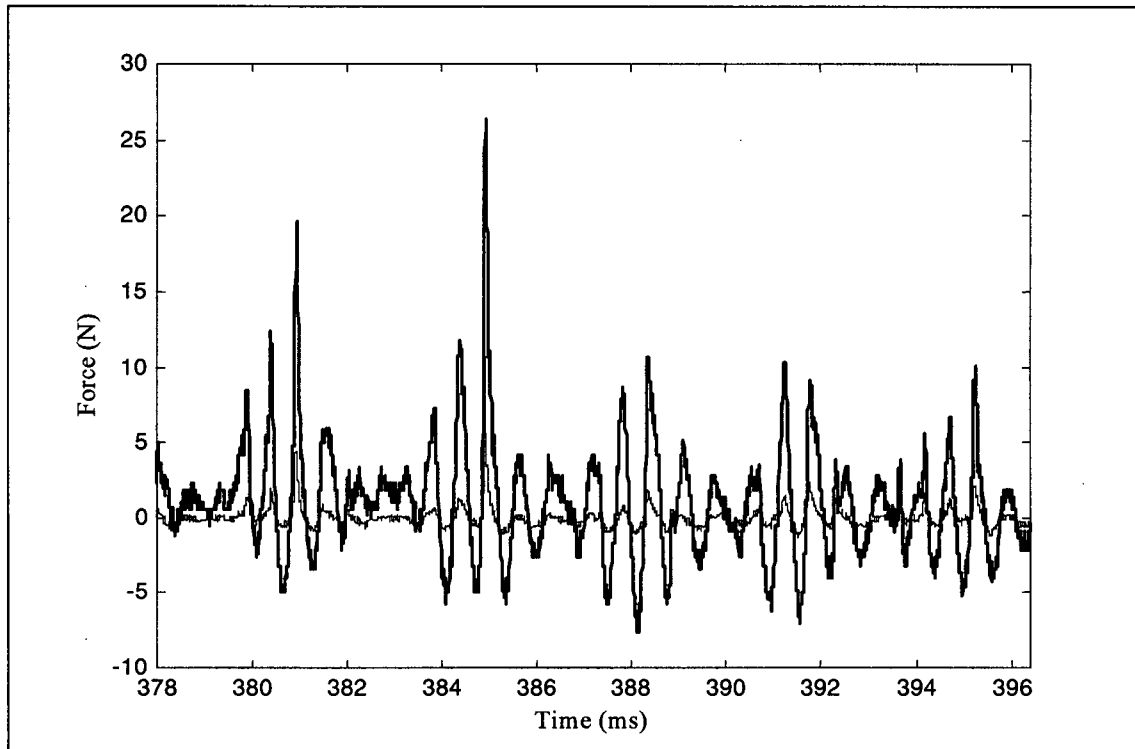


Figure 5.6(a) Sensor vibrations at approximately 2 kHz.

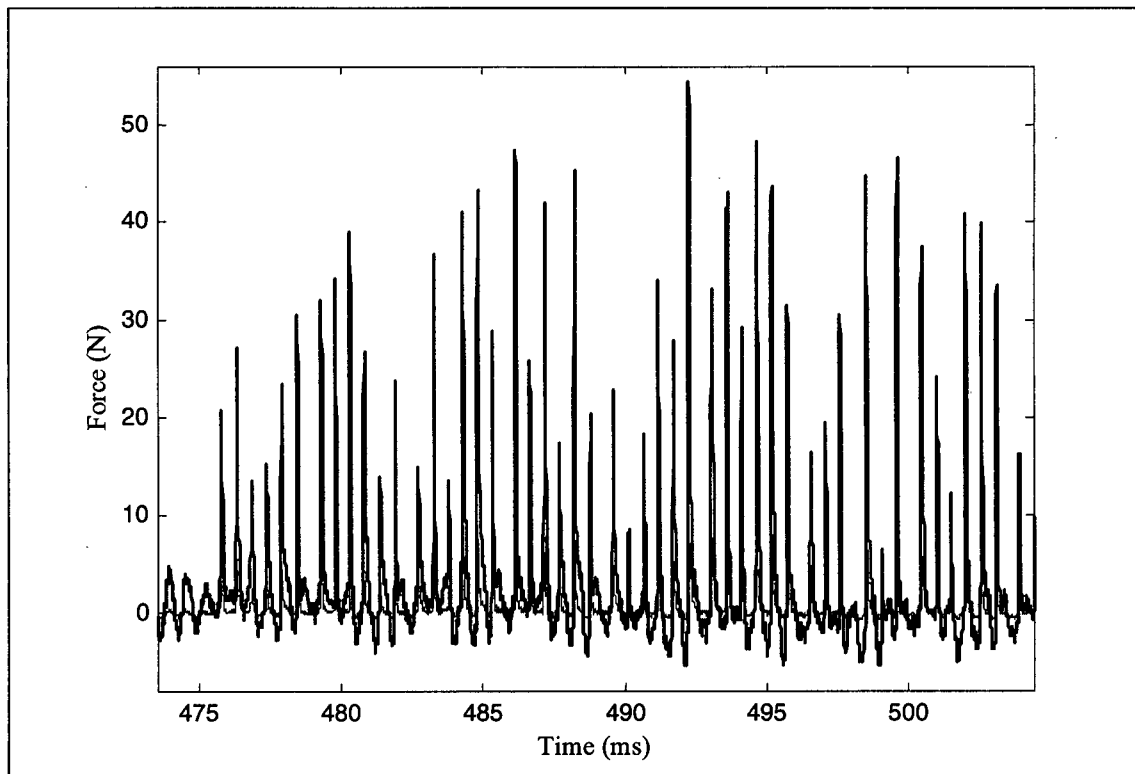


Figure 5.6(b) 2 kHz vibrations grow in amplitude for five successive bar impacts, until a sixth impact from a wider bar reduces their amplitude. This record shows several successive occurrences of this phenomenon.

kHz. As the sensor starts to vibrate in this way, the normal force reading after the bar impact dips down to a negative value, instead of reading zero normal force. This dip increases in magnitude with each bar passing, until the passing of the sixth bar, which is wider than the previous five on the D2B502 plate pattern. The impact with this bar serves to dissipate the energy of the vibration in two ways. As the pulp between this wider bar and the sensor probe is held against the probe for a longer time, this provides a damping mechanism. Also, the passage of the wider bar effectively breaks the periodicity of the excitation, thus temporarily counteracting the vibration (before it is set up again by the next five bars).

It should be noted that these vibrations are only present in the normal force and not in the shear force, suggesting that the sensor probe is vibrating purely with linear motion along the y-axis (as defined in Figure 3.1). These vibrations sometimes become severe enough to significantly affect the force measurement, as shown in Figure 5.6(a), and so all force signals displaying vibrations whose amplitudes were over 10% of the magnitude of the peak force were rejected.

5.3.2 CYCLIC FLUCTUATIONS IN NORMAL FORCE WITH EACH ROTATION

In some of the signals, particularly at high speed, another problem began to appear in the normal force signal. Figure 5.7 shows a part of a signal that seems to be comprised of a low frequency cyclic variation in the normal force upon which the spikes (bar impacts) are superimposed. This cyclic variation corresponds exactly to the period of rotation of the refiner, and again only appears in the normal force.

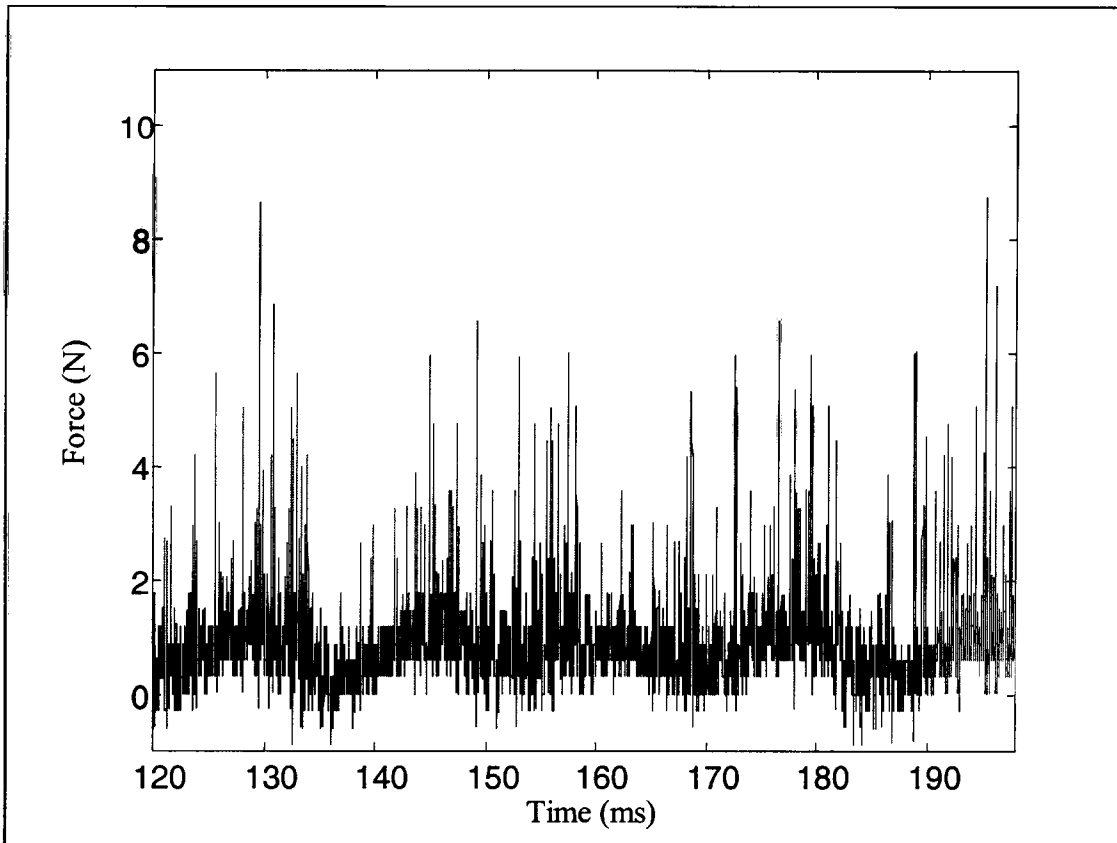


Figure 5.7 Cyclic fluctuations in normal force with each rotation at 2560 rpm.

Figure 5.8 is a plot of the average normal force and the varying plate clearance over one rotation, and there is a clear relationship between the two. As it was not possible to measure the exact plate clearance at the location of the sensor during normal refiner operation, the clearance was estimated by measuring the height of each bar with a dial gauge when the refiner was off. Zero plate clearance was determined with the refiner in operation, by narrowing the plate gap until the highest point on the rotor plate was contacting the highest point on the stator (the sensor probe tip) once per revolution. Thus, the plate clearance setting on the refiner applies to the gap between the highest bar on the rotor and the sensor probe. The clearance associated with other bars passing over the sensor probe can be determined relative to that using the bar heights measured with the dial gauge. Although the determination of the plate clearance using the static

measure of rotor bar heights is not exactly representative of the actual plate clearance during operation, it serves here for a qualitative comparison of the varying plate clearance and the mean normal force. The mean normal force was calculated by taking a moving average of entire revolutions of the rotor during operation, and the similarity in the shapes of the two curves was used to align them with each other in Figure 5.8.

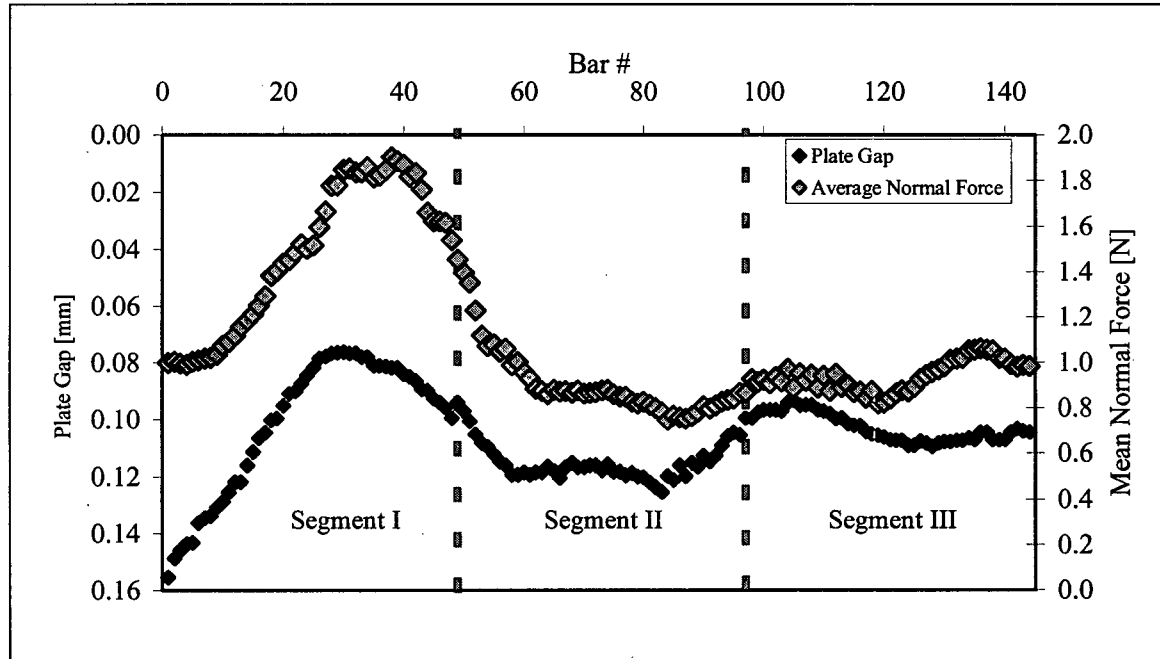


Figure 5.8 Variation of plate clearance and mean normal force through one full rotation of the rotor plate.

The regions of smaller plate gap are associated with higher normal force. This trend most likely occurs because of higher compressive stresses imposed on the pulp network at lower plate gaps. This phenomenon was not restricted to the high speed tests, but was more pronounced there than in the 700 rpm runs.

This phenomenon was considered a problem, as the offset in the normal force could have been due to a change in the sensor preload, with the sensor housing compressed between the refiner plate segment and the back plate (see Figure 4.3). Such circumstances would

skew the force measurement. Pending further tests to determine whether this phenomenon was indeed problematic, signals showing such a shift in the baseline force were excluded from further analysis.

5.4 ANALYSIS AND DISCUSSION

5.4.1 IMPACT STATISTICS

In order to analyze several signals, each containing hundreds of bar impacts (those satisfactorily free of the rejection criteria outlined in the previous section), the signals were processed using MATLAB 5 for Windows. MATLAB programs were used at all stages of signal analysis – for the calibrations and impact testing described earlier, as well as for the calculation of the refining forces from piezo signals and the subsequent analysis of these measured forces. All MATLAB programs (m-files) used in this work are included in Appendix D.

To analyze the force signals from the refiner, a program was designed to isolate individual bar passing events in the signal. This program also extracted the normal and shear force profiles of the events, recorded the peak values of these forces, and calculated the equivalent tangential coefficient of friction as the ratio of these forces. The latter was calculated using two different methods; first by taking the ratio of the peaks of the shear and normal forces (called $\mu_{t,eq}(\text{peaks})$), and second by calculating the ratio of these forces at each point in time during the impact and then taking the average ($\mu_{t,eq}(\text{ave})$) of these values. The beginning and the end of each impact were defined by the points at which the normal force rose above 1 N and fell below it, respectively. The region in between

was extracted from the force signal as the bar passing event. Strictly speaking, the event starts when the force rises from zero and ends when the force falls back down to zero, but a threshold value of 1 N had to be used to prevent falsely registering impacts due to noise or small vibrations in the signal.

A summary of our results is shown in table 5.1.

	Mean Gap (0.001")	Mean Gap (mm)	Peak $F_N(N)$			Peak $F_S(N)$			$\mu_{t,eq}(\text{peaks})$		$\mu_{t,eq}(\text{ave})$		No. of Impacts
			Mean	σ	Max	Mean	σ	Max	Mean	σ	Mean	σ	
No	18	0.46	1.61	0.69	5.24	1.00	0.68	3.86	0.59	0.19	0.55	0.20	210
Dilution	8	0.21	3.63	3.56	26.14	0.99	0.90	6.32	0.29	0.09	0.36	0.11	1302
Water	5	0.13	4.17	4.43	34.96	0.96	1.01	8.52	0.23	0.06	0.27	0.09	1873
	3	0.08	5.19	6.65	46.42	0.92	1.19	8.32	0.18	0.04	0.20	0.06	1557
Dilution	8	0.21	4.17	4.35	38.99	0.96	1.03	10.39	0.23	0.06	0.27	0.09	2716
Water	5	0.13	7.83	6.74	37.67	1.40	1.22	9.13	0.18	0.05	0.21	0.08	716
Added	3	0.08	13.58	11.57	55.33	2.06	1.86	10.83	0.16	0.04	0.18	0.08	996

Table 5.1 Summary of impact statistics for refining runs at 700 rpm (σ is the standard deviation).

As expected, the data shows a clear trend of increasing force with decreasing plate clearance. Lowering the plate clearance causes an increase in the axial thrust on the plates due to an increased reaction force from the pulp between the plates. This also increases the shear force and thus the power consumption.

5.4.2 VARIATION OF SHEAR FORCE WITH PLATE CLEARANCE

While the peak normal force keeps increasing with decreasing plate gap, the peak shear force seems to level off at about 11 N. Noting from the force profiles that the peak shear force is reached very shortly after the start of the impact, it seems reasonable to suggest that the peak is due mostly to the corner force. The ceiling of approximately 11 N would

therefore correspond to the maximum shear force per unit length of bar that can possibly be attained at this speed and range of consistency, which is calculated at 2.2 kN/m. This suggests that there may also be a ceiling in the motor load, which can be estimated using:

$$P = \omega \alpha (F_{SL} L_{bc}) \left(\frac{r_1 + r_2}{2} \right) \quad (5.1)$$

where ω is the refiner speed (in radians per second), α is the fraction of the refining zone area that is packed with pulp, r_1 and r_2 are the inner and outer radii of the refining zone, respectively, F_{SL} is the shear force per unit length, and L_{bc} is the total length of rotor and stator bar edges crossing at any time during refiner operation. This equation assumes that the torque on the refiner's shaft is equal to the moment exerted by the resultant shear force (calculated based on the average shear force per unit length of bar edge) acting at a radial distance halfway between the inner and outer radii of the refining zone. L_{bc} is estimated at 2.3 m (details of this estimate are given in Appendix E), which is approximately half of the total bar length of each of the plates, and α is estimated at 0.76 [26].

Equation 5.1 predicts the aforementioned ceiling in the motor load to be 44 kW for the lab refiner when operating at 700 rpm. For the Sprout-Waldron 60-inch refiner in [25], L_{bc} is estimated at 116 m (using to the method in Appendix E), and this leads to an upper limit in the motor load of 19 MW for the refiner running at 1500 rpm.

These values are somewhat higher than the rated capacity of the motor in each of the two cases, which for the laboratory refiner is 35 kW, and for the 60-inch refiner is 10 MW for

a single refining zone. This estimate of the ceiling in the motor load is nevertheless expected to be higher than anything achieved under normal conditions, as the maximum shear force per unit length was used in the calculation, and this was assumed to act uniformly on all bars under load. In reality, the average shear force per unit length throughout the refining zone will likely always be lower than this, thus drawing less power. The bar coverage fraction α also has a significant effect on this measure, and the value quoted above is a rough estimate at best.

5.4.3 EFFECT OF INJECTING DILUTION WATER

The addition of dilution water at constant plate gap seems to cause an increase in the peak magnitude of the forces, but this trend must be interpreted with caution. The refiner does not feed well at 700 rpm and, prior to the addition of dilution water, relatively few impacts are registered before the pulp fills the grooves and forms a mat on the surface of the plates. The addition of dilution water washes away the pulp on the surface of the plates, which causes a surge in the flow of material through the refiner and, in turn, leads to an increase in both the number and the peak magnitude of impacts measured shortly after. Thus, the effect observed here might be due to an increased capacity to feed material through the refiner, rather than an intrinsic increase in the reaction force of the pulp mat as a result of a change in consistency.

5.4.4 VARIATION OF $\mu_{t,eq}$ WITH PLATE CLEARANCE AND CONSISTENCY

The equivalent tangential coefficient of friction, $\mu_{t,eq}$, taken as the average ratio of the shear to the normal force, are plotted for the different test conditions in Figure 5.9. These values are close to those calculated from the peak values of the shear and normal force

from each impact, and qualitatively behave in the same way, although $\mu_{t,eq}(\text{ave})$ is generally slightly higher than $\mu_{t,eq}(\text{peaks})$. The value of $\mu_{t,eq}$ decreases with decreasing gap, because the shear force starts to level off at the lower plate gaps while the normal force continues to rise.

Adding dilution water decreases the consistency of the pulp suspension between the plates, and this results in a lower value of $\mu_{t,eq}$ at a given plate gap. This is consistent with a trend that has been observed by Isaksson et al. in an industrial refiner, where

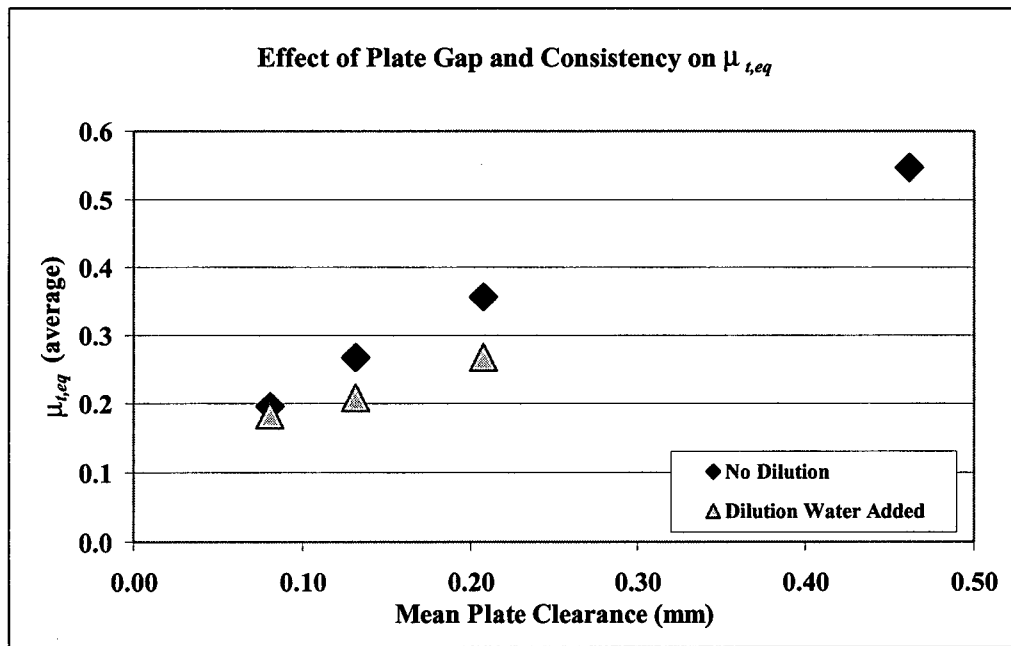


Figure 5.9 Equivalent tangential coefficient of friction vs plate clearance

dilution was seen to reduce $\mu_{t,eq}$ [25]. A similar dependence on consistency was also observed by Senger et al. [24] for measurements carried out on a single-bar refiner at very low speeds and at consistencies ranging from 5% to 80%. However, the effect he observed in this consistency range was less pronounced than the one depicted by our results in Figure 5.9. In contrast, Miles and May reported that $\mu_{t,eq}$ was unaffected by

consistency, based on tests performed using a pilot-scale refiner at discharge consistencies in the range of 15-30% [8].

Although the differences in $\mu_{t,eq}$ for the different consistency cases are barely within the calculated standard deviation, a student's t-test showed that the differences are significant at a 99.9% confidence limit.

5.4.5 RANGES OF MEASURED $\mu_{t,eq}$ AND AVERAGE PRESSURE

For the purpose of comparing the range of measured values of mechanical pressure (due to compressive stress on the pulp between the plates) and the equivalent tangential coefficient of friction, a graph of $\mu_{t,eq}$ against average mechanical pressure is plotted in Figure 5.10. This graph includes data from this work and from several other sources.

The average mechanical pressure for our data was calculated as the ratio of the average peak normal force (from Table 5.1) to the area of the sensor probe tip (15 mm²). For all data aside from that of this work, $\mu_{t,eq}$ was calculated using Equation 2.8,

$$\mu_t = \frac{2P}{h\omega F_m (r_1 + r_2)} \quad (2.8)$$

and the average mechanical pressure was determined from:

$$P_{ave} = \frac{F_m}{A_m} = \frac{F_m}{A_{rz} \lambda \alpha} \quad (5.2)$$

where A_m is the area of the refiner plates bearing the thrust load of the pulp between the plates. This is calculated using the bar coverage fraction, α , along with the proportion of the total refining zone area (A_{rz}) constituted by bar surfaces, represented by the fraction λ .

Assuming identical rotor and stator geometries in all cases, and that bar and groove widths are equal, a value of 0.50 is used for the fraction λ . The values of the constants used for each of the different data sets are given in Table 5.2.

Investigators	ω (rad/s)	r_1 (m)	r_2 (m)	h	α (%)
Atack et al. (S1 & S2)	189	0.376	0.533	1	75.6
Isaksson et al. S1	157	0.45	0.785	1	75.6
Isaksson et al. S2	157	0.51	0.785	1	75.6
Miles & May	126	0.355	0.457	2	16

Table 5.2 Values of constants from different sources for use in Equation 2.8 (S1 and S2 refer to primary and secondary stage processes, respectively).

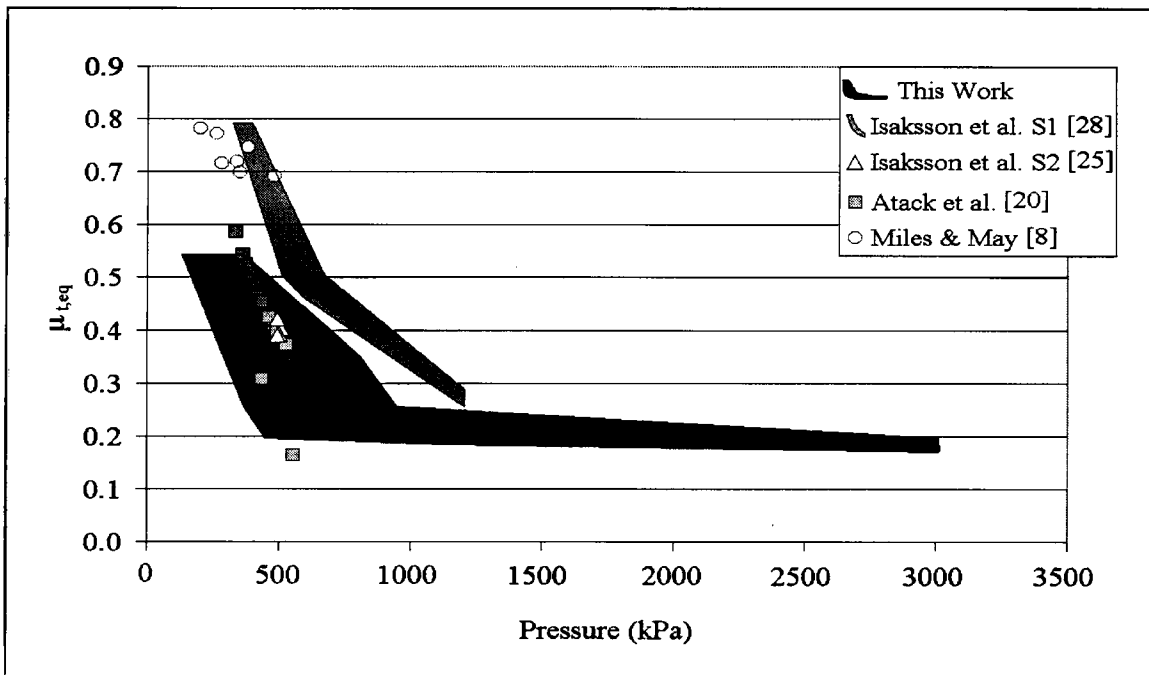


Figure 5.10 Plot of the equivalent tangential coefficient of friction against average mechanical pressure for different refiners.

The dark shaded area represents the data from this work, where the bar coverage fraction α is expected to lie somewhere between 30% and 80%. These values were used to estimate the high and low pressure bounds for this shaded region. For the data of Miles and May $\alpha = 16\%$ is used based on measurements made using that refiner [27]. For all other data, α is estimated at 0.76, based on an average value calculated from data published in [26].

In the case of Isaksson et al., the steam thrust for the data published in [25] was calculated improperly. Corrected data was obtained from the authors [28], but an uncertainty remained, in that pressure measurements were taken at the refiner inlet and also at the inner radius of the refining zone, but nothing is known about the pressure profile in the breaker bar region between those two points. Two possibilities were considered: that the pressure increased linearly with radial position from the value measured at the inlet to the higher value at the end of the breaker bar region, and secondly that the pressure remained constant at the inlet level throughout the breaker bar region. The nature of the true pressure profile is expected to be somewhere in between these two cases. The shaded region encompasses the range of pressure and $\mu_{t,eq}$ calculated assuming the two cases described above.

In all cases, the value of $\mu_{t,eq}$ increases as the pressure decreases. This is not a surprising result, as the calculation of $\mu_{t,eq}$ was performed using F_m in the denominator, and the calculation of the average pressure used F_m in the numerator. The only exception to this is the data from our work, which used the normal force in this same way instead of F_m . This explains the general shape of the trend seen with increasing pressure. It should therefore be re-emphasized that the purpose of plotting this graph was to compare the ranges of our measured values with those from other sources, and not to investigate the relationship between $\mu_{t,eq}$ and mechanical pressure. Such a relationship would have to be examined under conditions of constant throughput and motor load, as these are known to have an effect on the variables under consideration. Furthermore, the calculated values of pressure would be affected by the bar coverage fraction, α , which is unknown here.

The values used are estimates at best, and could also be affected by the mass flow rate of pulp fed through the refiner.

It is interesting to note that for all data sets, except for that of the primary stage refiner of Isaksson et al., the curves for different refiners lie very close to each other, suggesting that they were operating in a range of conditions in which the equivalent tangential coefficient of friction for a given pressure was similar for all of those refiners. The difference between the first and second stage refiners from the data of Isaksson et al. reflects the lower motor load of the latter case, as a lower $\mu_{t,eq}$ (and hence, for a given pressure, a lower shear force) is associated with a decrease in the power consumption. The two points in the data of Atack et al. with the lowest values of $\mu_{t,eq}$ were also taken from a second stage refiner. These two points were refined at a low specific energy (unlike the third point with $\mu_{t,eq}=0.48$, which was refined at a specific energy comparable to the first stage trials). Our trials were performed by refining softwood TMP, effectively making it a second stage process. This would explain why our points lie in the lower region relative to the others.

The fact that the range values of $\mu_{t,eq}$ and pressure measured here are similar to those reported by the other sources, coupled with the fact that the values of $\mu_{t,eq}$ for a given pressure are also similar, indicates that experiments carried out on the laboratory refiner can be useful for investigating the phenomena observed in larger refiners. Further testing is necessary to determine the exact nature of the relationship between the variables in question.

6. CONCLUSIONS

Energy-based methods are commonly used to characterize the action of refiners by quantifying the energy transferred to pulp fibres that pass through the refining zone. However, these methods fail to give insight into the real physical mechanisms acting in the process. In the refining zone, pulp flocs experience cyclically varying loads in directions normal and tangential to the motion of the refiner bars that impact them, and it is these forces that cause the structural changes induced by refining. Therefore, an understanding of these forces is a prerequisite to an understanding of the refining process.

A two-axis force sensor was developed for use in a 12-inch laboratory refiner to measure the normal and shear forces during refiner operation. Although the sensor response presented some limitations when operating the refiner at full speed (2560 rpm), these were not a great detriment when running the refiner at 700 rpm. The magnitudes of the normal and shear forces were seen to rise sharply at the start of bar impacts on pulp flocs, then to fall sharply again to a lower level before tapering off to zero as the bar impacts came to an end. This profile suggests that the normal force is made up of two components, these being the compressive force on the pulp floc (the lower level regime) and the corner force required to plough through the floc (the initial peak in the force profile). The shear force on the refiner bar also contains a corner force component, along with a component due to friction between the pulp and the bar's top face. The corner force appears to be the major component in both cases. Previous work, based on measurements made at low speed in a single-bar refiner, had suggested that the corner force only affected the shear force in refining [24].

While the normal force was seen to increase as the plate clearance decreased, the shear force measured by the sensor reached a maximum at approximately 11 N. If the corner force is the major component of the refining forces, then the forces essentially act at the leading edge of the refiner bars. This suggests an upper limit to the shear force reaction of the pulp per unit bar length of approximately 2.2 kN/m, for the 16% inlet consistency and 700 rpm conditions tested here.

The equivalent tangential coefficient of friction was seen to decrease with decreasing plate gap, due primarily to the leveling off of the shear force while the normal force continued to rise. Adding dilution water also lowered the equivalent tangential coefficient of friction slightly, suggesting that consistency may have an effect, although more testing needs to be done over a greater range of consistency to confirm this.

Further work must be carried out to improve the vibration characteristics of the sensor, as its resonant vibrations dominated the signals collected during refining trials at full speed. The lowest natural frequency of the sensor must be raised and its damping characteristics enhanced in order to implement its use at speeds closer to those used industrially.

BIBLIOGRAPHY

1. A. Banks, "Design and development of a mechanical wood pulp refiner force sensor", Master's Thesis, Queen's University (Jan. 2000).
2. M.I. Stationwala, K.B. Miles, A. Karnis, "The effect of first stage refining conditions on pulp properties and energy consumption", *Journal of Pulp and Paper Science*, 19(1) (1993).
3. R.J. Kerekes, "Characterization of pulp refiners by a C-factor", *Nordic Pulp and Paper Research Journal*, 5(1):3-8 (1990).
4. W. Brecht, "A method for the comparative evaluation of bar equipped beating devices", *Tappi Journal*, 50(8):40A (1967).
5. C.F. Baker, "Specific edge load theory – Applications and limitations" Pira International Refining Conference, Paper 02 (1991).
6. F.P. Meltzer, P. Sepke, "New ways to forecast the technological results of refining", Proceedings of the International Refining Conf. & Exhibition, Atlanta (1995).
7. J. Lumiainen, "Specific surface load theory", Proceedings of the International Refining Conf. & Exhibition, Atlanta (1995).
8. K.B. Miles, W.D. May, "The flow of pulp in chip refiners", *Journal of Pulp and Paper Science*, 16(2):J63-71 (1993).
9. K.B. Miles, W.D. May, "Predicting the performance of chip refiners; A constitutive approach", *Journal of Pulp and Paper Science*, 19(6):J268-274 (1993).
10. K.B. Miles, "A simplified method for calculating the residence time and refining intensity in a chip refiner", *Paperi ja Puu*, 73(9):852-857 (1991).
11. K.B. Miles, A. Karnis, "The response of mechanical and chemical pulps to refining", *Tappi Journal*, 74(1):157-164 (1991).
12. D.H. Page, "The beating of chemical pulps – The action and effects", In F. Bolam, editor, *Fundamentals of Papermaking: Transactions of Fundamental Research Symposium held at Cambridge, volume 1, pages 1-38. Fundamental Research Committee, British Paper and Board Makers' Association (Sept. 1989).*

13. A.A. Khlebnikov, V.F. Pashinski, V.N. Goncharov, E.A. Smirnova, "Analysis of forces involved in the operation of a conical refiner", *Bum Promst.* No.22:129-136 (English Translation) (1969).
14. V.N. Goncharov, E.A. Smirnova, E.V. Shemyakin, "Method for the determination of stresses between refiner blades", *Bum Promst.* No.27:134-138 (1970).
15. V.N. Goncharov, "Force factors in the disc refiner and their effect on the beating process", *Bum Promst.* No.5:12-14 (English Translation) (1971).
16. L. Nordman, J.E. Levlin, T. Makkonen, H. Jokisalo, "Conditions in an LC refiner as observed by physical measurements", *Paperi Ja Puu* 63(4)169-180 (1981).
17. D.M. Martinez, W.J. Batchelor, R.J. Kerekes, D. Ouellet, "Forces on fibres in low consistency refining: Normal force", *Journal of Pulp and Paper Science*, 23(1):J11-18 (1997).
18. W.J. Batchelor, D.M. Martinez, R.J. Kerekes, D. Ouellet, "Forces on fibres in low consistency refining: Shear force", *Journal of Pulp and Paper Science*, 23(1):J40-45 (1997).
19. W.J. Batchelor, D. Ouellet, "Estimating the forces on fibres in refining", 4th Pira International Refining Conference, Fiuggi, Italy, Paper 2 (March, 1997).
20. D. Atack, M.I. Stationwala, "On the measurement of temperature and pressure in the refining zone of an open discharge refiner", *Transactions of the Technical Section of the Canadian Pulp and Paper Association* (3):71-76 (1975).
21. D. Atack, "Towards a theory of refiner mechanical pulping", *Appita Journal*, 34(3):223-227 (1980).
22. D. Atack, M.I. Stationwala, A. Karnis, "What happens in refining" *Pulp and Paper Canada*, 85(12):T303-308 (1984).
23. R. Franzen, R. Sweitzer, "Refining forces in high stock concentration pulping", *Appita Journal* 36(2):116-121 (1982).
24. J. Senger, D. Ouellet, "Factors affecting the shear forces in high-consistency refining", *Proceedings of the International Mechanical Pulping Conference*, Helsinki, Finland, In Press (2001).
25. A.J. Isaksson, A.H. Horch, B. Allison, A. Karlström, L. Nilsson, "Modelling of mechanical thrust in TMP refiners", *Proceedings of the International Mechanical Pulping Conference*, Stockholm, Sweden, pages 87-93 (1997).

26. D. Atack, M.I. Stationwala, A. Karnis, "Distribution And motion of pulp fibres on refiner bar surface" *Journal of Pulp and Paper Science*, 18(4):J131-J137 (1992).
27. W.D. May, M.R. McRae, K.B. Miles, W.E. Lunan, "An approach to the measurement of pulp residence time in a chip refiner", *Journal of Pulp and Paper Science*, 14(3):J47-J53 (1988).
28. A.J. Isaksson, B. Allison, Personal communication of corrected tangential coefficient of friction data of reference [25].

NOMENCLATURE

a	constant equal to 4 for a single disc-refiner and 2 for a double-disc refiner
α	bar coverage fraction
A_m	area of refiner plates experiencing thrust load (m ²)
A_{rz}	total area of refining zone (m ²)
B	refiner bar width (m)
c	pulp consistency (fraction)
C_i	normal force coefficient for piezo element i , (N/V)
CEL	cutting edge length (m/s)
D_i	shear force coefficient for piezo element i , (N/V)
e	specific energy per impact (J/kg impact)
E	specific energy (J/kg)
f	frequency (Hz)
f_{bp}	frequency of bar passing events (Hz)
F	magnitude of resultant force on sensor probe tip (N)
F_m	mechanical thrust (N)
F_N	normal force (N)
F_S	shear force (N)
F_{SL}	shear force per unit length (N/m)
G	groove width (m)
h	constant equal to 1 for a single-disc refiner and 2 for a double-disc refiner
H	refiner bar height (m)

\overline{H}_i	average transfer function for piezo element i (dB)
I	refining intensity (units depend on definition of intensity used)
K_{iN}	sensitivity of piezo element i to a normal force on the sensor probe tip (V/N)
K_{iS}	sensitivity of piezo element i to a shear force on the sensor probe tip (V/N)
$K_{i\theta}$	sensitivity of piezo element i to a force acting at angle θ to the y-axis (V/N)
L_{bc}	total length of bar edges crossing
L_i	length of refiner bar within radial increment i (m)
λ	fraction of refining zone area constituted by bar surfaces
\dot{m}_f	oven-dry fibre mass flow rate through refiner (kg/s)
μ_r	radial coefficient of friction
μ_t	tangential coefficient of friction
$\mu_{t,eq}$	equivalent tangential coefficient of friction
N_{av}	average number of bars per unit length of arc on refiner plate (m^{-1})
n	number of impacts
n_{imp}	number of impacts experienced by pulp in one pass through the refining zone
n_{ri}	number of bars on rotor plate
n_{si}	number of bars on stator plate
θ	angle between the line of action of impact force and the y-axis ($^\circ$)
p_{ave}	average mechanical pressure on refiner plates (Pa)
P	net refining power (W)
r_1	inner radius of the refining zone (m)
r_2	outer radius of the refining zone (m)
r_s	radial position of sensor on stator plate (m)

R^2	regression correlation coefficient
S	steam flow term (s^{-1})
SEL	specific edge load (J/m)
τ	residence time (s)
v	radial velocity of pulp in the refining zone (m/s)
V_h	peak voltage of hammer signal (V)
V_i	peak voltage of signal from piezo element i (V)
ω	refiner rotational speed (rad/s)
Ω	refiner rotational speed (rpm)

APPENDIX A

SPECIFICATIONS OF D2B502 REFINER PLATES

Rotor and stator plates are identical.

Inner radius of refining zone, $r_1 = 12.25$ cm

Outer radius of refining zone, $r_2 = 15.25$ cm

Bar width, $B = 2.8$ mm

Bar Height, $H = 3.7$ mm

Groove Width, $G = 2.6$ mm

Number of bars per segment at radial position of sensor (14.6 cm) = 48

Number of segments on rotor = 3

Number of segments on stator = 3

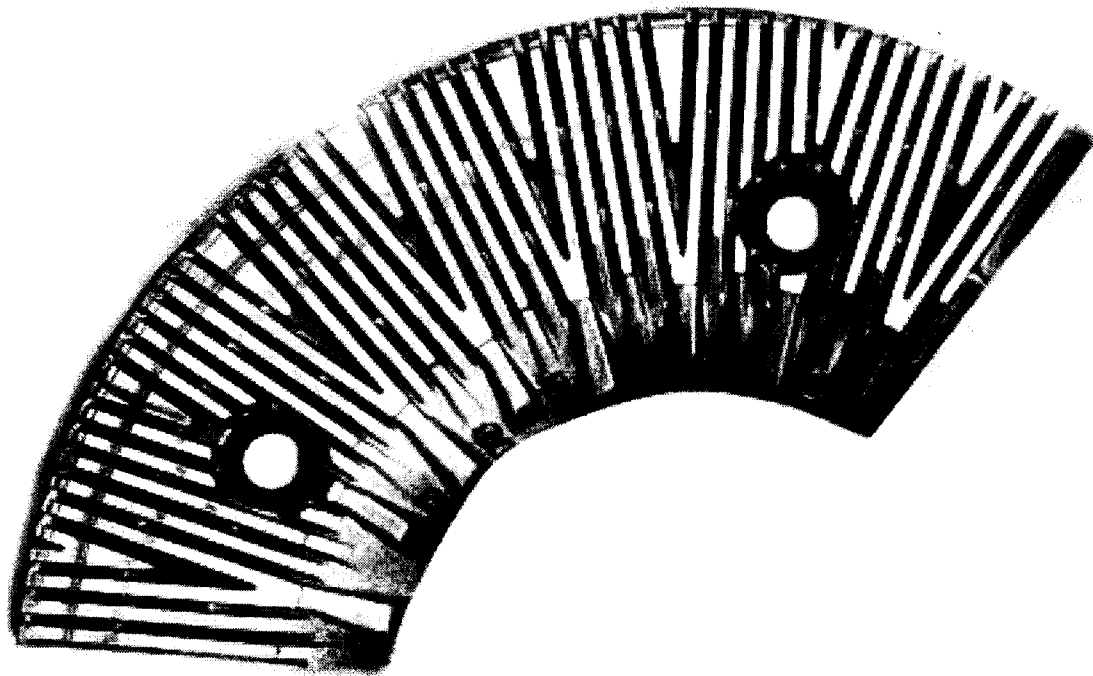


Figure A1. A segment of the rotor plate

APPENDIX B

PROPERTIES OF PIEZO CERAMIC ELEMENTS

<i>Property</i>		<i>Piezo Elements in Original Design</i>	<i>Piezo Elements in Modified Design</i>	<i>Units</i>
Material		Lead Zirconate Titanate	Lead Zirconate Titanate	
Dimensions		1 mm x 1 mm x 7 mm	1 mm x 2 mm x 7 mm	
Density		7.65	7.7	g/cm ³
Curie Temperature	T _c	360	350	°C
<i>Electrical</i>				
Dielectric Constant	K ₃₃ T	1750	1800	
Dissipation Factor		1.6	1.5	%
<i>Piezoelectric</i>				
Coupling Factor	k _p	0.62	0.6	---
	k ₃₁	0.37	0.34	---
	k ₃₃	0.72	0.69	---
Charge Constant	d ₃₁	-160	-175	10 ⁻¹² C/N
	d ₃₃	365	400	10 ⁻¹² C/N
Voltage Constant	g ₃₁	-11.5	-11	10 ⁻³ Vm/N
	g ₃₃	25	25.1	10 ⁻³ Vm/N
Frequency Constants	N _p	2050	2057	Hz.m
	N ₁	1400	1359	Hz.m
	N ₃	1800	1857	Hz.m
<i>Elastic Modulus</i>				
Compliance	S ₁₁ ^E	15.5	15.4	10 ⁻¹² m ² /N
	S ₃₃ ^E	19	18.4	10 ⁻¹² m ² /N

APPENDIX C

CALIBRATION PROCEDURE

This section provides details of the calibration procedures employed with the sensors used in this project. The section is split into two parts, the first explaining the original calibration method, which involved the use of the mounting jig, and the second explaining the revised calibration method, which involved impacting the sensor in the plate only.

C1. ORIGINAL CALIBRATION METHOD

This method consisted of impacting the sensor (mounted in the jig) with the force-measuring hammer along the x- and y-directions, as shown in Figure 3.3. This leads to the determination of K-values (the sensor response in V/N) for both normal and shear impacts in the jig. The sensor is then installed in the refiner plate, and impacted normally (along the y-direction) thus determining the actual sensitivity to normal impacts (as this is generally different from the K-value observed with the sensor in the jig). The K-value for shear impacts in the plate is then calculated by appropriate scaling according to Equation 3.4. Equations for calculating the forces from the piezo signals are derived from these K-values. This process is shown in detail below for the sensor used for the data in chapter 3.

The results of impacting the sensor in the jig in the normal and shear directions are shown in Figures C1 and C2, while Figure C3 shows the results of impacting the sensor in the normal direction while mounted in the plate.

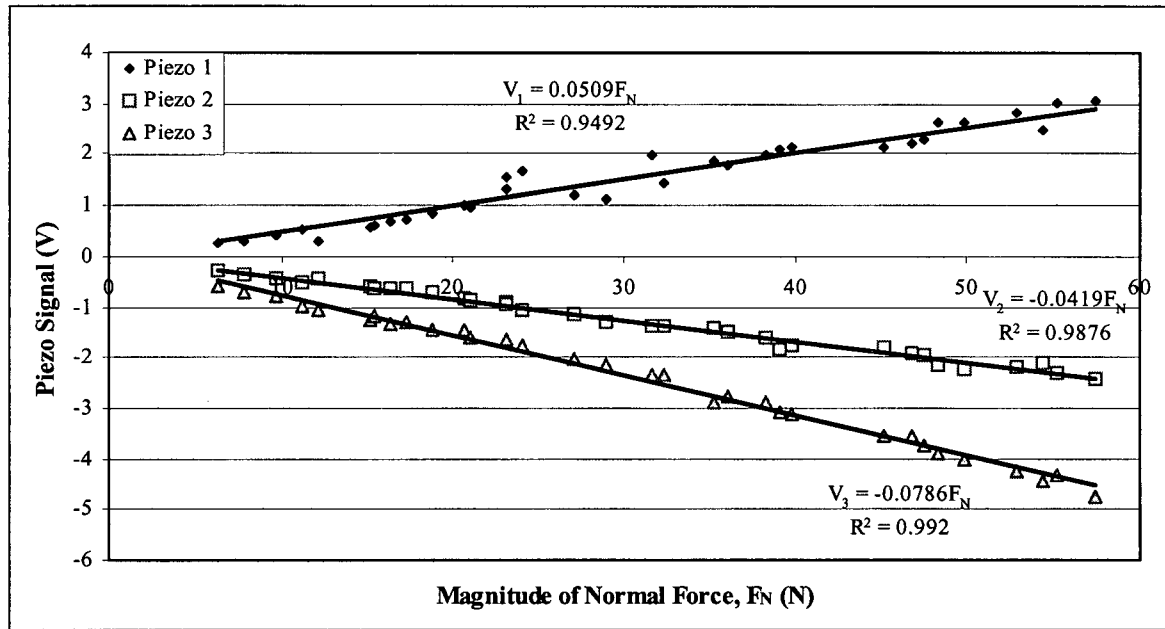


Figure C1. Piezo voltage vs normal impact force (impacts applied in mounting jig).

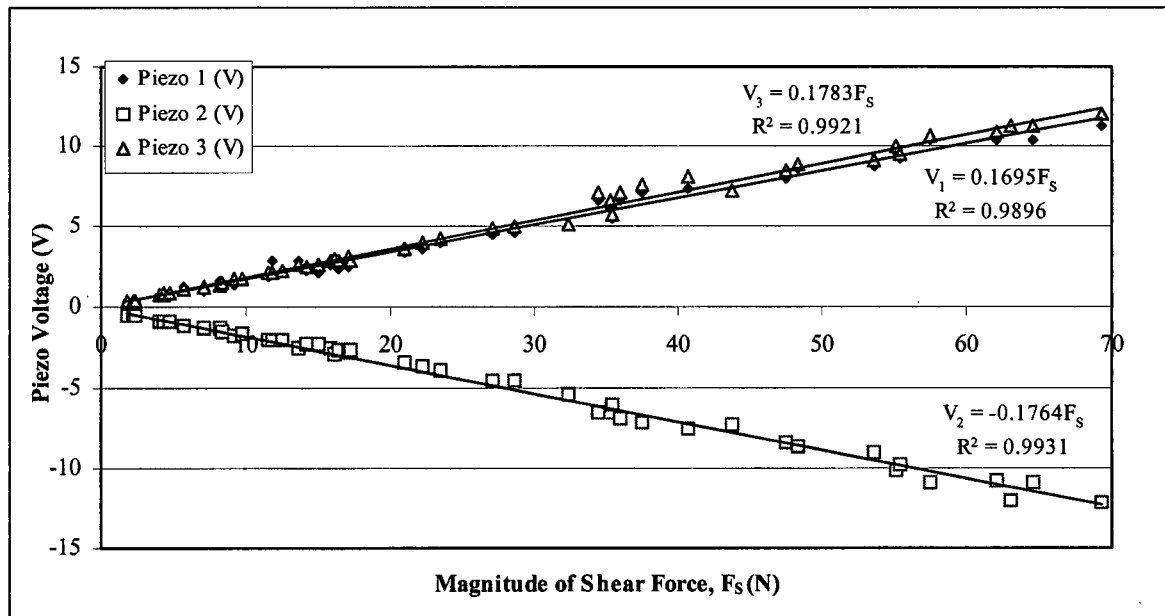


Figure C2. Piezo voltage vs shear impact force (impacts applied in mounting jig).

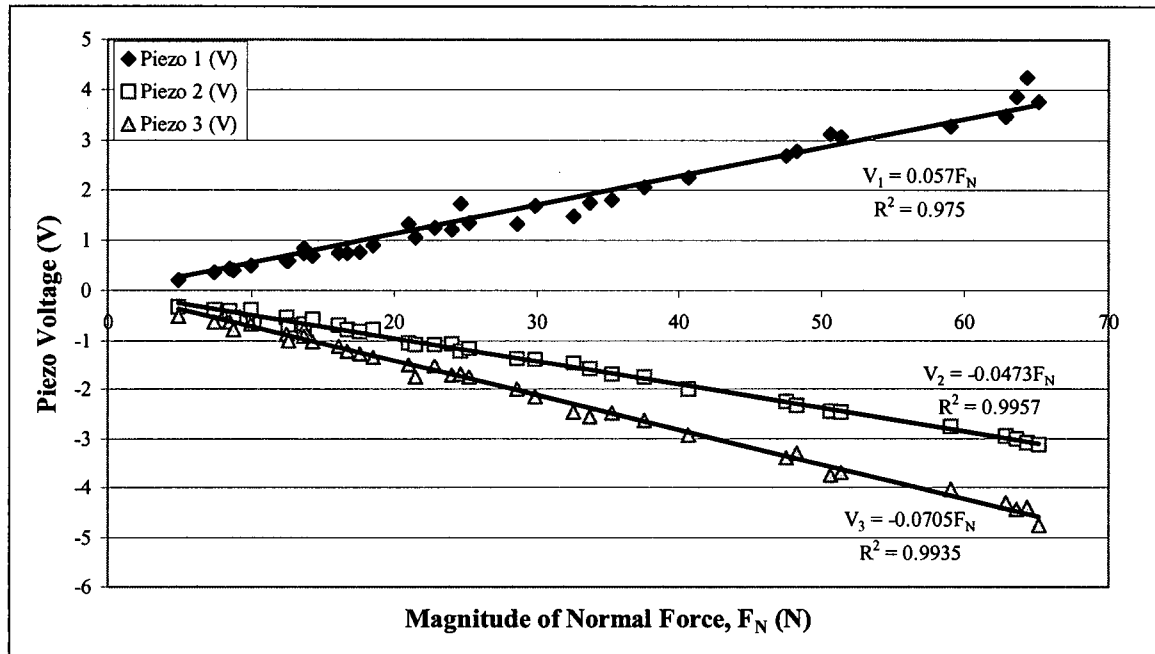


Figure C3. Piezo voltage vs normal force (impacts applied with sensor mounted in plate).

The results of linear regressions are shown on the graphs, and the K-values are determined from the slopes of these graphs. The summarized results of the above are:

$$\begin{array}{lll}
 K_{1N}(jig) = 0.0509 \text{ V/N} & K_{1S}(jig) = 0.170 \text{ V/N} & K_{1N}(plate) = 0.0570 \text{ V/N} \\
 K_{2N}(jig) = -0.0419 \text{ V/N} & K_{2S}(jig) = -0.176 \text{ V/N} & K_{2N}(plate) = -0.0473 \text{ V/N} \\
 K_{3N}(jig) = -0.0786 \text{ V/N} & K_{3S}(jig) = 0.178 \text{ V/N} & K_{3N}(plate) = -0.0705 \text{ V/N}
 \end{array}$$

K-values for shear impacts in the plate are now calculated by applying Equation C1 (same as Equation 3.4) below:

$$K_{is} = \frac{K_{iN}(plate)}{K_{iN}(jig)} \cdot K_{is}(jig) \quad (C1)$$

The use of this equation marks a slight departure from the calibration method used in [1], in which the discrepancy between the K-values from the jig and plate mounting conditions was not addressed.

Equation 3.4 yields:

$$K_{1S}(\text{plate}) = 0.190 \text{ V/N}$$

$$K_{2S}(\text{plate}) = -0.199 \text{ V/N}$$

$$K_{3S}(\text{plate}) = 0.160 \text{ V/N}$$

Now we can state that:

$$\begin{pmatrix} V_i \\ V_j \end{pmatrix} = \begin{pmatrix} K_{iN} & K_{iS} \\ K_{jN} & K_{jS} \end{pmatrix} \begin{pmatrix} F_N \\ F_S \end{pmatrix} \quad (\text{C2a})$$

Rearranging the above equation then gives:

$$\begin{pmatrix} F_N \\ F_S \end{pmatrix} = \begin{pmatrix} K_{iN} & K_{iS} \\ K_{jN} & K_{jS} \end{pmatrix}^{-1} \begin{pmatrix} V_i \\ V_j \end{pmatrix} \quad (\text{C2b})$$

This equation thus gives the normal and shear forces calculated using any desired pair of piezo elements. As explained in [1] and chapter 3 of this work, pairs of piezo elements must be chosen such that they are on opposite sides of the probe, and so only piezo pairs 1-3 and 2-3 are used for force calculations.

$$\begin{pmatrix} F_{N13} \\ F_{S13} \end{pmatrix} = \begin{pmatrix} 6.96 & -8.69 \\ 3.28 & 2.58 \end{pmatrix} \begin{pmatrix} V_1 \\ V_3 \end{pmatrix} \quad (\text{C3a})$$

$$\begin{pmatrix} F_{N23} \\ F_{S23} \end{pmatrix} = \begin{pmatrix} -7.39 & -9.31 \\ -3.47 & 2.29 \end{pmatrix} \begin{pmatrix} V_2 \\ V_3 \end{pmatrix} \quad (\text{C3b})$$

These equations were used to back-calculate the forces from the piezo responses. All the data are shown in the following tables, with the calculated forces and their respective errors shown in the four columns on the right.

Table C1. Data for normal impacts applied with sensor in mounting jig.

$F_N(\text{measured})$ (N)	V_1 (V)	V_2 (V)	V_3 (V)	F_{N13} (N)	$Error(13)$ (%)	F_{N23} (N)	$Error(23)$ (%)
6.26	0.28	-0.26	-0.60	7.12	13.66	7.52	20.14
7.79	0.32	-0.34	-0.72	8.53	9.44	9.27	18.87
9.63	0.43	-0.42	-0.79	9.83	2.10	10.42	8.22
11.16	0.54	-0.50	-0.97	12.22	9.50	12.75	14.18
12.08	0.32	-0.42	-1.07	11.50	4.80	13.04	7.94
15.15	0.56	-0.58	-1.26	14.80	2.27	15.94	5.25
15.45	0.62	-0.62	-1.16	14.41	6.78	15.42	0.25
16.37	0.68	-0.64	-1.32	16.18	1.16	16.99	3.75
17.29	0.71	-0.62	-1.29	16.14	6.68	16.58	4.12
18.82	0.85	-0.72	-1.44	18.47	1.86	18.73	0.51
20.66	1.01	-0.83	-1.44	19.56	5.33	19.54	5.45
20.97	0.95	-0.86	-1.60	20.48	2.31	21.22	1.21
23.11	1.32	-0.92	-1.69	23.90	3.38	22.56	2.41
23.11	1.53	-0.94	-1.66	25.08	8.53	22.43	2.97
24.03	1.65	-1.06	-1.76	26.73	11.25	24.18	0.60
27.10	1.21	-1.12	-2.04	26.12	3.61	27.26	0.59
28.93	1.14	-1.28	-2.13	26.44	8.60	29.29	1.21
31.69	1.98	-1.36	-2.35	34.19	7.89	31.90	0.65
32.30	1.43	-1.38	-2.35	30.37	5.98	32.06	0.74
35.26	1.87	-1.41	-2.88	38.03	7.85	37.23	5.58
36.03	1.78	-1.48	-2.76	36.29	0.74	36.60	1.60
38.33	1.96	-1.61	-2.88	38.69	0.94	38.69	0.95
39.09	2.09	-1.83	-3.07	41.19	5.35	42.05	7.57
39.86	2.12	-1.76	-3.13	41.95	5.24	42.17	5.81
45.22	2.15	-1.80	-3.57	45.97	1.65	46.48	2.78
46.75	2.21	-1.92	-3.57	46.40	0.75	47.40	1.39
47.52	2.28	-1.95	-3.76	48.46	1.99	49.38	3.91
48.28	2.62	-2.16	-3.88	51.94	7.58	52.08	7.86
49.82	2.62	-2.23	-4.01	53.03	6.45	53.78	7.97
52.88	2.84	-2.19	-4.26	56.72	7.27	55.79	5.50
54.41	2.49	-2.11	-4.44	55.96	2.85	56.98	4.72
55.18	3.03	-2.31	-4.32	58.57	6.15	57.25	3.75
57.48	3.06	-2.42	-4.76	62.59	8.90	62.15	8.14

Mean = 5.42

Mean = 5.05

Table C2. Data for normal impacts applied with sensor in mounting jig.

$F_s(\text{measured})$ (N)	V_1 (V)	V_2 (V)	V_3 (V)	F_{S13} (N)	$Error(13)$ (%)	F_{S23} (N)	$Error(23)$ (%)
1.8689	0.3688	-0.4512	0.37	2.16	15.80	2.41	29.11
2.1752	0.4	-0.4512	0.4013	2.35	7.91	2.48	14.23
2.3284	0.4313	-0.4825	0.4325	2.53	8.68	2.66	14.44
4.0135	0.7125	-0.8263	0.7763	4.34	8.13	4.64	15.73
4.3199	0.6813	-0.8263	0.7763	4.24	1.91	4.64	7.53
4.3199	0.7438	-0.8575	0.8388	4.60	6.57	4.90	13.34
4.7794	0.9375	-0.92	0.8388	5.24	9.62	5.11	6.99
5.6985	1.1938	-1.1075	1.0888	6.72	18.01	6.34	11.19
7.0772	0.9812	-1.2637	1.3075	6.59	6.86	7.38	4.27
8.1495	1.6062	-1.2637	1.37	8.80	8.02	7.52	7.70
8.3027	1.4	-1.4825	1.5575	8.61	3.71	8.71	4.92
9.2218	1.4187	-1.7012	1.745	9.16	0.72	9.90	7.35
9.6814	1.5875	-1.6387	1.745	9.71	0.29	9.68	0.01
11.5196	1.9	-1.9512	2.0888	11.62	0.88	11.55	0.30
11.826	2.9312	-2.0137	2.1513	15.16	28.23	11.91	0.74
12.4387	2.0875	-2.0137	2.2138	12.56	0.96	12.06	3.07
13.6642	2.8687	-2.4512	2.5888	16.09	17.74	14.43	5.63
14.1238	2.275	-2.295	2.5263	13.98	1.02	13.75	2.65
15.0429	2.1312	-2.295	2.62	13.75	8.60	13.96	7.18
15.8088	2.6187	-2.5137	2.8388	15.91	0.66	15.22	3.70
16.0662	2.7125	-2.92	2.995	16.62	3.47	16.99	5.76
16.4216	2.3187	-2.6075	2.87	15.01	8.60	15.62	4.88
17.0343	2.4687	-2.7637	3.0888	16.07	5.68	16.66	2.18
17.1875	2.9437	-2.5762	2.9013	17.14	0.27	15.58	9.33
20.9681	3.4	-3.3575	3.6825	20.65	1.50	20.08	4.22
22.1936	3.5875	-3.67	3.995	22.07	0.54	21.88	1.40
23.4191	3.9625	-3.92	4.3075	24.11	2.95	23.47	0.20
27.0956	4.525	-4.545	4.87	27.41	1.15	26.92	0.64
28.6275	4.5875	-4.545	4.995	27.93	2.42	27.21	4.95
32.3039	4.9625	-5.3325	5.1825	29.65	8.22	30.37	5.98
34.4975	6.6188	-6.4625	7.1312	40.11	16.26	38.76	12.34
35.2635	6.15	-6.4938	6.6625	37.36	5.95	37.79	7.17
35.3676	5.4625	-5.995	5.745	32.74	7.43	33.96	3.98
36.0294	6.6188	-6.9063	7.1312	40.11	11.32	40.30	11.84
37.5613	7.0875	-7.1313	7.6	42.86	14.09	42.15	12.22
40.625	7.4	-7.4438	8.0687	45.09	10.99	44.31	9.06
43.6887	7.0875	-7.275	7.2875	42.05	3.75	41.93	4.02
47.5184	8.025	-8.3688	8.5375	48.35	1.75	48.59	2.26
48.2843	8.65	-8.6813	8.85	51.21	6.05	50.39	4.36
53.6456	8.8063	-8.9938	9.1625	52.52	2.09	52.19	2.71
55.1775	9.5875	-10.0875	9.9437	57.10	3.49	57.77	4.71
55.4534	9.275	-9.775	9.475	54.87	1.06	55.62	0.30
57.4755	10.3687	-10.8688	10.5688	61.28	6.61	61.92	7.73
62.0711	10.3687	-10.7125	10.9	62.13	0.10	62.13	0.10
63.1127	11.15	-11.9625	11.2625	65.63	3.99	67.30	6.64
64.6446	10.3687	-10.8688	11.2125	62.94	2.64	63.39	1.94
69.2402	11.3062	-12.1188	11.9938	68.03	1.75	69.52	0.40
69.2402	11.3062	-12.1188	11.9938	68.03	1.75	69.52	0.40

Mean =6.05

Mean =6.08

Table C3. Data for normal impacts applied with sensor mounted in plate.

$F_N(\text{measured})$ (N)	V_1 (V)	V_2 (V)	V_3 (V)	F_{N13} (N)	<i>Error</i> (%)	F_{N23} (N)	<i>Error</i> (%)
4.93	0.22	-0.31	-0.50	5.87	18.96	6.96	41.19
7.38	0.38	-0.37	-0.63	8.04	8.91	8.59	16.29
8.46	0.44	-0.39	-0.63	8.48	0.24	8.74	3.32
8.76	0.41	-0.54	-0.78	9.62	9.76	11.23	28.13
9.94	0.51	-0.37	-0.66	9.27	6.73	8.88	10.68
12.44	0.59	-0.54	-0.88	11.74	5.64	12.11	2.60
12.59	0.59	-0.67	-1.00	12.82	1.83	14.28	13.40
13.66	0.84	-0.78	-0.78	12.66	7.33	13.04	4.58
13.66	0.75	-0.66	-0.91	13.10	4.16	13.31	2.61
14.28	0.69	-0.58	-1.03	13.75	3.71	13.85	2.99
16.12	0.75	-0.68	-1.13	15.00	6.94	15.52	3.71
16.68	0.75	-0.78	-1.22	15.81	5.20	17.11	2.59
17.60	0.78	-0.82	-1.28	16.56	5.88	17.99	2.22
18.52	0.91	-0.78	-1.34	17.99	2.87	18.27	1.31
20.97	1.33	-1.05	-1.50	22.29	6.31	21.69	3.43
21.48	1.06	-1.09	-1.75	22.60	5.24	24.31	13.21
22.81	1.25	-1.09	-1.53	22.01	3.51	22.33	2.10
24.03	1.22	-1.07	-1.72	23.42	2.55	23.87	0.66
24.64	1.72	-1.22	-1.69	26.69	8.30	24.75	0.44
25.26	1.34	-1.15	-1.75	24.56	2.76	24.81	1.76
28.63	1.32	-1.37	-2.00	26.57	7.20	28.71	0.30
29.85	1.69	-1.39	-2.16	30.48	2.11	30.33	1.59
32.61	1.48	-1.48	-2.47	31.75	2.62	33.88	3.91
33.73	1.75	-1.57	-2.56	34.45	2.12	35.48	5.19
35.26	1.81	-1.70	-2.48	34.12	3.23	35.57	0.86
37.56	2.06	-1.75	-2.63	37.17	1.05	37.39	0.46
40.63	2.25	-2.00	-2.91	40.97	0.85	41.90	3.13
47.52	2.69	-2.25	-3.38	48.03	1.08	48.05	1.12
48.28	2.79	-2.33	-3.28	47.86	0.88	47.67	1.27
50.58	3.12	-2.45	-3.75	54.30	7.36	53.02	4.82
51.35	3.08	-2.47	-3.69	53.45	4.09	52.56	2.36
59.01	3.29	-2.75	-4.03	57.86	1.95	57.80	2.04
62.84	3.48	-2.93	-4.30	61.51	2.11	61.66	1.88
62.84	3.48	-2.94	-4.30	61.59	1.99	61.73	1.77
63.60	3.87	-2.99	-4.44	65.50	2.98	63.41	0.30
64.37	4.26	-3.08	-4.40	67.89	5.46	63.69	1.05
65.13	3.78	-3.12	-4.75	67.55	3.71	67.25	3.25

Mean = 3.93

Mean = 3.14

The mean percentage errors in all cases are quite low, and the graph of Figure C4 shows a good agreement between the force measured by the impact hammer, and that calculated using the magnitudes of the piezo signals. These two facts suggest that the calibration procedure here is reliable.

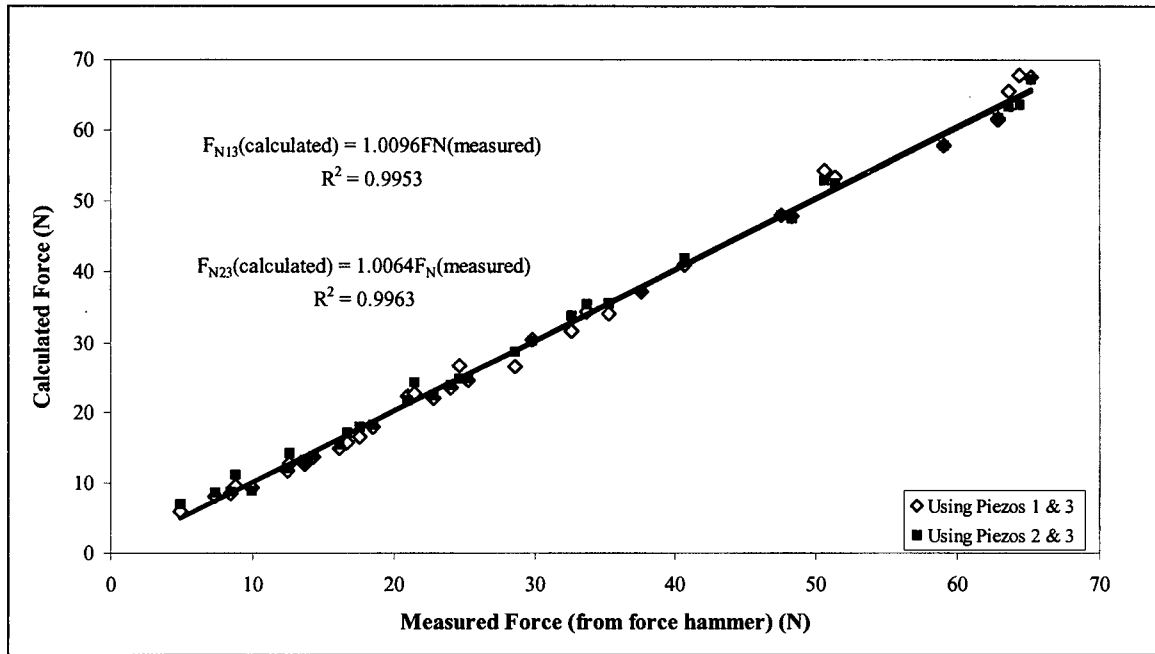


Figure C4. Calculated force vs. Measured force for normal impacts with sensor mounted in plate.

C2. NEW CALIBRATION METHOD

As explained in section 3.4, the original calibration was modified, as it did not account for the change in the sensor's response to impacts in the shear direction when it was transferred from the jig to the plate. It was seen, time and time again, that the response of the sensor was extremely sensitive to the mounting conditions. This became an even more significant issue when the use of shims was employed to stiffen the sensor housing, as there was no way to ensure that the preload on the piezo ceramic elements in the jig was the same as that in the plate.

It was therefore decided that calibration had to be performed with the sensor installed in the plate, to ensure that mounting conditions did not change between the time of calibration and refining trials. This section provides the impact data and details of the calibration for the sensor used for the data in section 4.2, where the calibration method is outlined.

The sensor was impacted at various angles (as described in section 4.2), and K-values ($K_{i\theta}$) were determined for different angles, θ , to the normal direction (as shown in Figure 4.6). K_{iN} was determined as before, by impacting the sensor in the normal direction. K_{iS} was then determined using:

$$K_{iS} = \frac{K_{i\theta} - K_{iN} \cos\theta}{\sin\theta} \quad (C4)$$

This was done for all angles, θ , at which the sensor was impacted, and the mean value of K_{iS} found in this way was taken as the true K_{iS} .

Table C4 shows all the impact data (magnitude of impact force F from force hammer, and piezo voltages V_1 , V_3 and V_4), along with the true normal and shear forces associated with each impact ($F \cos\theta$ and $F \sin\theta$, respectively), and the back-calculated normal and shear components from the piezo signals. Figures C5 through C9 are graphs of the impact data, with linear regressions from which the K-values were determined. These K-values are summarized in Table C5, which is identical to Table 4.1.

Table C4. Data for impacts administered at different angles.

θ (°)	F (N)	V_1 (V)	V_2 (V)	V_3 (V)	$F \cos\theta$ (N)	$F \sin\theta$ (N)	F_{N13} (N)	F_{S13} (N)	F_{N14} (N)	F_{S14} (N)
0	9.19	0.41	-0.56	0.47	9.19	0.00	8.73	0.31	9.47	-0.04
0	11.80	0.52	-0.77	0.58	11.80	0.00	11.42	0.22	11.97	-0.03
0	15.01	0.67	-0.94	0.72	15.01	0.00	14.48	0.48	15.19	0.16
0	15.47	0.67	-1.02	0.76	15.47	0.00	15.01	0.23	15.62	-0.05
0	17.16	0.75	-1.09	0.83	17.16	0.00	16.48	0.39	17.16	0.08
0	17.46	0.77	-1.14	0.83	17.46	0.00	16.99	0.32	17.35	0.16
0	22.06	0.97	-1.45	1.04	22.06	0.00	21.56	0.37	21.87	0.25
0	22.37	0.97	-1.53	1.08	22.37	0.00	22.09	0.12	22.30	0.04
0	22.98	1.02	-1.63	1.13	22.98	0.00	23.29	0.07	23.31	0.07
0	24.51	1.06	-1.67	1.19	24.51	0.00	24.18	0.16	24.47	0.04
0	25.12	1.09	-1.73	1.21	25.12	0.00	24.98	0.12	25.14	0.07
0	26.96	1.13	-1.94	1.32	26.96	0.00	26.73	-0.36	26.54	-0.26
0	28.80	1.23	-2.06	1.41	28.80	0.00	28.90	-0.20	28.75	-0.11
0	29.41	1.30	-2.09	1.44	29.41	0.00	29.87	0.03	29.80	0.08
0	31.25	1.33	-2.22	1.58	31.25	0.00	31.10	-0.21	31.50	-0.38
0	33.70	1.47	-2.56	1.58	33.70	0.00	35.12	-0.58	33.21	0.35
0	35.54	1.52	-2.53	1.74	35.54	0.00	35.48	-0.24	35.39	-0.17
10	6.59	0.39	-0.25	0.17	6.49	1.14	6.46	1.24	6.45	1.25
10	7.20	0.43	-0.29	0.19	7.09	1.25	7.14	1.26	6.98	1.34
10	9.65	0.56	-0.35	0.23	9.50	1.68	9.11	1.76	9.04	1.80
10	10.72	0.62	-0.39	0.27	10.56	1.86	10.16	1.94	10.10	1.98
10	11.64	0.66	-0.41	0.28	11.47	2.02	10.74	2.08	10.70	2.10
10	12.56	0.73	-0.43	0.28	12.37	2.18	11.74	2.42	11.61	2.49
10	14.09	0.80	-0.59	0.40	13.88	2.45	13.63	2.25	13.56	2.29
10	15.32	0.88	-0.56	0.36	15.09	2.66	14.37	2.75	14.12	2.88
10	20.53	1.19	-0.75	0.50	20.22	3.56	19.46	3.75	19.28	3.85
10	20.53	1.16	-0.88	0.63	20.22	3.56	19.93	3.19	20.13	3.11
10	22.06	1.25	-0.91	0.64	21.72	3.83	21.28	3.57	21.41	3.52
10	24.20	1.39	-0.98	0.69	23.84	4.20	23.51	4.05	23.58	4.03
10	25.74	1.47	-1.05	0.73	25.34	4.47	24.88	4.25	24.99	4.22
10	27.57	1.63	-0.98	0.69	27.15	4.79	26.35	5.26	26.42	5.25
10	27.57	1.53	-1.34	0.78	27.15	4.79	27.64	3.63	26.20	4.33
10	27.88	1.64	-1.17	0.83	27.46	4.84	27.81	4.74	27.98	4.68
10	29.87	1.69	-1.47	0.86	29.42	5.19	30.38	4.04	28.86	4.78
10	32.78	1.86	-1.38	0.97	32.28	5.69	31.83	5.23	32.01	5.17
10	32.78	1.83	-1.48	1.05	32.28	5.69	32.19	4.72	32.40	4.64
20	4.29	0.30	0.07	-0.03	4.03	1.47	3.19	1.79	3.36	1.71
20	4.37	0.29	0.06	-0.03	4.10	1.49	3.13	1.71	3.24	1.66
20	5.13	0.32	0.08	-0.04	4.82	1.76	3.28	1.90	3.47	1.81
20	5.36	0.37	0.09	-0.04	5.04	1.83	3.89	2.21	4.14	2.09
20	9.50	0.65	0.14	-0.08	8.92	3.25	6.95	3.83	7.17	3.74
20	10.11	0.68	0.16	-0.08	9.50	3.46	7.18	4.02	7.48	3.89
20	11.18	0.73	0.19	-0.10	10.51	3.82	7.53	4.38	7.87	4.23
20	13.17	0.89	0.22	-0.11	12.38	4.51	9.33	5.33	9.73	5.15
20	14.71	1.03	0.24	-0.14	13.82	5.03	10.90	6.09	11.15	5.98
20	17.46	1.17	0.31	-0.16	16.41	5.97	12.05	7.04	12.62	6.78
20	19.00	1.29	0.34	-0.17	17.85	6.50	13.32	7.75	13.94	7.47
20	23.59	1.62	0.41	-0.21	22.17	8.07	16.82	9.66	17.48	9.36
20	23.59	1.68	0.43	-0.22	22.17	8.07	17.51	10.08	18.26	9.74
20	24.51	1.79	0.40	-0.26	23.03	8.38	18.95	10.52	19.12	10.46
20	25.74	1.86	0.45	-0.24	24.18	8.80	19.44	11.04	20.15	10.72
20	28.34	2.06	0.38	-0.27	26.63	9.69	22.43	11.87	22.40	11.91
20	29.41	2.10	0.55	-0.29	27.64	10.06	21.72	12.59	22.63	12.18
30	5.90	0.49	0.11	-0.08	5.11	2.95	5.17	2.87	5.08	2.91
30	6.28	0.54	0.13	-0.09	5.44	3.14	5.72	3.22	5.73	3.22
30	7.81	0.65	0.14	-0.11	6.77	3.91	6.91	3.82	6.78	3.89

θ ($^{\circ}$)	F (N)	V_1 (V)	V_2 (V)	V_3 (V)	$F \cos\theta$ (N)	$F \sin\theta$ (N)	F_{N13} (N)	F_{S13} (N)	F_{N14} (N)	F_{S14} (N)
30	7.97	0.67	0.15	-0.12	6.90	3.98	7.07	3.95	6.94	4.01
30	8.73	0.73	0.16	-0.12	7.56	4.37	7.71	4.26	7.59	4.32
30	9.11	0.78	0.20	-0.13	7.89	4.56	8.06	4.63	8.08	4.63
30	11.80	1.00	0.24	-0.21	10.22	5.90	10.51	5.93	10.04	6.16
30	15.78	1.33	0.36	-0.29	13.66	7.89	13.65	8.02	13.22	8.23
30	15.78	1.34	0.38	-0.30	13.66	7.89	13.71	8.16	13.35	8.34
30	16.54	1.45	0.33	-0.27	14.33	8.27	15.37	8.57	14.98	8.77
30	17.46	1.52	0.40	-0.33	15.12	8.73	15.67	9.11	15.19	9.35
30	17.62	1.55	0.39	-0.33	15.26	8.81	16.13	9.23	15.57	9.51
30	18.84	1.66	0.47	-0.36	16.32	9.42	16.91	10.06	16.53	10.25
30	19.30	1.67	0.46	-0.36	16.72	9.65	17.14	10.12	16.72	10.33
30	20.83	1.80	0.63	-0.42	18.04	10.42	17.55	11.28	17.68	11.24
30	22.37	1.91	0.64	-0.43	19.37	11.18	18.77	11.90	18.95	11.83
30	24.51	2.09	0.77	-0.49	21.23	12.25	20.20	13.27	20.61	13.09
30	25.43	2.22	0.69	-0.48	22.02	12.71	22.24	13.66	22.18	13.71
30	25.74	2.19	0.83	-0.52	22.29	12.87	20.91	13.95	21.44	13.72
30	31.56	2.78	0.95	-0.61	27.33	15.78	27.27	17.42	27.72	17.23
40	6.20	0.52	0.20	-0.14	4.75	3.99	4.92	3.31	4.93	3.31
40	6.28	0.51	0.19	-0.14	4.81	4.04	4.95	3.24	4.86	3.29
40	7.35	0.61	0.27	-0.17	5.63	4.73	5.56	3.99	5.71	3.93
40	7.51	0.61	0.29	-0.17	5.75	4.82	5.51	4.08	5.78	3.95
40	7.51	0.65	0.26	-0.18	5.75	4.82	6.11	4.16	6.13	4.16
40	10.26	0.89	0.34	-0.28	7.86	6.60	8.41	5.68	7.99	5.89
40	14.09	1.24	0.50	-0.38	10.80	9.06	11.63	7.99	11.33	8.14
40	17.00	1.55	0.83	-0.52	13.03	10.93	13.13	10.65	13.71	10.39
40	17.16	1.58	0.83	-0.50	13.14	11.03	13.47	10.79	14.20	10.46
40	19.61	1.80	0.95	-0.59	15.02	12.60	15.39	12.34	16.01	12.06
40	22.98	2.08	1.01	-0.63	17.60	14.77	18.40	13.98	19.11	13.66
40	23.90	2.19	1.26	-0.77	18.31	15.36	18.08	15.36	19.10	14.89
40	24.51	2.22	1.32	-0.80	18.78	15.75	18.02	15.69	19.14	15.18
40	25.74	2.39	1.39	-0.83	19.71	16.54	19.58	16.79	20.88	16.20
40	25.74	2.33	1.34	-0.83	19.71	16.54	19.22	16.35	20.19	15.91
40	30.94	3.04	1.45	-0.91	23.70	19.89	27.02	20.33	27.95	19.91
40	32.48	3.04	1.64	-1.00	24.88	20.87	25.74	20.93	27.03	20.34
40	34.62	3.32	1.78	-1.09	26.52	22.25	28.18	22.84	29.53	22.23
40	36.00	3.54	2.00	-1.20	27.58	23.14	29.46	24.69	31.18	23.90
40	39.06	3.94	2.16	-1.33	29.92	25.11	33.11	27.25	34.73	26.52

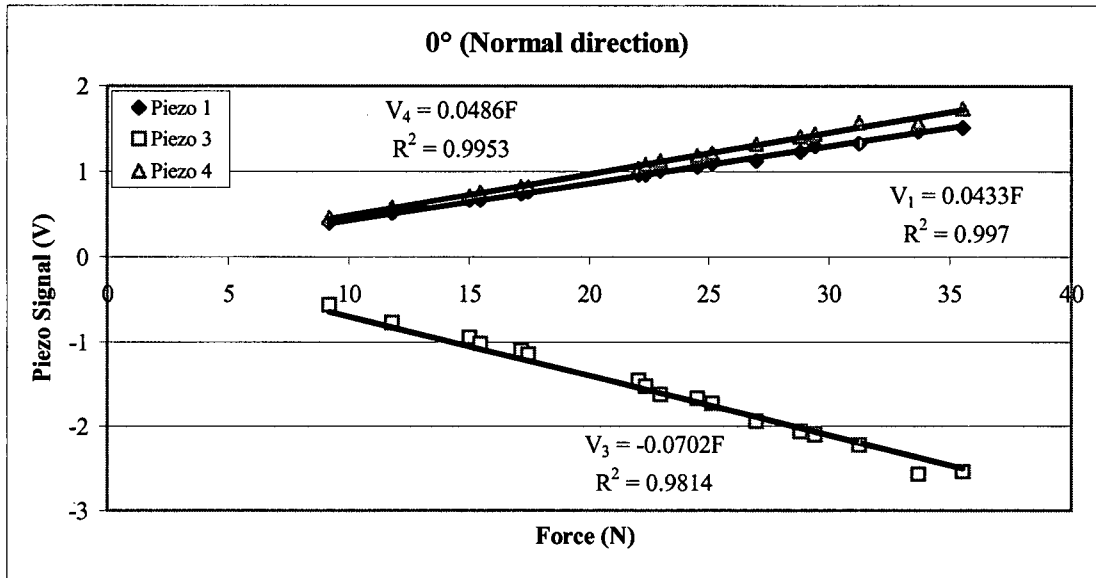


Figure C5. Impacts applied in the normal direction.

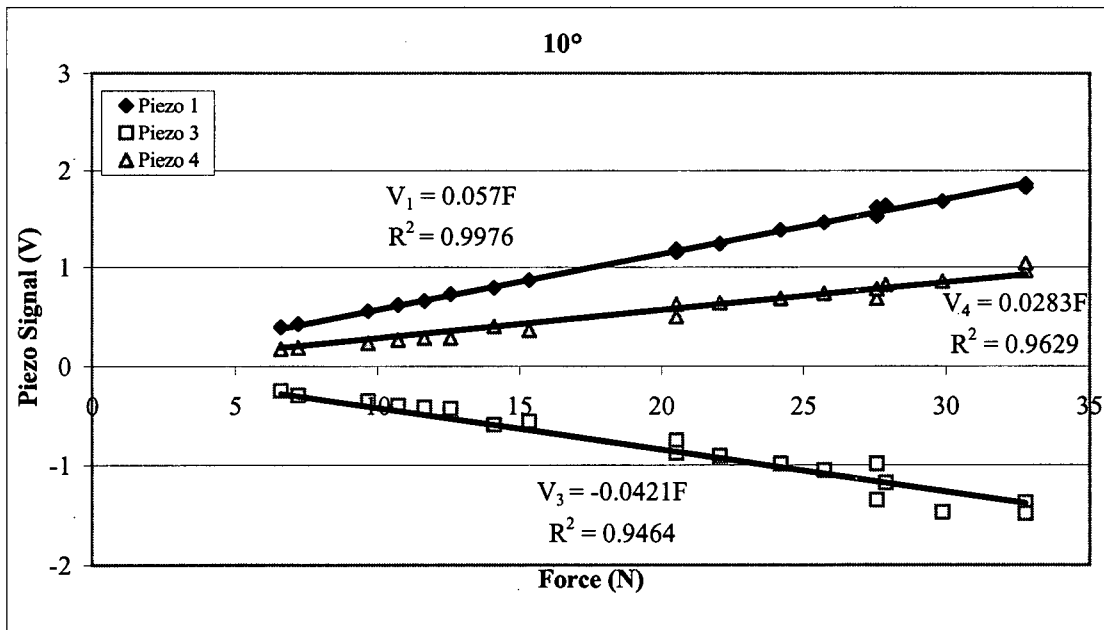


Figure C6. Impacts applied at 10° to the normal direction.

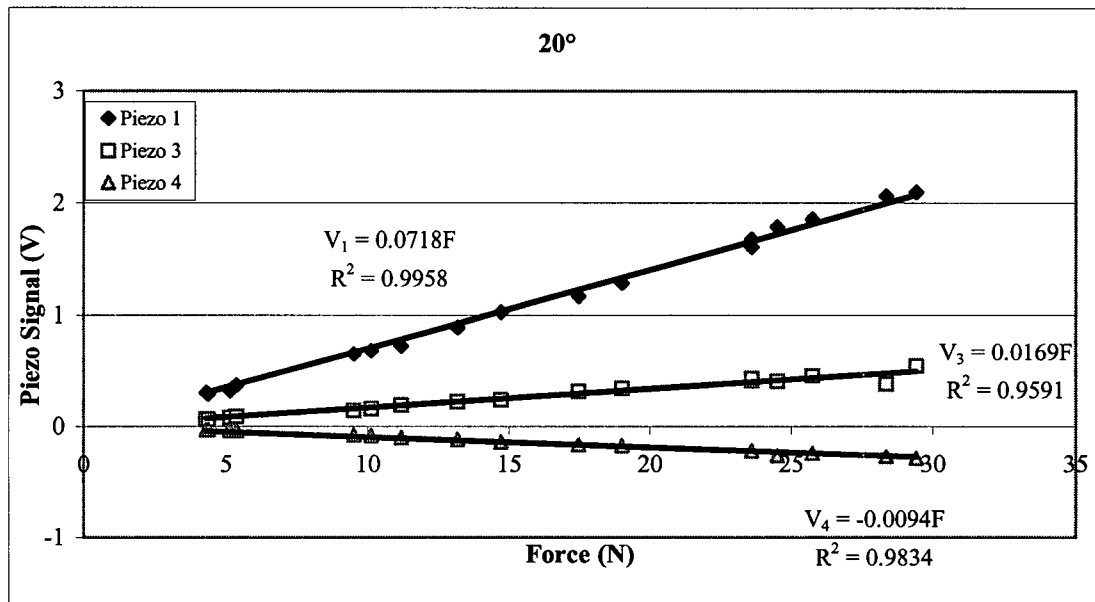


Figure C7. Impacts applied at 20° to the normal direction.

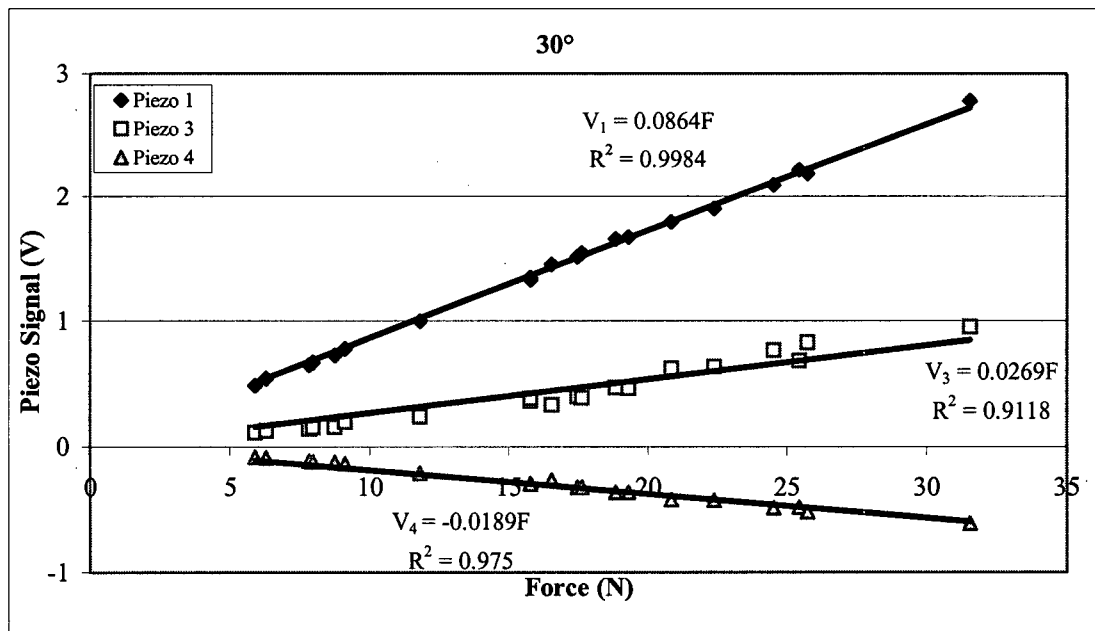


Figure C8. Impacts applied at 30° to the normal direction.

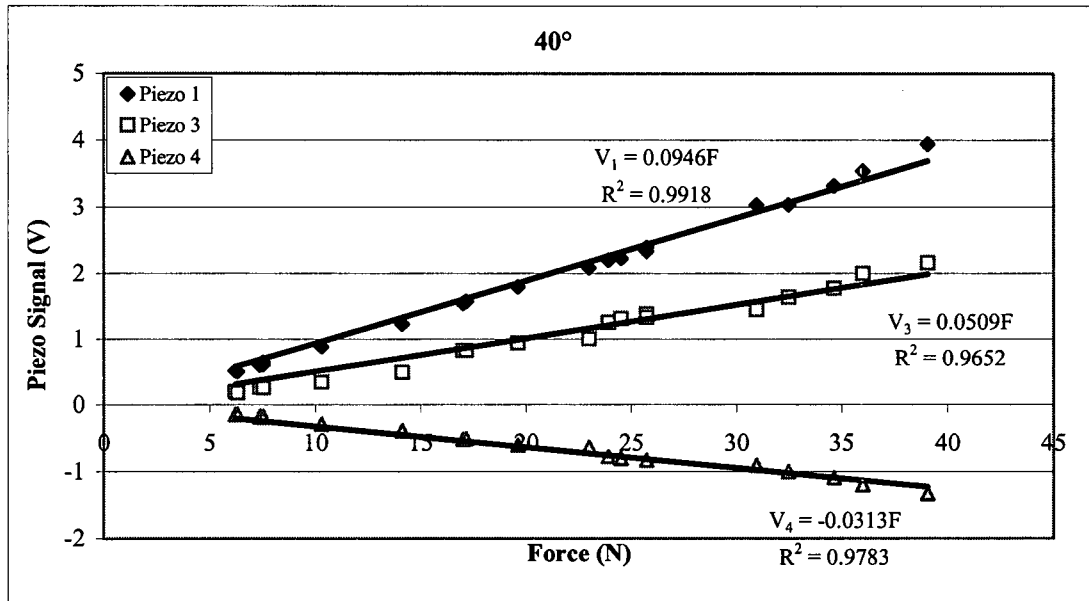


Figure C9. Impacts applied at 40° to the normal direction.

Angle (°)	Piezo 1		Piezo 3		Piezo 4	
	$K_{1θ}$ (mV/N)	K_{1S} (mV/N)	$K_{3θ}$ (mV/N)	K_{3S} (mV/N)	$K_{4θ}$ (mV/N)	K_{4S} (mV/N)
0	43.3	-	-70.2	-	48.6	-
10	57.0	82.7	-42.1	155.7	28.3	-112.7
20	71.8	91.0	16.9	242.3	-9.4	-161.0
30	86.4	97.8	26.9	175.4	-18.9	-122.0
40	94.6	95.6	50.9	162.8	-31.3	-106.6
	Ave K_{1S} = 91.8 mV/N K_{1N} = 43.3 mV/N		Ave K_{3S} = 164.6 mV/N K_{3N} = -70.2 mV/N		Ave K_{4S} = -113.7 mV/N K_{4N} = 48.6 mV/N	

Table C5. K-Values determined by impacting the sensor at different angles

As a validation of the calibration procedure, the following two graphs (Figures 4.7 and 4.8) show plots of the measured forces from the force hammer signal against the calculated forces from the piezo signals. The graphs show more scatter than Figure C4, which is the equivalent graph for the old calibration method. This is because of the difficulty in administering angled impacts in such a way that the line of action of the

applied force passed through the center of the probe tip. Regardless, the agreement was judged to be sufficiently good for a reliable determination of the forces.

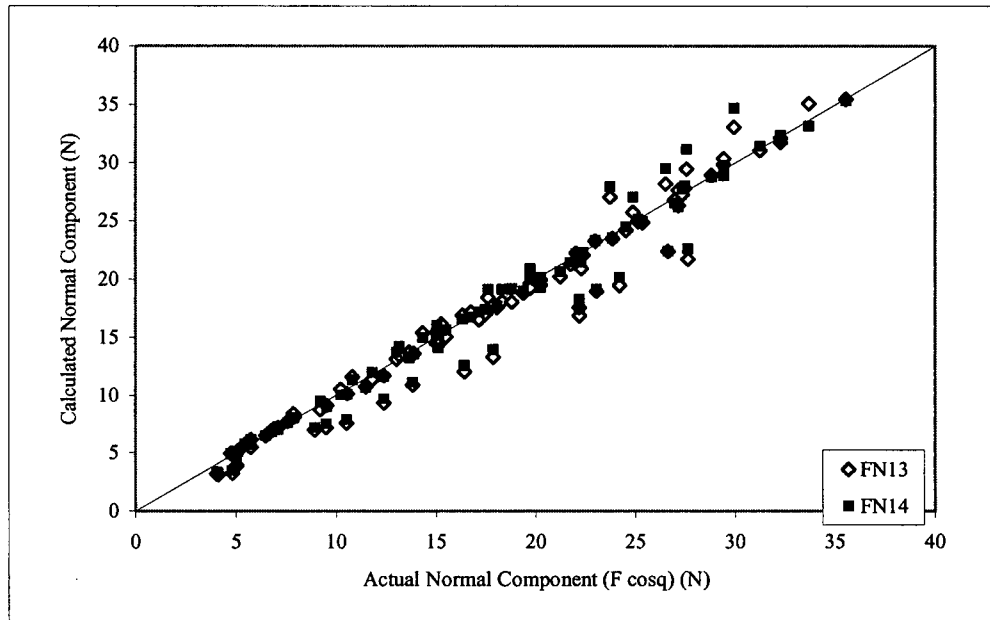


Figure C10. (Same as Figure 4.7) Comparison of calculated and measured normal forces.

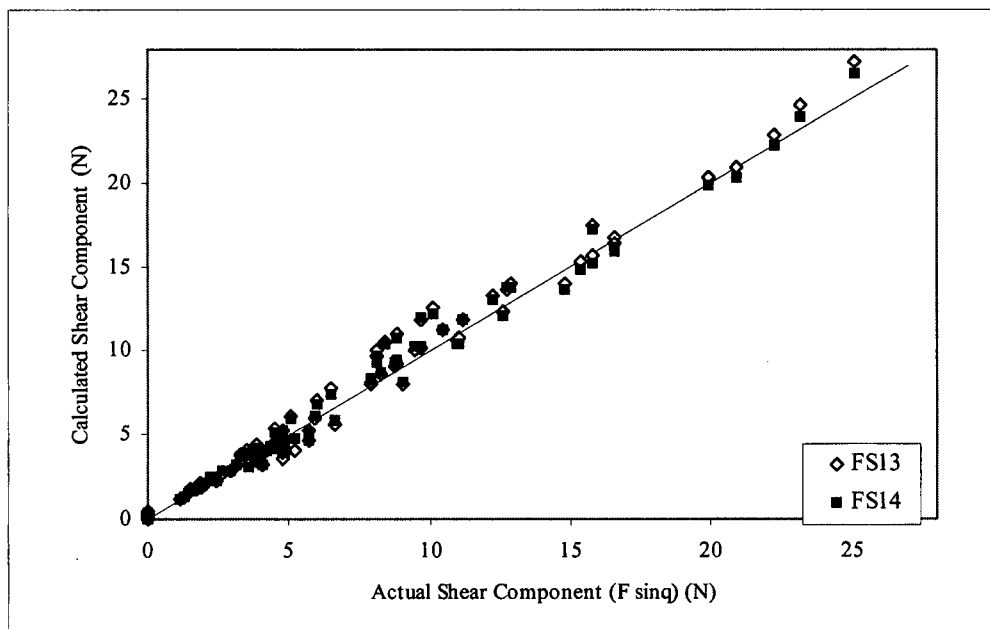


Figure C11. (Same as Figure 4.8) Comparison of calculated and measured shear forces.

APPENDIX D

MATLAB PROGRAMS

D1. CALIBRATION

"Calibn.m"

```
clear

load c:\lecroy\calibn\sc1000.dat; % Piezo 1 signal
load c:\lecroy\calibn\sc2000.dat; % Piezo 2 signal
load c:\lecroy\calibn\sc3000.dat; % Piezo 3 signal
load c:\lecroy\calibn\sc4000.dat; % Hammer signal

clear sc1000 sc2000 sc3000 sc4000;

c1(1)=max(sc1000); % Maximum piezo 1 voltage
c2(1)=min(sc2000); % Minimum piezo 2 voltage
c3(1)=min(sc3000); % Minimum piezo 3 voltage
h(1)=max(sc4000); % Maximum hammer voltage

load c:\lecroy\calibn\sc1001.dat;
load c:\lecroy\calibn\sc2001.dat;
load c:\lecroy\calibn\sc3001.dat;
load c:\lecroy\calibn\sc4001.dat;

c1(2)=max(sc1001); % Maximum piezo 1 voltage
c2(2)=min(sc2001); % Minimum piezo 2 voltage
c3(2)=min(sc3001); % Minimum piezo 3 voltage
h(2)=max(sc4001); % Maximum hammer voltage

clear sc1001 sc2001 sc3001 sc4001;

% The program proceeds in this way until all relevant impacts are processed. The
% vectors c1, c2, c3 and h are then exported to Microsoft Excel for the linear
% regression, k-value determination and derivation of force equations.
```

D2. TRANSFER FUNCTIONS

"TF.m"

```
clear

w=hanning(50002); % Define Hanning window

load d:\lecroy\calibn\sc1000.dat % Piezo signal
load d:\lecroy\calibn\sc4000.dat % Hammer signal
tfn=tfe(sc4000,sc1000,65536,10000000,w); % Calculate transfer function
tf1(1,:)=abs(tfn(1:750)'); % Calculate magnitude of transfer function
clear sc1000 sc4000;

load d:\lecroy\calibn\sc1001.dat
load d:\lecroy\calibn\sc4001.dat
```

```

tfn=tf(sc4001,sc1001,65536,1000000,w);
tf1(2,:)=abs(tfn(1:750)');
clear sc1001 sc4001;

% The program proceeds in this way until all relevant impacts are processed, and the
% average transfer function is then calculated as follows (usually for 10 impacts):

tfav1=sum(tf1)/11;           % Calculate average transfer function
tfdbl=20*log10(tfav1);      % Convert to decibels
f=(0:65535)*1000000/65536;  % Define frequency scale
fr=f(1:750);

figure(1)
plot(fr,tfdbl);
grid on;
hold on;
title('Average Transfer Function for Piezo 1');
xlabel('freq (Hz)');
ylabel('TF (dB)');

```

D3. REFINER FORCE SIGNAL ANALYSIS

“Getstats.m”

```

% This program loads piezo signals, calculates the shear and normal forces, registers the
% beginning and end of all impacts, and computes the desired statistics such as peak
% forces, coefficient of friction (as avratio and peakratio), and impact duration.
% These are then saved as column vectors that are extracted and compiled for several
% signals by the program named "Compilestats.m".

```

```
clear
```

```
load d:\lecroy\d4ref\sc1003.dat
load d:\lecroy\d4ref\sc2003.dat
```

```
V2=sc1003;    % Piezo 2 Voltage
V3=sc2003;    % Piezo 3 Voltage
```

```
clear sc1003 sc2003;
```

```
Fn=-4.40*V2-10.67*V3;
Fs=-1.68*V2+2.52*V3;
```

```
clear V2 V3;
```

% FORCE PROFILE ANALYSIS

```

peakcount=2;    % Peak Counter (set at 2 to start with because (peakcount-1)
                % as used below would otherwise give a negative index.
avrangle=2;     % Number of points either side of point 'i' used for mean value
thresh=1.0;     % Threshold force value (1 N) for recognizing impacts
impstart(1)=-150; % Avoids mishandling the first impact
impfinish(1)=-150;
buffer=100;     % Number of points neglected after an impact (to help
                % prevent registering vibrations as impacts)

impswitch=1;

% Noise Compensation by mean calculation
for i=1:avrangle
    meanFn(i)=Fn(i);
    meanFs(i)=Fs(i);
end
for i=length(Fn)-avrangle:length(Fn)

```

```

    meanFn(i)=Fn(i);
    meanFs(i)=Fs(i);
end
for i=1+avrange:length(Fn)-avrange-1
    meanFn(i)=mean(Fn(i-avrange:i+avrange));
    meanFs(i)=mean(Fs(i-avrange:i+avrange));
end

clear Fn Fs;

% Find location of start and end of impacts
for i=2:length(meanFn)
    if (meanFn(i-1)<thresh) & (meanFn(i)>=thresh) & (i-impstart(peakcount-
1)>buffer)
        impstart(peakcount)=i;
        impswitch=i;
    else
        if (meanFn(i-1)>thresh) & (meanFn(i)<=thresh) & (impswitch-impstart(peakcount-
1)>buffer) & impstart(length(impstart))>0
            impfinish(peakcount)=i;
            peakcount=peakcount+1;
        end
    end
end

IMPSTART=impstart/250;          % Convert indices to time (ms)
IMPFINISH=impfinish/250;

t=(0:4e-3:1000.004);

% Compute Impact Statistics
for j=2:peakcount-1
    floctimeindex(j)=IMPFINISH(j)-IMPSTART(j);
    Fnprofile(1:impfinish(j)-impstart(j)+1,j)=meanFn(impstart(j):impfinish(j));
    Fsprofile(1:impfinish(j)-impstart(j)+1,j)=meanFs(impstart(j):impfinish(j));
    maxFn(j)=max(Fnprofile(:,j));
    maxFs(j)=max(Fsprofile(:,j));
    peakratio(j)=maxFs(j)/maxFn(j);
    avratio(j)=mean(Fsprofile(1:impfinish(j)-impstart(j)+1,j)./Fnprofile(1:impfinish(j)-
impstart(j)+1,j));
end

% Save all stats
'Impact#   Fn Fs R(pk) R(av) Floc Size Index(ms)   impstart impfinish'
[(3:j)'   maxFn(3:j)' maxFs(3:j)' peakratio(3:j)'   avratio(3:j)' floctimeindex(3:j)'
IMPSTART(3:j)' IMPFINISH(3:j)']

stats003=[(3:j)'   maxFn(3:j)' maxFs(3:j)' pkratio(3:j)'   avratio(3:j)'
floctimeindex(3:j)' IMPSTART(3:j)' IMPFINISH(3:j)'];

meanfn003=meanFn;

save d:\research\data\d4ref\stats003;
save d:\research\data\d4ref\meanfn003;

```

D4. COMPILATION OF IMPACT STATISTICS

“Compilestats.m”

```

% This program provides a plot of the signal showing the start and end of impacts
% as recognized by "Getstats.m", and outputs all the impact data associated with
% the signal in question. This data is then exported to Microsoft Excel manually.

```

```

clear
load d:\research\data\d4ref\stats003

```

```

t=(0:1/1000:50000/1000);

% Plot of forces and start\finish points for the purpose of checking how well
% impacts were recognised by the previous program.
% The green lines signify the start of the extracted impacts and the red lines
% signify the end of the impacts.
figure(1)
clf;hold on;
plot(t,meanFn,'b',t,meanFs,'r');
for j=2:peakcount-1
    plot([IMPSTART(j) IMPSTART(j)],[-2 50],'g-',[IMPFINISH(j) IMPFINISH(j)],[-2 50],'r-');
end
xlabel('Time (ms)');
ylabel('Force (N)');
title('Impacts at 700RPM, Dec 4, sc*016b');

% Display vectors containing stored variables
'maxFn'
maxFn'
'maxFs'
maxFs'
'pkratio'
pkratio'
'avratio'
avratio'
'impdur'
impdur'
'flocsizeindex'
flocsizeindex'
'n='
length(maxFn)

```

APPENDIX E

ESTIMATED LENGTH OF BARS CROSSING AT ANY GIVEN TIME

This quantity was estimated in chapter 6 to estimate the total shear force acting on the rotor plate.

Assuming equal bar and groove widths, the surfaces of the bars constitute approximately half of the total area of the refining zone. That is:

$$A_b = \frac{A_{rz}}{2} \quad (\text{E1})$$

where A_b is the total area of bar surfaces and A_{rz} is the area of the refining zone.

The total bar length is then given by the total bar area divided by the bar width, B , and the total length of bars crossing is estimated to be half of the total bar length. Therefore:

$$L_{bc} = \frac{A_{rz}}{4B} = \frac{\pi(r_2^2 - r_1^2)}{4B} \quad (\text{E2})$$

where r_1 and r_2 are the inner and outer radii of the refining zone, respectively, and L_{bc} is the total length of bars crossing at any given time.

For the Sprout-Waldron 12-inch laboratory refiner with the D2B502 plates, r_1 is 12.25 cm, r_2 is 15.25 cm, and B is 2.8 mm, giving a value of 2.3 m for L_{bc} . For the Sprout-Waldron TWIN 60 refiner in [25], r_1 is 45 cm and r_2 is 78.5 cm, and B is assumed to be 2.8 mm, giving a value of 116 m for L_{bc} .